

GEORGIA DOT RESEARCH PROJECT 21-05

Final Report

**PRACTICAL ASSESSMENT OF
NON-DESTRUCTIVE TESTING (NDT)
TECHNIQUES FOR ON-SITE APPLICATION
OF GDOT PROJECTS**



Office of Performance-based Management and Research

600 West Peachtree Street NW | Atlanta, GA 30308

March 2025

TECHNICAL REPORT DOCUMENTATION PAGE

1. Report No. FHWA-GA-25-2105	2. Government Accession No. N/A	3. Recipient's Catalog No. N/A	
4. Title and Subtitle Practical Assessment of Non-Destructive Testing (NDT) Techniques for On-Site Application of GDOT Projects		5. Report Date March 2025	
		6. Performing Organization Code N/A	
7. Author(s) Hossein Taheri, Ph.D. https://orcid.org/0000-0003-1704-8775 Saman Hedjazi, Ph.D. https://orcid.org/0000-0003-2730-4832 Macy Spears		8. Performing Organ. Report No. 21-05	
9. Performing Organization Name and Address Georgia Southern University Laboratory for Advanced Testing, In-situ Monitoring and Evaluation (LANDTIE) Box 7991, Statesboro, GA 30460		10. Work Unit No. N/A	
		11. Contract or Grant No. Rp 21-05	
12. Sponsoring Agency Name and Address Georgia Department of Transportation (SPR) Office of Performance-based Management and Research 600 W. Peachtree Street NW Atlanta, GA 30308		13. Type of Report and Period Covered Final Report	
		14. Sponsoring Agency Code N/A	
15. Supplementary Notes Prepared in cooperation with the U.S. Department of Transportation, Federal Highway Administration.			
16. Abstract Non-destructive testing (NDT) is often conducted to evaluate the performance and condition of assets and infrastructures. Practical considerations must be considered when conducting NDT in the field. This study evaluates the effectiveness and practicality of various NDT methods for inspecting reinforced concrete structures, with a focus on the application of ground-penetrating radar (GPR). It encompasses two investigations: a laboratory study and a field study. In the laboratory, GPR was used on concrete slabs with simulated defects to validate the accuracy of GPR data against the slab designs. The field study, conducted on an aging bridge deck, employed multiple NDT techniques, including GPR, impact echo, ultrasonic pulse echo, a cover meter, and a rebound hammer. Most of the data from the NDT methods correlated well with the core samples, achieving acceptable accuracy levels. The study highlights the limitations of NDT methods in practical field conditions versus controlled laboratory settings, especially when dealing with unknown embedded objects and defects. However, it emphasizes the potential of NDT methods for structural evaluations in civil engineering, noting the importance of technical knowledge in interpreting results.			
17. Key Words Ground Penetrating Radar (GPR), Non-destructive Testing (NDT),		18. Distribution Statement No restrictions. This document is available through the National Technical Information Service, Springfield, VA 22161.	
19. Security Classif. (of this report) Unclassified	20. Security Classif. (of this page) Unclassified	21. No. of Pages: 210	22. Price: Free

GDOT Research Project 21-05

Final Report

PRACTICAL ASSESSMENT OF NON-DESTRUCTIVE TESTING (NDT) TECHNIQUES
FOR ON-SITE APPLICATION OF GDOT PROJECTS

By

Hossein Taheri, Ph.D.

Associate Professor of Manufacturing Engineering

Saman Hedjazi, Ph.D.

Associate Professor of Civil Engineering

and

Macy Spears

Graduate Student

Georgia Southern University

College of Engineering and Computing

Contract with

Georgia Department of Transportation

In cooperation with

U.S. Department of Transportation, Federal Highway Administration

November 2024

The contents of this report reflect the views of the authors, who are responsible for the facts and accuracy of the data presented herein. The contents do not necessarily reflect the official views of the Georgia Department of Transportation or the Federal Highway Administration. This report does not constitute a standard, specification, or regulation.

SI* (MODERN METRIC) CONVERSION FACTORS				
APPROXIMATE CONVERSIONS TO SI UNITS				
Symbol	When You Know	Multiply By	To Find	Symbol
LENGTH				
in	inches	25.4	millimeters	mm
ft	feet	0.305	meters	m
yd	yards	0.914	meters	m
mi	miles	1.61	kilometers	km
AREA				
in ²	square inches	645.2	square millimeters	mm ²
ft ²	square feet	0.093	square meters	m ²
yd ²	square yard	0.836	square meters	m ²
ac	acres	0.405	hectares	ha
mi ²	square miles	2.59	square kilometers	km ²
VOLUME				
fl oz	fluid ounces	29.57	milliliters	mL
gal	gallons	3.785	liters	L
ft ³	cubic feet	0.028	cubic meters	m ³
yd ³	cubic yards	0.765	cubic meters	m ³
NOTE: volumes greater than 1000 L shall be shown in m ³				
MASS				
oz	ounces	28.35	grams	g
lb	pounds	0.454	kilograms	kg
T	short tons (2000 lb)	0.907	megagrams (or "metric ton")	Mg (or "t")
TEMPERATURE (exact degrees)				
°F	Fahrenheit	5 (F-32)/9 or (F-32)/1.8	Celsius	°C
ILLUMINATION				
fc	foot-candles	10.76	lux	lx
fl	foot-Lamberts	3.426	candela/m ²	cd/m ²
FORCE and PRESSURE or STRESS				
lbf	poundforce	4.45	newtons	N
lbf/in ²	poundforce per square inch	6.89	kilopascals	kPa
APPROXIMATE CONVERSIONS FROM SI UNITS				
Symbol	When You Know	Multiply By	To Find	Symbol
LENGTH				
mm	millimeters	0.039	inches	in
m	meters	3.28	feet	ft
m	meters	1.09	yards	yd
km	kilometers	0.621	miles	mi
AREA				
mm ²	square millimeters	0.0016	square inches	in ²
m ²	square meters	10.764	square feet	ft ²
m ²	square meters	1.195	square yards	yd ²
ha	hectares	2.47	acres	ac
km ²	square kilometers	0.386	square miles	mi ²
VOLUME				
mL	milliliters	0.034	fluid ounces	fl oz
L	liters	0.264	gallons	gal
m ³	cubic meters	35.314	cubic feet	ft ³
m ³	cubic meters	1.307	cubic yards	yd ³
MASS				
g	grams	0.035	ounces	oz
kg	kilograms	2.202	pounds	lb
Mg (or "t")	megagrams (or "metric ton")	1.103	short tons (2000 lb)	T
TEMPERATURE (exact degrees)				
°C	Celsius	1.8C+32	Fahrenheit	°F
ILLUMINATION				
lx	lux	0.0929	foot-candles	fc
cd/m ²	candela/m ²	0.2919	foot-Lamberts	fl
FORCE and PRESSURE or STRESS				
N	newtons	0.225	poundforce	lbf
kPa	kilopascals	0.145	poundforce per square inch	lbf/in ²

* SI is the symbol for the International System of Units. Appropriate rounding should be made to comply with Section 4 of ASTM E380.
(Revised March 2003)

TABLE OF CONTENTS

EXECUTIVE SUMMARY	1
CHAPTER 1. INTRODUCTION	3
Background of Study.....	3
Objective.....	4
Project Scope.....	4
CHAPTER 2. GPR APPLICATIONS IN CIVIL ENGINEERING AND CONSTRUCTION	6
Detection of Rebar	6
Rebar Corrosion and Concrete Deterioration	7
Detection of Voids.....	9
CHAPTER 3. ASSESSMENT OF GPR CODES AND STANDARDS.....	12
Assessment of ASTM D6087 Standard.....	12
Scope.....	12
Summary of Test Method.....	14
Significance and Use	14
Apparatus	15
Hazards	16
Procedure.....	17
Data Processing	18
Report.....	20
Precision and Bias	21
System Performance Compliance.....	21
Pre-operation Measurement	29
GPR Data Acquisition	30
Data Processing	32
Assessment of ASTM D4748 Standard.....	43
Apparatus	43
Summary of Test Method.....	47
Relative Dielectric Constants of Typical Pavement Materials.....	49
Assessment of ASTM D6432 Standard.....	55
Significance and Use	57
Parameter Being Measured and Representative Values	58
Limitations and Interferences.....	67
Assessment of AASHTO-PP 98 Standard	69
Hardware Requirements	71

Software Requirements	75
Evaluate the Adjustment, Modification, or Recommendations Needed to Consider in Comparison to ASTM D4748 and ASTM D6432.....	82
CHAPTER 4. NDT TOOLS UTILIZED IN TRANSPORTATION PROJECTS IN THE FIELD	88
Technical Assessment of NDT Tools.....	88
Cover Meter (Proceq Profometer 650).....	88
Swiss Hammer (Proceq Schmidt OS8000).....	96
Thickness Coating Gage (DeFelsko Corporation, PosiTector 6000).....	102
Resistivity Resipod (Proceq)	111
Technical Assessment of GPR (Proceq GP8000)	114
Other NDT Tools.....	117
Review of GPR Post-processing Software.....	123
GPR Slice	124
GPR Insights.....	125
Comparison of Equivalent and Major GPR Products.....	128
CHAPTER 5. EXPERIMENTAL INVESTIGATIONS	136
Laboratory-scale Investigation	136
Methodology	136
Results	138
Discussion.....	143
I-16 Bridge in Macon, GA	147
Bridge over Ogeechee River	148
Methodological Approach	155
Results	157
Impact Echo.....	165
CHAPTER 6. PRACTICAL IMPLEMENTATION OF GPR.....	173
Understand and Study the Science of Identified GPR Tool, Its Sensitivity, and Its Potential Technical Limitations or Service-maintenance Requirement	173
Study the Technical Challenges and Operational Limitations of GPR.....	176
GPR Data Collection	179
Acquisition Parameters	179
GPR Data Interpretation.....	186
Preprocessing.....	186
Detection of Interface Reflections.....	187
Dielectric Properties Estimation.....	188
Layer/distress Separation.....	189

Optimizing the Information Yield from GPR	189
Locating the Target.....	190
Depth and Size Estimation	191
GPR in Coastal Environments	194
Field Work, Survey Design, and Topographic Correction	194
Choice of Antenna Frequency for Effective GPR Surveys	196
Practical Implementation (GPR Test Procedure).....	200
CHAPTER 7. CONCLUSIONS AND RECOMMENDATIONS	208
ACKNOWLEDGEMENTS	210
REFERENCES.....	211

LIST OF FIGURES

Figure 1. Diagrams. GPR system surveying over cylindrical objects: (a) top view of scanning and (b) theoretical hyperbolic result of scanning, where x_n denotes the position.....	6
Figure 2. Block diagram. GPR and support equipment as demonstrated in ASTM D6087.	16
Figure 3. Flowchart. Accepted GPR data processing methodologies.....	20
Figure 4. Diagram. Near field and far field regions of antenna.	23
Figure 5. Diagram and graph. SNR test: (a) antenna and metal plate principle and (b) amplitude versus time graph	24
Figure 6. Drawing. Laboratory setup for analyzing SNR with a distance of 30 cm between radar box and copper sheet	25
Figure 7. Graph. Normalized (to 1) amplitude variations for 100 consecutive radar traces of the signal peak with 1 GHz GPR system with varying heights of the antenna	26
Figure 8. Graphs. Linearity in the time axis and time window: amplitude and time window graphs for (a) position 1: $2\lambda c$; (b) position 2: $3\lambda c$; and (c) position 3: $2.5\lambda c$	28
Figure 9. Flowchart. GPR data processing scheme for clutter removal.	29
Figure 10. Diagram. GPR inspection passes for air-launched antenna systems.....	31
Figure 11. Schematic diagram. GPR antenna passing over embedded rebar at 90° angle.	32
Figure 12. Diagram. GPR inspection passes for ground-coupled antenna systems.....	32
Figure 13. Line scan. A-scan and radargram output from GPR surveying on 8 ft of RC floor.....	38
Figure 14. Graph. Effects of deterioration on GPR signal amplitude.....	39
Figure 15. B-scan image. Bridge deck.....	40
Figure 16. Map. GPR results of a bridge deck: attenuation map using amplitude analysis	41
Figure 17. Venn diagram. Comparison of the sections outlined in ASTM D6087 in which GPR system they are to be applied.	42
Figure 18. Schematic. Relationship between GPR antenna frequency, resolution, and penetration depth when detecting subsurface objects.	44
Figure 19. Drawings. Representation of Section 4.1.1.1, showing the comparison of different suggested antenna frequencies and determining layer thickness.	45
Figure 20. Diagram. Ground-coupled and air-coupled antenna systems of GPR.....	46
Figure 21. Diagram. Typical equipment configuration for GPR using a vehicle or cart. Air-coupled antenna system is shown.	47
Figure 22. Photos. Hasan and Yazdani study: (a) drilling of bridge deck and (b) measuring actual cover depth after coring.....	51
Figure 23. Diagram. CMP method of GPR measurement of a single subsurface layer	51
Figure 24. Flowchart. General GPR data processing.....	54
Figure 25. Schematic diagram. GPR system with (a) monostatic and (b) bistatic antenna.	56

Figure 26. Plots. One example of simulation: incident signal (top left), 0.61 ns impulse response (top right), simulated signal (bottom left), and noisy signal (bottom right).	61
Figure 27. Plots. Variation of attenuation of GPR reflected signal from rebars with TWTT: before and after the depth-correction procedure.	64
Figure 28. Graph. Relationship between depth-corrected attenuation measured by air-coupled GPR system.	65
Figure 29. Plot. Relationship between depth-corrected attenuation of concrete cover and relative permittivity of concrete on the top surface of the bridge decks.....	65
Figure 30. Photo. Basic equipment for DPS.	71
Figure 31. Graphs. Example heat map and line graph.	77
Figure 32. Diagram. Equipment setup for DPS with GPR.	79
Figure 33. Graph. Dielectric values for an asphalt pavement using 2 GHz GPR.....	80
Figure 34. Photo. Walking cart (left), gator-mounted (center), and prototype (right) robotic DPS units	81
Figure 35. Photo. PaveScan RDM 2.0 (GSSI™).	81
Figure 36. Screenshot. Example of visual output from PaveScan data with a color map showing anomalies in dielectric measurement (top) and a line graph of the dielectric output of each sensor (bottom) (GSSI™).	82
Figure 37. Photo. Proceq Profometer 650 detector and monitor (Screening Eagle™).	88
Figure 38. Screenshot. Demonstration of Cross-line mode to display rebar arrangements.....	89
Figure 39. Screenshot. Demonstration of Cross-line view displaying high/low signal intensities	90
Figure 40. Screenshot. Demonstration of Single-line view displaying rebar parameters and location.....	90
Figure 41. Screenshot. Demonstration of Multi-line view displaying Signal strength intensity	91
Figure 42. Screenshot. Demonstration of Statistics view for statistical analysis.....	92
Figure 43. Screenshot. Settings for Rebar diameter, Maximum cover, and Minimum cover parameters (Screening Eagle™).	92
Figure 44. Screenshot. Proceq Profometer Link software displaying Single-line graph (Screening Eagle™).	94
Figure 45. Screenshot. Proceq Profometer Link for Multi-line view displaying Signal strength (Screening Eagle™).	94
Figure 46. Screenshot. Proceq Profometer Link Statistical, Single-line, Multi-line, and Cross-line view graphs (Screening Eagle™).	95
Figure 47. Photo. Schmidt Hammer (Schmidt OS8000) (Screening Eagle™).	97
Figure 48. Screenshot. Schmidt app demonstration (Screening Eagle™).	98
Figure 49. Screenshot. Demonstration of Original Schmidt Live calculating the median (Screening Eagle™).	98

Figure 50. Screenshot. Demonstration of Original Schmidt Live calculating the impact angle correction (Screening Eagle™).	99
Figure 51. Screenshot. Demonstration of checking the app for availability of an update (Screening Eagle™).	100
Figure 52. Images. PosiTector 6000: (a) typical screen and (b) bottom functions.	107
Figure 53. Photos. PosiTector probes.	109
Figure 54. Photo. Proceq Resipod Resistivity Meter.	112
Figure 55. Photo. GPR (Proceq GP8000™).	115
Figure 56. Schematic. Concrete delamination.	115
Figure 57. Schematic. GPR working principle.	116
Figure 58. Photos. Proceq GS8000: (a) device with the tablet and (b) base.	117
Figure 59. Photos. PD8050 iOS app: (a) Stripe scan (on-site 3D) mode and (b) Line scan mode operation.	121
Figure 60. Photo. T-C-10 Cementometer Type R™.	122
Figure 61. Graphs. GPR Slice results of hyperbola fitting.	125
Figure 62. Scan. GPR data in GPR Insights with time gain.	126
Figure 63. Screenshots. GPR Insights: features of the condition map (left) and deterioration map (right).	127
Figure 64. Image. B-scan image of bridge deck.	128
Figure 65. Photo. Surveying grid and directions for GPR scanning on top of slab.	138
Figure 66. Image. GPR line scan result with corroded rebar.	140
Figure 67. Image. GPR line scan result for slab with polystyrene sheets.	141
Figure 68. Images. GPR line scan results for slab with small polystyrene sheets: (a) X ₃ scan and (b) Y ₂ scan.	141
Figure 69. Photo. Slab with visible voids from balloons and one water bottle beneath the surface.	142
Figure 70. Images. GPR line scan results: (a) PVC pipe location and (b) void location.	143
Figure 71. Photos. Laboratory-scale GPR testing.	145
Figure 72. Images. Maximum speed: (a) Test 1 and (b) Test 2.	146
Figure 73. Images. Maximum depth: (a) Test 1 and (b) Test 2.	147
Figure 74. Photo. Surveying bridge deck with Proceq GP8000 GPR (GSU research team).	148
Figure 75. Photo. Measuring distance to the core location from curb.	148
Figure 76. Photo. Satellite view of bridges over Ogeechee River: bridge in use (left) and subject bridge not in use (right).	149
Figure 77. Photos. Bridge deck: (a) top and (b) underside.	150
Figure 78. Image. GPR B-scan data in the y-axis.	151
Figure 79. Image. GPR B-scan data in the x-axis.	151
Figure 80. Photo. Core drill in use.	152
Figure 81. Photos. Core 12 days after extraction, corresponding to GPR data in figure 78. Length = 7 inches.	152

Figure 82. Photos. Core 12 days after extraction, corresponding to GPR data in figure 79. Length = 7.5 inches.....	153
Figure 83. Photo. Pundit PI8000 probe and impactor.....	153
Figure 84. Photo. PM8000 Pro equipment and drawn grid for surveying.....	154
Figure 85. Photo. Surveying bridge deck with Proceq GP8000 GPR (GSU research team).....	155
Figure 86. Photo. Location of a drilled core.	157
Figure 87. Photos. Eight core specimens chosen for visual inspection.	158
Figure 88. Image. A-scan and B-scan data for core location C7.	159
Figure 89. Image. A-scan and B-scan data for core location I9.	159
Figure 90. Image. A-scan and B-scan data for core location H8.	161
Figure 91. Diagram. 3D visualization of rebar in the bridge deck based on GPR scans.	161
Figure 92. Graph. Mean and standard deviation for rebar depth in both directions.	163
Figure 93. Graph. Mean and standard deviation for rebar spacing in both directions.....	163
Figure 94. Image. UPE line scan data for core location H8.	165
Figure 95. Graphs. IE data response for core H8: FFT (top) and time domain (bottom).	167
Figure 96. Images. Core locations after extraction.	169
Figure 97. Graph. 90 wavelet representing the pulse of EM waves within the GPR signal.....	173
Figure 98. Diagram. Change in penetration depth in concrete as a function of frequency	180
Figure 99. Graph. Reflection amplitude mapped along the same distance in different weather conditions. Dashed line shows smoothed amplitude data.	183
Figure 100. Images. GPR scans collected over a bridge deck using the range of 15 ns and the following number of samples per scan: (a) 128, (b) 256, (c) 512, (d) 1024, and (e) 2048	185
Figure 101. Image. Raw radar data acquired with a GSSI SIR-10A+ using a bistatic 900 MHz in air center frequency antenna towed across a 90 cm diameter pipe buried 37 cm deep.	191
Figure 102. Images. Steps in data and image post-processing to enhance imaging results.....	192
Figure 103. Images. Steps in data and image post-processing to enhance quantitative results.	193

LIST OF TABLES

Table 1. Review of research using GPR for rebar evaluation.....	8
Table 2. Review of research using GPR for void detection.....	10
Table 3. Revisions of ASTM D6087 standard.....	12
Table 4. Assessment of covering scope of standard ASTM D6087.	13
Table 5. Summary of test method in ASTM D6087.....	14
Table 6. Significance and use of ASTM D6087.....	14
Table 7. Characteristics and requirements of the required apparatus according to ASTM D6087.....	15
Table 8. Potential, but not limited to, hazards while operating GPR according to ASTM D6087.....	16
Table 9. The recommended procedure of GPR testing and relevant considerations according to ASTM D6087.....	17
Table 10. Accepted GPR data processing methodologies.	19
Table 11. Minimum requirement of reports.....	21
Table 12. Requirements for precision and bias.....	21
Table 13. Relative dielectric constants and radar wave velocity through the materials.	52
Table 14. Approximate EM properties of various materials.....	62
Table 15. Dual criteria-based GPR interpretation for condition assessment of concrete bridge decks with asphalt overlays in Korea expressway networks.	66
Table 16. Radar wavelengths (meters) for various antenna frequencies (f) and relative permittivities (ϵ_r).....	68
Table 17. Operating requirements summary table with required limits.	73
Table 18. Summary of GPR products (Screening Eagle TM and GSSI TM).....	129
Table 19. Pulse velocity measurements and concrete quality.....	156
Table 21. UPE data for slab depth estimation.....	164
Table 22. IE data for slab thickness estimation.	166
Table 23. Comparison of rebar depth values with GPR and core data.	168
Table 24. Comparison of slab depth data from GPR, UPE, IE, and core specimens.	170
Table 25. Concrete core compressive test data.	172
Table 26. GPR major technical challenges.	177
Table 27. GPR major operational limitations.	178
Table 28. Apparent depth estimates calculated for given values of dielectric permittivity and range (ns).....	184

EXECUTIVE SUMMARY

This study evaluates the effectiveness and practicality of various non-destructive testing (NDT) methods for inspecting reinforced concrete structures, with a particular focus on ground-penetrating radar (GPR). The research comprises two investigations: a laboratory study and a field study, each aimed at exploring the reliability and limitations of NDT techniques in different environments.

In the laboratory investigation, GPR was applied to concrete slabs containing simulated defects designed to mimic real structural flaws. This experiment served as a preliminary validation of GPR data by comparing the results against the known design parameters of the slabs. The data collected demonstrated GPR's capability to detect embedded defects, thus confirming the method's accuracy in a controlled setting.

The second study was conducted on an aging bridge deck and involved the use of multiple NDT methods, including GPR, impact echo (IE), ultrasonic pulse echo (UPE), and use of a cover meter and a rebound hammer. GPR was primarily used to locate embedded reinforcement steel and areas of suspected concrete deterioration caused by reinforcing bar (rebar) corrosion. Core samples were extracted from the deck for visual inspection and comparison with the GPR data. Additionally, compressive strength tests on the bridge deck were performed and compared with estimates obtained from the rebound hammer. The IE and UPE techniques were utilized to determine the thickness of the deck slab, and the cover meter provided data on rebar depth and spacing.

The field study results were generally in good agreement with the core sample data, demonstrating the potential of NDT methods for accurate structural assessment. However, the

study also highlighted key limitations when applying NDT in real-world conditions as opposed to controlled laboratory environments. The presence of unknown embedded objects and flaws poses challenges for accurate interpretation, making technical expertise crucial for meaningful evaluations.

Despite these challenges, the research underscores the promising future of NDT methods in civil engineering and infrastructure maintenance. With further refinement and increased understanding of NDT techniques, particularly GPR, these methods hold significant potential for efficient, non-invasive evaluation of structures, offering valuable tools for both immediate inspections and long-term condition monitoring.

CHAPTER 1. INTRODUCTION

BACKGROUND OF STUDY

The maintenance of transportation infrastructure relies on dependable testing methods for the evaluation of materials and components to ensure proper repair can be done where needed. Particularly, non-destructive testing (NDT) applications are desirable in many cases to avoid destructive testing procedures, which damage the tested area. NDT methods have been implemented on pavement and bridge deck structures to locate subsurface layers, materials, and anomalies. Some of the deterioration types of highest concern found in bridge decks consist of reinforcing bar (rebar) corrosion, delamination, cracking, and concrete degradation, which usually give rise to one another [1]. These flaws within the structure can lower the strength of the concrete, reducing the service life expectancy. Therefore, detecting weaknesses in a structure is critical for the safety of the public and can save on major repair costs in the end.

This study analyzes the practicality and accuracy of NDT techniques on concrete structures through two cases outlined in this report. The first is a laboratory experiment involving concrete slabs with implanted objects to mimic typical defects in concrete. The slabs were evaluated with the NDT instrument known as ground-penetrating radar (GPR). The GPR results were verified by the designer of the slabs based on knowledge of where the objects were actually located. This case was part of the preliminary work for the principal study: a field investigation on an inactive bridge deck. For this situation, GPR served as the primary testing method with other supplementary NDT. The additional methods utilized were impact echo (IE), ultrasonic pulse echo (UPE), a rebar cover meter, and a rebound hammer. All the techniques in this study were

performed manually, and no automated equipment was utilized. The methods were compared to each another where applicable, and core specimens were extracted to corroborate the NDT data.

OBJECTIVE

Many researchers have observed the application of NDT methods through a controlled laboratory environment with simulated defects [2], [3]. These studies have been successful in showing the reliability of NDT methods for flaw detection in these situations. However, the feasibility and practical application of testing on existent, large-scale structures can be more difficult. Assessing bridge decks through NDT methods has some practical challenges, especially when the flaw type and location are not identifiable from a visual inspection. Utilizing these devices requires preliminary knowledge on the background of the equipment and also a familiarity with standard designs for the structure. More specifically, this work outlines the possibilities and limitations when implementing a variety of NDT methods in an authentic testing situation. This research explores how limited knowledge on the original structural drawings and details can make data analyses more difficult for verification. Unlike laboratory testing with simulated defects, detecting flaws in a real structure is more challenging when the size and severity is unknown. This research was conducted in collaboration with the Georgia Department of Transportation (GDOT) with the objective to document and analyze the practical assessment of NDT techniques available for bridge decks and pavement construction projects.

PROJECT SCOPE

A review of previous work involving the application of GPR is included in chapter 2, along with a literature summary of work related to utilization of GPR as the NDT method for bridge investigations. Chapter 3 provides an assessment of codes and standards related to GPR.

Chapter 4 details the NDT tools utilized in transportation projects. Chapter 5 describes the experimental work plan for this research study and presents the experimental results obtained from the laboratory and site investigations and post-processing. Chapter 6 discusses the significance and benefit of this study, in addition to the practical implementation of the project. Chapter 7 provides the research conclusions, along with recommendations for future studies.

CHAPTER 2. GPR APPLICATIONS IN CIVIL ENGINEERING AND CONSTRUCTION

DETECTION OF REBAR

The outcome of surveying cylindrical objects, such as rebar and pipes, is the creation of a hyperbolic shape on the GPR radargram [4]. This formation represents the antenna system moving toward the buried object and then away as the GPR crosses over it in a perpendicular direction. Therefore, the top of the hyperbolic shape indicates the position of the object. A basic schematic is shown in figure 1 for a representation of surveying over a circular object and an idealized hyperbolic shape that will show on the B-scan data output. With this approach, the following information on rebar can be found: location, spacing, and depth [5]. Although there are limitations on estimating the diameter of a buried item using GPR, the size of the hyperbola on the scan can provide an indication of the size of the object compared to surrounding objects. A wider hyperbolic shape typically represents a larger diameter because it takes longer for the system to move across it. Studies from Ristic et al. [6] and Hasan and Yazdani [7] explored approaches for estimating sizes of cylindrical objects with GPR.

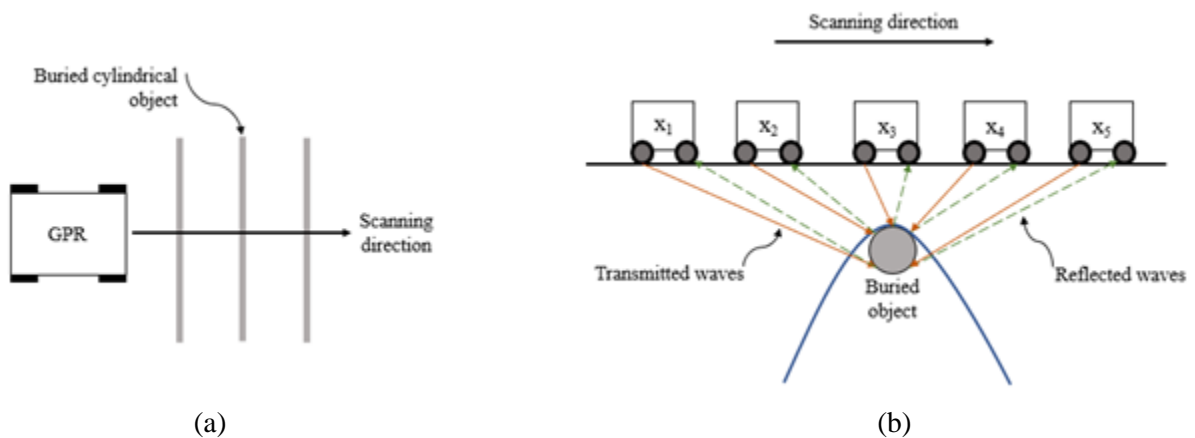


Figure 1. Diagrams. GPR system surveying over cylindrical objects: (a) top view of scanning and (b) theoretical hyperbolic result of scanning, where x_n denotes the position.

REBAR CORROSION AND CONCRETE DETERIORATION

Detecting embedded rebar non-destructively is important, not only for finding the members but for assessing the condition. Because rebar is susceptible to corrosion, which can lead to cracking and delamination of the surrounding concrete, identification of this occurrence is critical when evaluating reinforced concrete (RC) structures. However, determining the condition of the rebar is typically more complicated than locating the rebar with GPR. Many researchers have studied the applicability of GPR for inspecting rebar for corrosion by analyzing signal attenuation and the clarity of hyperbolic shapes. Attenuation in GPR terms describes the differences in the amplitude of a wave, such as the different values from rebar reflections. Similarly, an evaluation of the surrounding concrete through GPR results can also show signs of rebar corrosion, which leads to deterioration.

In their review, Tešić et al. analyzed and compared numerous related works, focusing on the application of GPR for inspection of reinforcement corrosion in concrete [8]. They observed that experiments in the laboratory had a primary focus of only corrosion detection, whereas inspections on-site differed as the separate effects from corrosion were able to be analyzed. Therefore, these products should be considered when emulating a corrosive environment for concrete in a laboratory condition. For inspection of corrosion, the most-used NDT methods are potential and resistivity measurements; potential measuring involves studying the potential changes between the rebar or materials, and resistivity measurements are used to determine concrete electrical resistivity [9]. GPR could be considered as a more challenging corrosion assessment technique compared to these, although studies have still shown the significance of using GPR for this purpose. A summary is presented of a different review of comparable work, specifically related to using GPR for the inspection of rebar corrosion and defects (table 1).

Table 1. Review of research using GPR for rebar evaluation.

Study	Year	GPR Antenna Frequency (GHz)	Purpose/Experiment	Main Findings
Wong et al. [10]	2018	2	Evaluated concrete delamination by accelerated rebar corrosion in a laboratory setting. Part of the slab was immersed in 4% saline solution and the other was exposed to freshwater.	Noticeable changes in the amplitudes of the rebar reflections were observed in the saline and freshwater sections of the slab when compared to the control. An increase in amplitude occurred in both sections due to the accelerated corrosion.
Eisenmann et al. [11]	2018	1.6 and 2.6	Evaluated a bridge on-site and a laboratory experiment to analyze rebar corrosion and its effect on GPR signals.	The areas with low amplitudes represented the thinning of rebar due to corrosion. The 2.6 GHz antenna system was preferred over the 1.6 GHz for concrete.
Dinh et al. [12]	2017	1.5	Utilized MATLAB to create contour maps of bridge decks. The authors studied the characteristics from A-scan and B-scan data from a bridge deck as their model motivation.	Concrete in good condition displayed a strong reflection from the rebar, whereas a corrosive concrete environment exhibited weak reflections. These weaker reflections made the hyperbolic shapes on the B-scan image appear faded or blurry.
Abouhamad et al. [13]	2017	1.5	Created contour maps for bridge decks from both numerical-based (amplitude values) and image-based (radargram data) analyses.	Numerical-based results: Lower amplitude values corresponded to deterioration. Image-based results: Strong rebar reflection with clear hyperbola shape indicated good condition. Strong attenuation and distorted hyperbola shape represented signs of severe corrosion. The image-based analysis proved to be more accurate.
Alani et al. [14]	2013	2	Investigated bridge decks for determining rebar location and spacing, as well as locating areas of moisture penetration and delamination.	Sound concrete was represented in the radargram as clearer signals and strong returns from the rebar. Deteriorated areas were shown to have signal attenuation due to moisture.

From a review of literature, the following assumptions can be made when analyzing GPR scans for rebar characteristics:

- Rebar is located by a distinct hyperbolic shape on the radargram.
- A strong reflection from the rebar indicates sound concrete, whereas a weak reflection shows signs of deterioration.
- A distorted/blurry hyperbolic shape may represent rebar corrosion and deterioration of concrete.
- Accurately locating corroded rebar relies heavily on the condition of the surrounding concrete.

DETECTION OF VOIDS

Voids within concrete are described as empty space, and they include gaps or holes of air that can contribute to failure of the structure. Commonly used NDT methods for detecting voids consist of ultrasonic and IE [15]. Locating voids within concrete is also possible through implementation of GPR. Specifically, voids are detectable on a radargram by displaying a sharp contrast in color, typically black and white, which appears more intense compared to the rest of the image. Investigations with GPR to locate voids have been evaluated on both RC structures and asphalt pavements. An evaluation of literature on detecting voids with GPR is presented in table 2.

Table 2. Review of research using GPR for void detection.

Study	Year	GPR Antenna Frequency (MHz)	Purpose/Experiment	Main Findings
Lai et al. [16]	2017	400 and 900	Excavated air-filled voids in a soil tank in a laboratory experiment and analyzed asphalt pavement in the field for detection of voids.	Overlaid or surface material can affect the feasibility of detecting voids. Detecting voids in plain concrete with nonmetallic utilities is comparatively easy. Voids will display as local reflectors, but utilities will show as continuous reflections.
Thitimakorn et al. [17]	2016	400	Surveyed a road for subsurface void detection and drilled cores to confirm results.	GPR successfully found the location of the void as the results were validated with the core sample, but GPR should be used along with another testing method.
Xie et al. [18]	2013	900	Utilized an automatic recognition algorithm for detecting voids in RC structures through a simulation with synthetic images.	The algorithm was able to locate the three individual voids in each simulation model, which included one without any rebar. The models with steel bars were observed to be a disadvantage for locating voids.
Cassidy et al. [19]	2011	450 and 900	Scanned an RC slab with a buried void and compared results to UPE technique.	The 900 MHz antenna provided more desirable results for this situation. Ultrasonic techniques have the ability to overcome some of the challenges of GPR.

After studying different situations for detecting voids using GPR in the laboratory, field, and with simulations, the following conclusions can be drawn:

- Voids can be detected in reinforced and unreinforced concrete structures.
- Detecting voids surrounding other subsurface objects may be challenging, especially with metallic objects.
- Voids present themselves on B-scans as a recognizable change in contrast/color when compared to the surrounding image.

- Voids are typically seen as a local reflection.

CHAPTER 3. ASSESSMENT OF GPR CODES AND STANDARDS

ASSESSMENT OF ASTM D6087 STANDARD

ASTM D6087 presents the standard test method for evaluating asphalt-covered concrete bridge decks using GPR for the evaluation of concrete or rebar. Specifically, this method can be applied to bridge decks overlaid with asphalt concrete or Portland cement concrete, and even those without an overlay. The importance of evaluating the condition of the concrete and rebar is to detect any deterioration of these materials. This standard outlines the procedures and data processing techniques that can be followed for assessment of the concrete or rebar components in a bridge deck. GPR systems are categorized depending on the antenna system setup, which consists of air-launched horn antennas or ground-coupled antennas. Depending on which antenna system the GPR utilizes, the ASTM testing procedure can differ.

This report provides the background information needed to execute the procedure. Examples of similar work may be included in sections for a comprehensive understanding of the working principles and data outputs presented by GPR equipment. Table 3 summarizes the revisions of this standard up to the version under assessment in this report.

Table 3. Revisions of ASTM D6087 standard [20].

Date	Revision
2008	Original Adoption
2015	Reapproved
2015 ¹	Editorial change ²

¹Version under assessment in this report.

²Converted inch-pound units removed editorially in June 2015.

Scope

The covering scope of standard ASTM D6087 is discussed in table 4.

Table 4. Assessment of covering scope of standard ASTM D6087.

Standard Language	Note/Discussion	Remark
<p>Covers the procedure for:</p> <ul style="list-style-type: none"> ❖ Concrete bridge decks overlaid with asphaltic concrete wearing surfaces. ❖ Bridge decks overlaid with Portland cement concrete. ❖ Bridge decks without an overlay. 	<p>Because the specific purpose of this standard is for prediction of the presence or absence of concrete or rebar deterioration due to corrosion, it is a suitable choice in cases where corrosion damage to the rebars is more susceptible, expected, or observed considering the environmental conditions in the state of Georgia.</p>	Application
<p>It is of particular interest in bridge deck condition investigations to locate not only the areas of active reinforcement corrosion but also areas of chloride-contaminated and otherwise deteriorated concrete.</p>	<p>A preliminary assessment of the potential areas including both possible active corrosion and chloride-contaminated areas is recommended to determine the best scanning area using GPR.</p>	Consideration
<p>This test method may not be suitable for the following cases:</p> <ul style="list-style-type: none"> ❖ Bridges with delamination that are localized over the diameter of the reinforcement. ❖ Bridges that have cathodic protection (coke breeze as cathode) installed on the bridge. ❖ Bridges on which a conductive aggregate has been used in the asphalt (that is, blast furnace slag). <p><i>This is because metals are perfect reflectors of electromagnetic (EM) waves, since the wave impedances for metals are zero.</i></p>	<p>As mentioned in the standard, any point or localized reflector of EM wave (such as active cathode, high voltage wires, metals, and large local corrosions) will be a limiting factor.</p>	Limitation
<p>A precision and bias statement has not been developed at this time. Therefore, this standard should not be used for acceptance or rejection of a material for purchasing purposes.</p>	<p>No approval or rejection of a material solely based on this standard is recommended. Additional investigation will be required for material approval purposes.</p>	Limitation
<p>The values stated in SI units are to be regarded as standard. No other units of measurement are included in this standard.</p>	<p>Only SI units are applicable. This must be considered while using this standard for inspection or for inspection with any particular GPR device.</p>	Consideration
<p>This standard does not purport to address all of the safety concerns.</p>	<p>All safety concerns and considerations must be checked by an approved safety officer before any action.</p>	Consideration/ Limitation

This test method predicts the presence or absence of concrete or rebar deterioration at or above the level of the top layer of rebar.

Summary of Test Method

Sections 2 and 2.1 of the ASTM D6087 standard describe the test method as summarized in table 5.

Table 5. Summary of test method in ASTM D6087.

Standard Language	Note/Discussion	Remark
The data collection equipment consists of: <ul style="list-style-type: none">❖ Short-pulse GPR device.❖ Data acquisition device.❖ Recording device.❖ Data processing and interpretation equipment.	The majority of recent GPR devices that are commercially available include all of these components in a single package. Operator must check the device before any further actions.	Consideration
The user makes repeated passes with the data collection equipment in a direction parallel or perpendicular to the centerline across a bridge deck at specified locations.		Consideration
Bridge deck condition is <i>quantified</i> based on the data obtained.	The GPR device must have the capability to <i>quantify</i> the results in terms of meaningful values.	Consideration

Significance and Use

Important points in significance and use of ASTM D6087 are summarized in table 6.

Table 6. Significance and use of ASTM D6087.

Standard Language	Note/Discussion	Remark
This test method provides information on the condition of: <ul style="list-style-type: none">❖ Concrete bridge decks overlaid with asphaltic concrete.❖ Bridge decks without overlays and with Portland cement concrete overlays.	Interpretation of GPR results for each of these conditions requires an adequate experience with GPR operation and science of work. An experienced operator or adequate training is recommended.	Consideration
Information on the condition of asphalt-covered concrete bridge decks is needed to estimate bridge deck condition for maintenance and rehabilitation, to provide cost-effective information necessary for rehabilitation contracts.	Same as above	Consideration

Apparatus

Characteristics of the apparatus required by ASTM D6087 are summarized in table 7.

Table 7. Characteristics and requirements of the required apparatus according to ASTM D6087.

Standard Language	Note/Discussion	Remark
GPR system can be either: ❖ GPR using air-launched horn antennas with center frequencies 1 GHz and greater ❖ GPR using ground-coupled antennas with center frequencies 1 GHz and greater	Per standard requirement, <i>sufficient center frequency to provide the accurate measurement of a 5 cm thick asphalt pavement</i> is needed. The actual detection range must be confirmed and discussed by the officials to make sure there is enough penetration and detection depth available with the device being used.	Consideration
A data acquisition system, consisting of equipment for gathering GPR data at the minimum data rates specified in Sections 4.1.1 and 4.1.2.	Data rates are not directly mentioned in Sections 4.1.1 and 4.1.2. It is recommended that the data acquisition and processing rate be checked in the device, specifically at higher operating frequency.	Consideration-Limitation
The system shall be capable of accurately acquiring GPR data with a minimum of 60 dB dynamic range.	60 dB dynamic range is a typical range for GPR. A higher range might be required based on different environmental effects and noise. 80–100 dB is recommended.	Consideration
A distance measurement system consisting of a fifth-wheel or appropriate distance measurement instrument (DMI) with accuracy of $\pm \pm 100$ mm/km and a resolution of 25 mm is required.	DMI must be provided and checked before the tests.	Consideration

Figure 2 shows the block diagram of GPR and support equipment as demonstrated in ASTM D6087 [20].

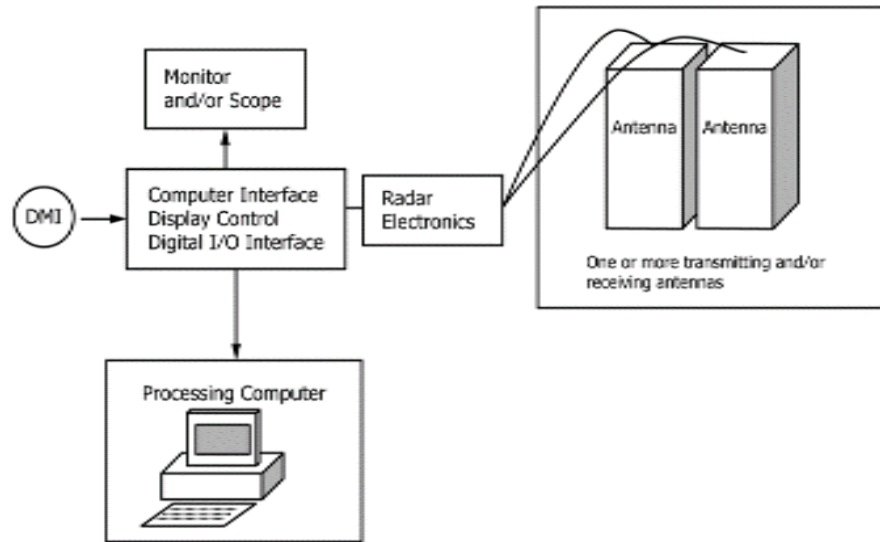


Figure 2. Block diagram. GPR and support equipment as demonstrated in ASTM D6087.

Hazards

Potential, but not limited to, hazards are summarized in table 8.

Table 8. Potential, but not limited to, hazards while operating GPR according to ASTM D6087.

Standard Language	Note/Discussion	Remark
Observe the manufacturer's safety directions at all times.	Study the manufacturer's safety protocol in addition to any case specific to the test site.	Consideration
When conducting inspections, ensure that appropriate traffic protection is utilized in accordance with the accepted standards.	Traffic control plans including signs and signals must be prepared in advance.	Consideration-Limitation
EM emissions from the GPR apparatus, if the system is improperly operated, could potentially interfere with commercial communications, especially if the antenna is not properly oriented toward the ground. Ensure that all such emissions from the system comply with Part 15 of the Federal Communications Commission (FCC) Regulations.	<i>Part 15 of the Federal Communications Commission (FCC) Regulations</i> must be considered when operating the GPR.	Consideration-Limitation

Procedure

The recommended procedure of testing and relevant considerations are summarized in table 9.

Table 9. The recommended procedure of GPR testing and relevant considerations according to ASTM D6087.

Standard Language	Note/Discussion	Remark
Cleaning/Preparation: ❖ If soil, aggregate, or other particulate debris is present on the bridge deck surface, clean the bridge deck.	Adequate arrangement for cleaning must be considered before the tests.	Consideration
Surface Condition: ❖ Test the bridge deck in a surface dry condition.	Weather forecast (or season) must be considered before the tests. <i>This will reduce the influence of wet interfaces on EM waves and signals.</i>	Consideration
System Performance Compliance: ❖ The system should be calibrated and performance verified in accordance with the manufacturer's recommendations and specifications.	Sections 6.2.1 through 6.2.4 and 6.3 provide recommendations for typical calibration procedures for different types of systems. Compliance with those procedures is not required and the <i>manufacturer's calibration procedure takes preference.</i>	Consideration
GPR Data Acquisition Air-launched Antenna Systems ❖ GPR inspection passes in a longitudinal direction parallel to the centerline of the bridge deck. ❖ Antenna mounted to maintain a manufacturer-recommended distance from the bridge deck surface. ❖ Use a transverse distance (dt) between GPR inspection passes; $<1\text{ m}$ is suggested. ❖ Use a longitudinal distance (dl) between GPR scans $\leq 150\text{ mm}$. ❖ Determine the starting location for passes, that is, at abutments, joints, or a predetermined location. ❖ Determine the optimum speed of operation for contiguous longitudinal coverage based on GPR range sweep rate and the scan-spacing.	❖ Pre-assessment of scanning passes is recommended. ❖ Familiarity with technical specification of the GPR device and experience with its operation is strongly recommended.	Consideration

Standard Language	Note/Discussion	Remark
<p>GPR Data Acquisition</p> <p>Ground-coupled Antenna Systems</p> <ul style="list-style-type: none"> ❖ Make GPR inspection passes either parallel to the direction of traffic or perpendicular to the direction of traffic, depending on the direction of the top layer of reinforcing. ❖ The pass direction should be chosen so that the antenna crosses over the top layer of reinforcing at an angle nearest to 90°. ❖ Use a transverse distance (dt) between GPR inspection passes $< 0.6\text{ m}$. ❖ Use a longitudinal distance (dl) between GPR scans necessary to obtain sufficient data; $< 150\text{ mm}$ is suggested. ❖ Determine the starting location for passes, i.e., at abutments, joints, or a predetermined location. 	<ul style="list-style-type: none"> ❖ Pre-assessment of scanning passes is recommended (refer to table 4 and table 5). ❖ Familiarity with technical specification of the GPR device and experience with its operation is strongly recommended. 	Consideration

Signal-to-noise ratio (SNR) of the GPR device must be tested and confirmed before the testing according to equation 1.

Equation 1. SNR.

$$\frac{\text{Signal Level } (A_m)}{\text{Signal Level } (A_n)} > 20 \text{ (26.0 dB)}$$

Data Processing

Accepted GPR data processing methodologies and the procedure of their implementation are summarized in table 10 and figure 3.

Table 10. Accepted GPR data processing methodologies.

Standard Language	Note/Discussion	Remark
There are two different accepted GPR data processing methodologies. Both methods employ reflection amplitudes.	<ul style="list-style-type: none"> ❖ GPR device must be capable of operating in reflection mode. ❖ Device must be set to operate in reflection mode by the operator. 	Consideration
The bottom deck reflection attenuation technique calculates deterioration based on the relative reflection amplitudes from the bridge deck bottom relative to the bridge deck surface.	<ul style="list-style-type: none"> ❖ Technical operating setup of the device and the operating frequency must be set such that the bottom deck reflection can be detected and reached. ❖ Procedure described in Section 7.2 must be used for this method. 	Consideration
<p>The top reinforcing reflection attenuation technique, utilizes the relative reflection amplitudes from the top layer of reinforcing to assess deterioration.</p> <ul style="list-style-type: none"> ❖ Air-Launched Antenna Data <ul style="list-style-type: none"> ○ Can be used when the dominant deck reinforcing steel is aligned transversely to the direction of the movement of the antenna and has uniform density in that direction, such as occurs for decks supported by concrete or steel girders. ○ For decks in which dominant steel is longitudinal, i.e., parallel to the direction of travel (such as one-way slabs and arch slabs), the method of this section is not appropriate. <i>This is because the density of top steel varies with longitudinal position.</i> 	<ul style="list-style-type: none"> ❖ An accurate detection and determination of reflection from the top reinforcing must be achieved. ❖ Procedure described in Section 7.3 must be used for this method. ❖ The alternate methods for decks with longitudinal dominant steel is either the method of Section 7.2 (bottom reflection), or to use the ground-coupled antenna with the method of Section 7.3.3, with survey lines transverse to the direction of travel. ❖ For more information refer to 	Consideration

Figure 3 shows the flowchart of accepted GPR data processing methodologies.

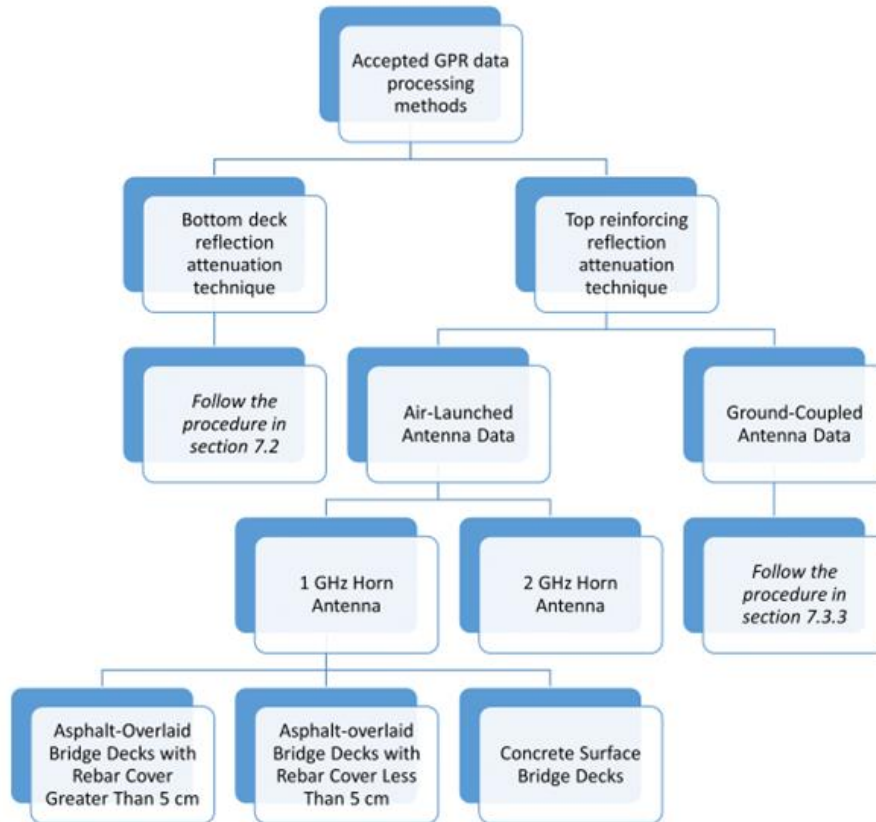


Figure 3. Flowchart. Accepted GPR data processing methodologies.

Report

Minimum requirement of reports is summarized in table 11. Client requirement must be followed for other requirements.

Table 11. Minimum requirement of reports.

Standard Language	Note/Discussion	Remark
Report, as a minimum, the following conditions and parameters: <ul style="list-style-type: none">❖ Bridge identification and location.❖ Date and weather conditions.❖ General deck status relative to moisture and debris.❖ Any unusual conditions or circumstances.		
Report, as a minimum, the GPR results in the following forms: <ul style="list-style-type: none">❖ Percent of bridge deck area delaminated at top steel.❖ Bridge deck area, in square meters deteriorated, at top steel.❖ Total bridge deck area, in square meters deteriorated for the bridge deck at top steel.❖ Plan view map of bridge deck, depicting GPR inspection pass versus longitudinal distance and showing location and extent of detected deterioration at top steel. <i>A color-coded contour map is suggested.</i>		

Precision and Bias

Requirements for precision and bias are summarized in table 12.

Table 12. Requirements for precision and bias.

Standard Language	Note/Discussion	Remark
Precision <ul style="list-style-type: none">❖ The processing techniques described in Section 7 are suggested methods.❖ If applicable, however, other techniques can be utilized.		
Bias <ul style="list-style-type: none">❖ The research necessary to determine the bias of this test method has not been performed.		

System Performance Compliance

Signal-to-Noise Ratio Test

Position the antenna at its far field distance approximately equal to the maximum dimension of the antenna aperture above a square metal plate with a width 4× the antenna aperture, minimum.

Turn on the GPR unit and allow it to operate for a 20-min warm-up period for the time recommended by the manufacturer. After warming up the unit, record 100 waveforms. Then

evaluate the recorded waveform for SNR. The SNR is described by equation 1. This will be performed on each of the 100 waveforms, and the average SNR value of the 100 waveforms will be taken as the “signal-to-noise of the system.” Noise voltage (A_n) is defined as the maximum amplitude occurring between the metal plate reflection and region up to 50 percent of the time window after the metal plate reflection normally used within the antenna (i.e., $1.0 \text{ GHz}/20 \text{ ns} = 10 \text{ ns}$). The signal level (A_{mp}) is defined as the amplitude of the echo from the metal plate. The SNR test results for the GPR unit should be greater than or equal to 20 (+26.0 dB) (equation 1).

The warm-up period describes the time it takes for the equipment to stabilize before operating and collecting results. The far field distance of an antenna describes the distance between the transmitting antenna and the far field region, which is the farthest area the antenna is influenced by the electromagnetic (EM) field. A representation of this is shown in figure 4. The start of the far field region can be found with equation 2.

Equation 2. Far field region.

$$r = \frac{2D^2}{\lambda}$$

where,

r = distance from center of antenna to beginning of far field region,

D = maximum linear antenna dimension, and

λ = wavelength of EM waves.

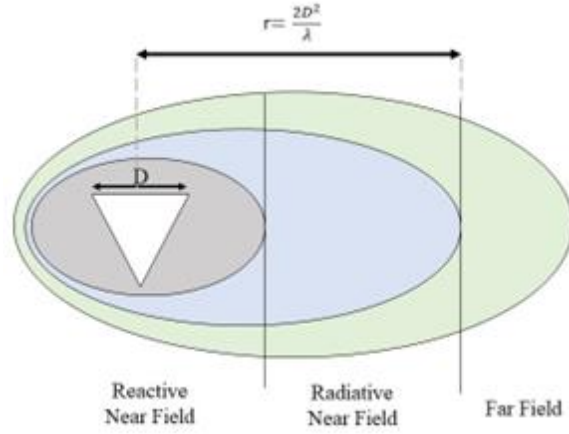


Figure 4. Diagram. Near field and far field regions of antenna.

For interpretation of the signal (A_{mp}) and noise (A_n) level values, an example is shown in figure 5 as presented by Pajewski et al. [21]. Figure 5(a) shows the antenna and metal plate setup. The distance, h , from the antenna to the metal plate is described with equation 3.

Equation 3. Distance from antenna to metal plate.

$$h = 3\lambda_c$$

where,

λ_c = wavelength at the central frequency and

c = light velocity in air.

The size of a square metal reflector is shown by equation 4.

Equation 4. Size of a square metal reflector.

$$L = 2\sqrt{5} \cdot \lambda_c$$

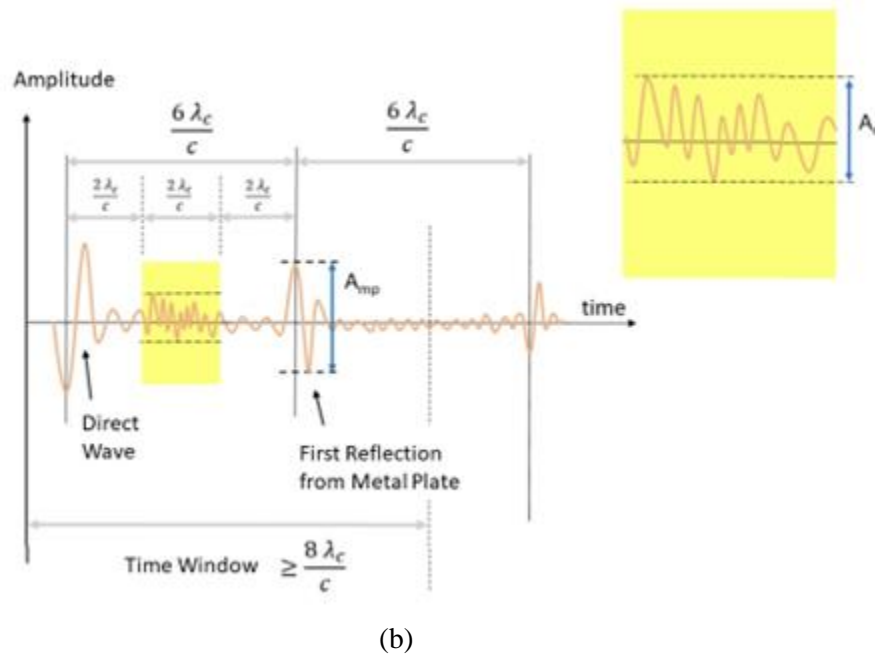
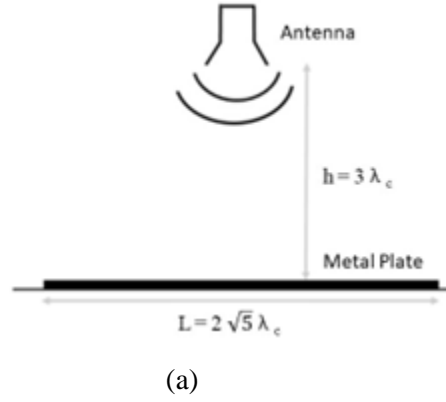


Figure 5. Diagram and graph. SNR test: (a) antenna and metal plate principle and (b) amplitude versus time graph [21].

In figure 5(b), the amplitude graph for this scenario is shown, where $2\lambda_c/c$ [s] indicates the suggested relevant time window after the absolute maximum amplitude of the signal. The time window should be at least twice the two-way travel time (TWTT) from the antenna to the metal plate, which is shown to be $8\lambda_c/c$. The signal level, A_{mp} , is shown as the average peak-to-peak amplitude of the first echo from the metal plate. The noise level, A_n , is shown in the section

highlighted in yellow, where it is defined as the average peak-to-peak amplitude of the noise over the relevant time window.

In an example laboratory experiment for analyzing the SNR with an air-coupled antenna system (see figure 6), the radar box was placed 30 cm above a copper sheet to be the perfect electric conductor (PEC), allowing for complete reflection of propagation waves [22]. The authors recorded signal responses at different heights to evaluate the signal stability. In accordance with ASTM D6087, the signal and noise peaks for 100 traces were evaluated to confirm the applicability of the SNR methodology outlined in the standard.

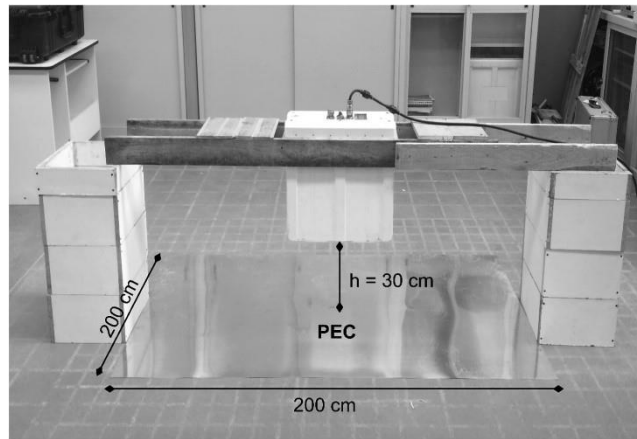


Figure 6. Drawing. Laboratory setup for analyzing SNR with a distance of 30 cm between radar box and copper sheet [22].

Signal Stability

Use the same test configuration as described in the SNR test. Record 100 traces at the maximum data acquisition rate. Evaluate the signal stability using equation 5.

Equation 5. Signal stability criteria.

$$\frac{A_{max} - A_{min}}{A_{ave}} < 0.01 \text{ (1\%)}$$

where,

A_{\max} = maximum amplitude of the metal plate reflection for all 100 traces,

A_{\min} = minimum amplitude of the metal plate reflection for all 100 traces, and

A_{avg} = average trace amplitude of all 100 traces.

The signal stability test results for the GPR system should be ≤ 1 percent.

An example of the amplitudes produced from 100 radar traces is shown in figure 7, completed by Benedetto and Tosti from the same experiment mentioned above. The authors used a GPR system with 1 GHz frequency and moved the antenna to three different distances from the metal plate: 30, 40, and 50 cm. From these data of the normalized signal amplitudes, the maximum, minimum, and average amplitudes can be found, from which the signal stability can be calculated.

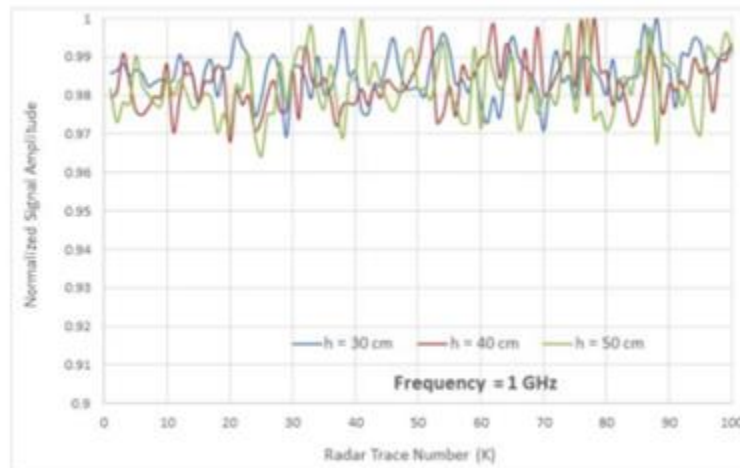


Figure 7. Graph. Normalized (to 1) amplitude variations for 100 consecutive radar traces of the signal peak with 1 GHz GPR system with varying heights of the antenna [22].

Linearity in the Time Axis and Time Window Accuracy

Variations in Time Calibration Factor

Use the same test configuration as described in the SNR test, except the metal plate can be replaced by any reflecting object. Collect a single waveform and measure the distance from the antenna to the reflector. Perform this test for three different distances corresponding to approximately 15, 30, and 50 percent of the time window normally used with the system. The time delay between the echo from the aperture of the transmitting antenna and that from the reflecting object is measured as time t_1 (where subscript 1 represents position 1, and so forth). The differences between t_2 and t_1 and between t_3 and t_2 represent the travel time for a fixed distance in air. The factor C_i represents the speed between distance i and $i+1$. The allowable variation in measured speed is shown in equation 6.

Equation 6. Allowable variation in measured speed.

$$\frac{C_1 - C_2}{\text{Mean of } C_1 \text{ and } C_2} < 2\%$$

where,

$$C_1 = \frac{\text{Distance from Position 2 to Position 1}}{T_1}$$

$$C_2 = \frac{\text{Distance from Position 2 to Position 2}}{T_2}$$

The variation in time calibration factor should be <2 percent.

More specifically, the time delay can be described as the difference between the absolute maximum amplitude of the direct wave and the absolute maximum amplitude from the metal plate reflection. Pajewski et al. [21] created amplitude versus time graphs for the linearity in the

time axis procedure as shown in figure 8. Figure 8(a), (b), and (c) differ due to the distance from the antenna to the metal plate reflector, which are as follows: $2\lambda_c$, $3\lambda_c$, and $2.5\lambda_c$, consecutively. The time window in this example is at least twice the TWTT at the longest distance, which results in a time window of at least $12\lambda_c/c$.

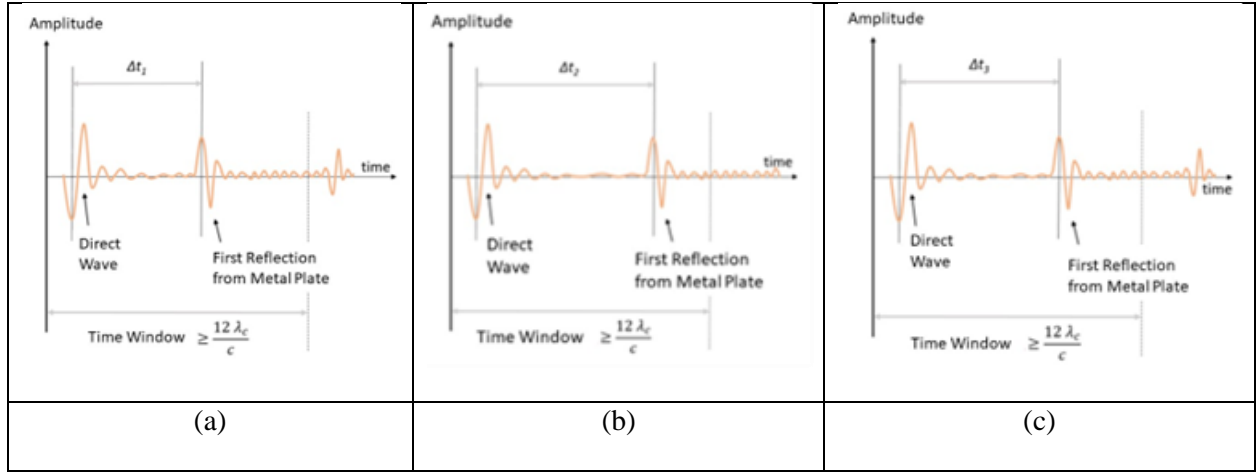


Figure 8. Graphs. Linearity in the time axis and time window: amplitude and time window graphs for (a) position 1: $2\lambda_c$; (b) position 2: $3\lambda_c$; and (c) position 3: $2.5\lambda_c$ [21].

Long-term Stability Test

Long-term Amplitude Variation

Use the same test configuration as described in the SNR test. Switch on the GPR and allow it to operate for 2 h continuously. As a minimum, capture a single waveform every 1 min, 120 total. Calculate the amplitude of a metal plate reflection and plot against the time for each waveform. For the system to perform adequately, the amplitude of reflection should remain constant after a short warm-up period. The stability criterion is as in equation 7.

Equation 7. Signal stability criterion.

$$\frac{A_{max} - A_{20}}{A_{20}} < 0.03 \text{ (3\%)}$$

where,

A_{20} = amplitude measured after 20 min and

A_{\max} = largest amplitude measured between 20 and 120 min.

Pre-operation Measurement

Free Space Signal (FSP)

The equipment manufacturer may require the GPR antenna to be mounted in an operational configuration and 100 waveforms be gathered in the absence of the material to be inspected. Use the average of 100 waveforms as a template for clutter removal.

Flat Metal Plate (FMP)

Position the GPR in an operation configuration and gather 100 waveforms while illuminating a flat plate with dimensions recommended by the manufacturer. This is a measure of the emitted energy to be used in subsequent measurements and as a template for decorrelation or background removal, or both. Clutter removal involves signal processing methods to reduce the clutter of a reflected signal. Some of these processing methods can include time-zero correction, background removal, and deconvolution. A general flowchart for the data processing of the GPR raw data is shown in figure 9.

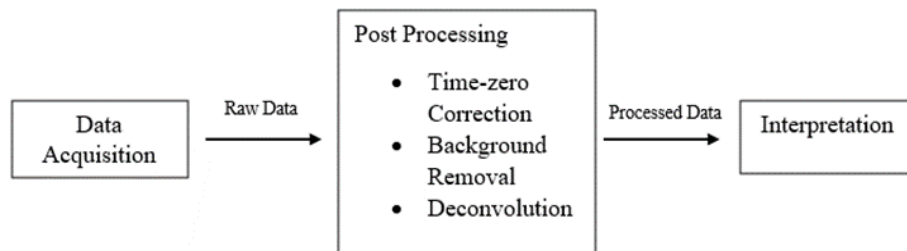


Figure 9. Flowchart. GPR data processing scheme for clutter removal.

GPR Data Acquisition

Air-launched Antenna System

- Make GPR inspection passes in a longitudinal direction parallel to the centerline of the bridge deck with the antenna mounted to maintain a manufacturer-recommended distance from the bridge deck surface.
- Use a transverse distance (dt) between GPR inspection passes (<1 m is suggested).
- Use a longitudinal distance (dl) between GPR scans ≤ 150 mm.
- Determine the starting location for passes (i.e., at abutments, joints, or predetermined location).
- Determine the optimum speed of operation for contiguous longitudinal coverage based on the GPR range sweep rate and the scan spacing.

Figure 10 shows a schematic representing the surveying procedure for air-launched antenna systems as mentioned in Section 6.4.1, where “T” is the transmitting antenna and “R” is the receiving antenna.

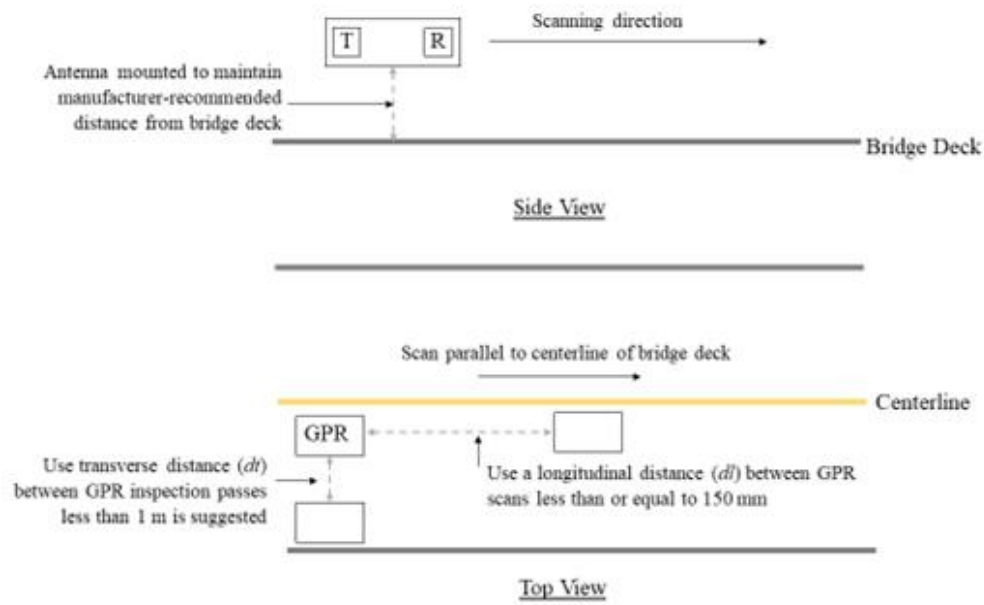


Figure 10. Diagram. GPR inspection passes for air-launched antenna systems.

Ground-coupled Antenna Systems

- Make GPR inspection passes either parallel to the direction of traffic or perpendicular to the direction of traffic, depending on the direction of the top layer of reinforcing. The pass direction should be chosen so that the antenna crosses over the top layer of reinforcing at an angle nearest to 90°.
- Use a transverse distance (dt) between GPR inspection passes <0.6 m.
- Use a longitudinal distance (dl) between GPR scans necessary to obtain sufficient data (<150 mm is suggested).
- Determine the starting location for passes (i.e., at abutments, joints, or a predetermined location).

A simple diagram to represent the direction of scanning is shown in figure 11. The “T” represents the transmitting antenna, and the “R” represents the receiving antenna as the GPR surveys the bridge deck and crosses over the embedded rebar.

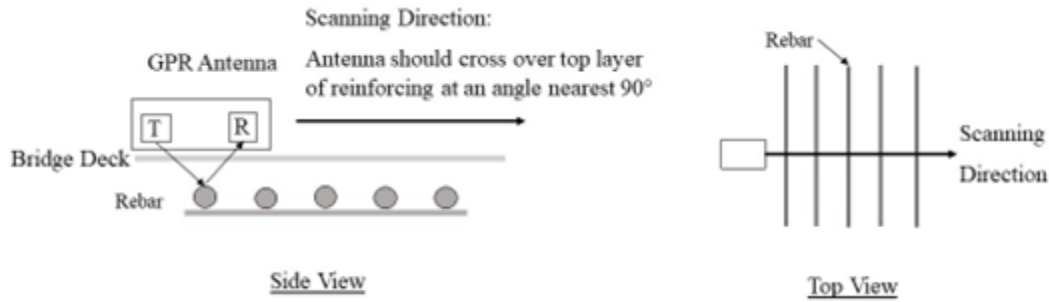


Figure 11. Schematic diagram. GPR antenna passing over embedded rebar at 90° angle.

The data acquisition for ground-coupled antenna systems is illustrated in figure 12.

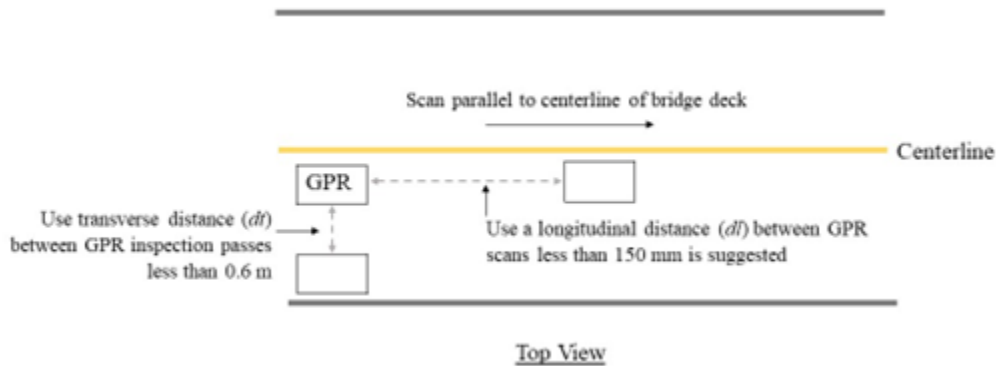


Figure 12. Diagram. GPR inspection passes for ground-coupled antenna systems.

Data Processing

There are two accepted GPR data processing methodologies. Both methods employ reflection amplitudes. The first method, the bottom deck reflection attenuation technique, calculates deterioration based on the relative reflection amplitudes from the bridge deck bottom relative to the bridge deck surface. The second method, the top reinforcing reflection attenuation technique, utilizes the relative reflection amplitudes from the top layer of reinforcing to assess deterioration.

Deterioration Measurements at Top Reinforcing Steel using the Bottom Deck Reflection Attenuation Technique

The process is to measure and record the applied signal strength, V_t , at the deck surface, and then measure and record the maximum signal strength of the deck bottom echo, V_{bs} . If V_{bs} is $\geq 0.0264 V_t$ for a longitudinal GPR inspection pass, proceed to Section 7.2.5.¹ If V_{bs} is $< 0.0264 V_t$ after repeating the longitudinal GPR inspection pass, the data are not reliable for determining removal quantities of bridge deck concrete. Processing of the data will require an alternative technique, such as the one described in Section 7.3 of this test method or that described in Ontario Ministry of Transportation (MTO) reports. Measure and record the amplitude of the deck bottom echo, V_b , for each waveform, then determine delamination at the top reinforcing steel using the attenuation technique. Consider the concrete delaminated if equation 8 is true.

Equation 8. Delamination criterion.

$$V_b \leq 0.385V_{bs}$$

where,

V_b = bottom echo amplitude;

V_{bs} = bottom echo maximum amplitude, all scans; and

0.385 = a constant derived from research data.

Calculate the percent delaminated at the top steel in each GPR inspection pass using equation 9.

Equation 9. Percent delamination.

$$X_{tn} = [(W_{dt}) / (W_{dt} + W_{st})] \times 100$$

¹ The number 0.0264 is a constant derived from research data.

where,

X_{tn} = percent delaminated in a GPR inspection pass, n , at top steel;

n = GPR inspection pass identification number;

W_{dt} = concrete delaminated at top steel, m ; and

W_{st} = sound concrete at top steel, m .

Calculate the estimated quantity of deck delaminated at top steel for each GPR inspection pass using equation 10.

Equation 10. Estimated quantity of deck delaminated at top steel.

$$Q_t = X_m L_m d_t$$

where,

Q_t = square meters of deck delaminated at top steel;

L_m = length of GPR inspection pass m ; and

d_t = transverse distance between GPR inspection passes, m .

Calculate the total estimated quantity of deck delaminated at top steel using equation 11.

Equation 11. Estimated quantity of deck delaminated at top steel.

$$Q_{Tt} = \sum Q_t$$

where,

Q_{Tt} = total square meters of deck delaminated at top steel for all GPR inspection passes.

Deterioration Measurements at or above Top Reinforcing Steel Using the Top Reinforcing Reflection Attenuation Technique

Extract the reflection amplitudes from the top layer of reinforcing.

Air-launched Antenna Data

This method can be used when the dominant deck reinforcing steel is aligned transversely to the direction of the movement of the antenna and has uniform density in that direction, such as occurs for decks supported by concrete or steel girders. For decks where the dominant steel is longitudinal (i.e., parallel to the direction of travel, such as one-way slabs and arch slabs), the method of this section is not appropriate. This is because the density of top steel varies with longitudinal position. The alternate method for these decks is to use either the method of Section 7.2 (bottom reflection) or to use ground-coupled antenna with the method of Section 7.3.3 with survey lines transverse to the direction of travel.

1 GHz Horn Antenna

1. *Asphalt-Overlaid Bridge Decks with Rebar Cover >5 cm*—One antenna is required per lane position. The antenna must be positioned with its radiated polarization parallel or nearly parallel to the orientation of the top layer of reinforcing. Data post-processing incorporates the subtraction of a metal plate reflection from each scan.
2. *Asphalt-Overlaid Bridge Decks with Rebar Cover <5 cm*—Due to possible interference between the asphalt concrete interface reflection and the rebar reflections, data collected under these conditions with the air-launched horn antenna system must be obtained with two antennas positioned of the asphalt surface reflection. This method may not be reliable for bridge decks containing longitudinal rebar on top of transverse rebar with on-center spacings greater than 20 cm. For this situation, ground-coupled antenna data should be collected in the direction transverse to traffic flow or data should be collected and

evaluated using the methodology presented in Section 7.2. If the trend of the top layer of reinforcing is not near 45° relative to the direction of traffic: (a) normalize the asphalt reflection amplitude of the antenna polarized parallel to the top layer of reinforcing relative to (b) the same reflection amplitude in the (1) other antenna and subtract (b) from (a) for each data scan. This is done to isolate the reflection from the top layer of reinforcing from the asphalt bottom reflection. For the top layer of reinforcing angles near 45° , no subtraction should be performed. However, for this case, if the reinforcing reflection amplitudes cannot visually be differentiated from the asphalt bottom reflection, this method may not be reliable, and the data should be analyzed using the methodology presented in Section 7.2 or ground-coupled antenna data should be collected.

3. *Concrete Surface Bridge Decks*—This designation includes decks without overlays and decks with Portland cement concrete overlays. A single antenna per lane position suffices for this condition regardless of rebar cover because, in the case of a concrete overlay, the reflection between the concrete overlay and the concrete deck does not significantly affect the rebar reflection. Only one antenna is required per lane position. The antenna must be positioned with its radiated polarization parallel or nearly parallel to the orientation of the top layer of reinforcing. Data post-processing incorporates the subtraction of a metal plate reflection from each scan. This method may not be suitable for bridge decks containing longitudinal reinforcing on top with on-center spacings greater than 20 cm.

2 GHz Horn Antenna

Data are obtained with one antenna per lane position. During data collection, the antenna is oriented such that its radiated polarization is parallel or nearly parallel to the top layer of

reinforcing. Data post-processing incorporates the subtraction of a metal plate reflection from each scan. This method has not been tested on bridge decks containing the top layer of reinforcing oriented in the longitudinal direction.

Record the highest amplitude reflections from the top layer of reinforcing in the data from the antenna polarized most nearly parallel to the trend top reinforcing.

Ground-coupled Antenna Data

The two types of migration algorithms are time migration and depth migration. The time migration algorithm is based on the root mean square (RMS) velocity and the depth migration algorithm uses interval velocity [23]. RMS velocity considers the average velocity of the upper layer's instantaneous velocity, whereas the interval velocity is the reflection of the actual velocity of only one layer. Record the reflection amplitudes from the scan most nearly centered over each reinforcing steel member detected in the data.

An example of a GPR line scan is shown in figure 13, where the reflections from the rebar can be seen. This scan was performed on a concrete floor in the Engineering and Research Building at Georgia Southern University (GSU). This floor consists of 3.5 inches of concrete (145 PCF) slab reinforced with #3 rebar at 18 inches on center, each way. The rebar can be seen as the top reflections on the black and white radargram, where the center of the hyperbolic shape is the rebar. Beneath the slab is a 3 inch 20 gage galvanized steel composite floor deck, in which those reflections can also be seen. To the left is the A-scan data output, where the green represents the signal and the red is the envelope.

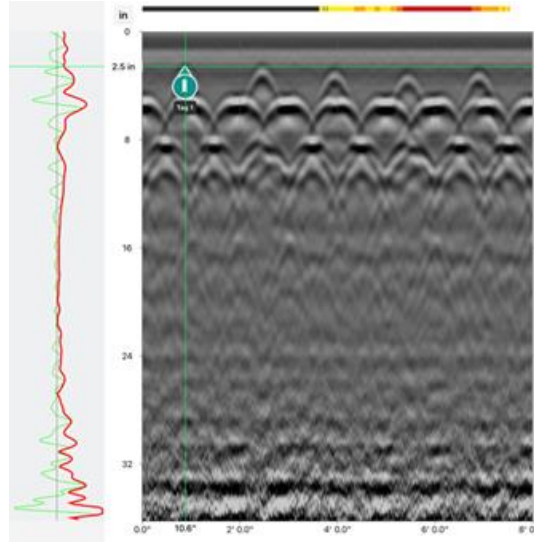


Figure 13. Line scan. A-scan and radargram output from GPR surveying on 8 ft of RC floor.

Calculate the deterioration threshold and convert the reflection amplitudes to decibels according to equation 12.

Equation 12. Convert reflection amplitudes to decibels.

$$A_{db} = 20 \log_{10}(A)$$

where,

A_{db} = reflection amplitude in decibels and

A = reinforcing reflection amplitude in data units.

The amplitudes of the reinforcing reflections along each pass provide a gradational scale. The lower the reflection amplitude, the higher the likelihood of deterioration. The spatial location of scans containing reflection amplitude less than 6–8 dB below the maximum reflection amplitudes recorded typically correspond to deterioration detected using other information, such

as (1) bridge deck bottom inspection results, (2) core data when possible, and (3) results from other deterioration assessment techniques to refine the threshold value.

Figure 14 illustrates how the reflection amplitudes will appear when there is sound concrete versus signs of deterioration [24]. As mentioned above, a higher reflection amplitude produced from the rebar indicates sound concrete, whereas a lower reflection amplitude likely shows signs of deterioration.

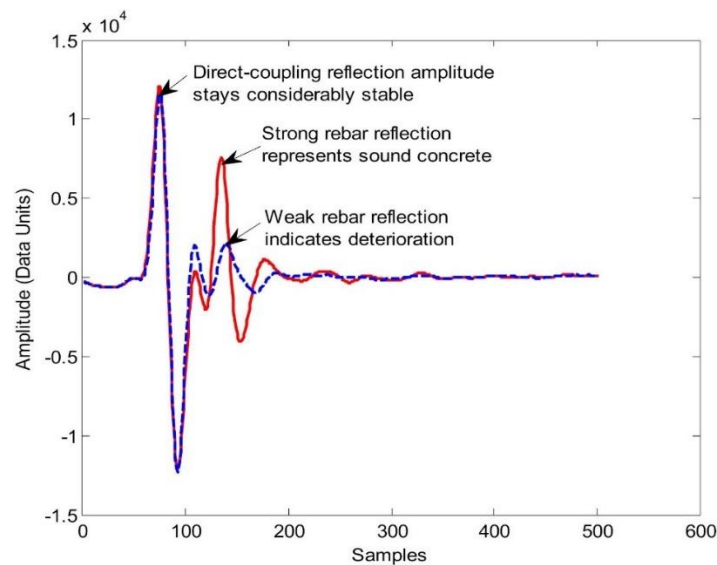


Figure 14. Graph. Effects of deterioration on GPR signal amplitude [24].

Similarly, this information can be observed on the B-scan image produced from the GPR, and an example is shown in figure 15 [25]. The hyperbolic signature for rebar in sound concrete is distinct because there is a strong reflection. Comparably, if there is a weak reflection from the rebar, the hyperbolic signatures are not as visible.

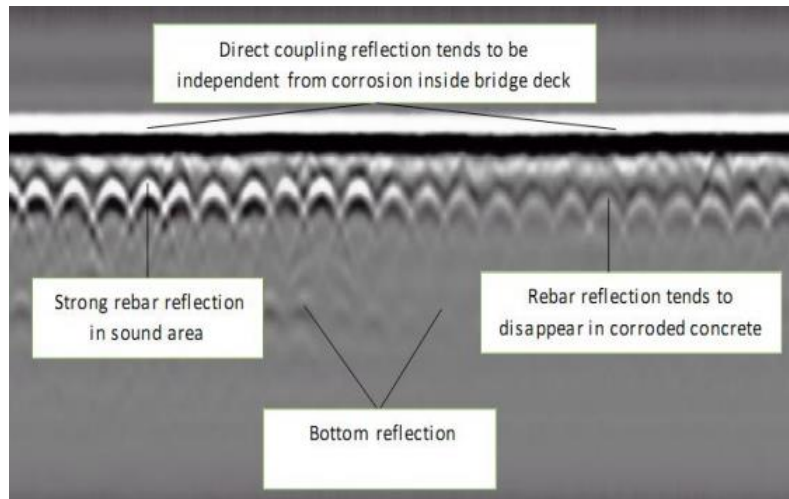


Figure 15. B-scan image. Bridge deck [25].

Create a contour map of the reflection amplitudes versus spatial location on the bridge deck. Locations of deteriorated areas correspond to reflection amplitudes less than threshold value.

For the evaluation of bridge deck corrosiveness, the creation of contour maps is possible by analyzing the amplitudes created from GPR scanning. An example of this application has been studied by Abouhamad et al. [13]. Numerical-amplitude analysis was performed to create the attenuation map, in which lower amplitudes from the scans signified deteriorated concrete. The attenuation map for both sides of the bridge deck is shown in figure 16, where the red and purple colors indicate severe deterioration because the amplitudes are significantly lower according to a predetermined threshold. The attenuation of the GPR reflections at the top reinforcement is often used for assessing the condition.

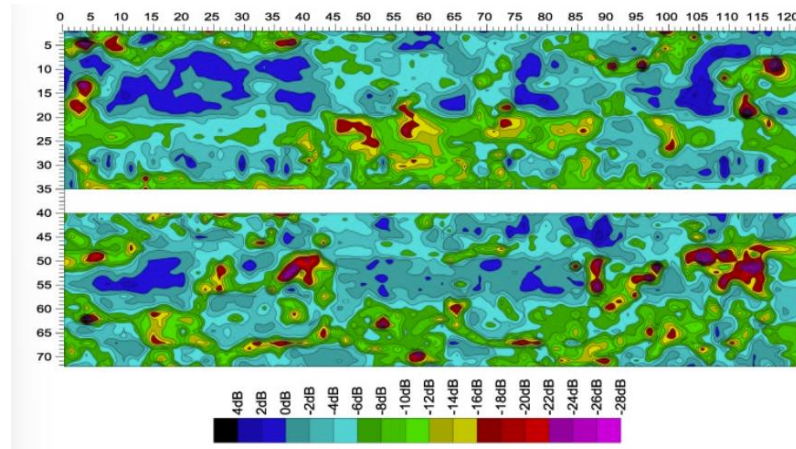


Figure 16. Map. GPR results of a bridge deck: attenuation map using amplitude analysis [13].

Calculate the percent deterioration at or above the top steel in each GPR inspection pass using equation 9. Estimate the quantity of deck deteriorated at or above the top reinforcing using equation 10 and equation 11.

A Venn diagram is presented in figure 17 to distinguish which sections outlined in the ASTM D6087 standard are to be utilized for the different GPR antenna systems: air-launched and ground-coupled.

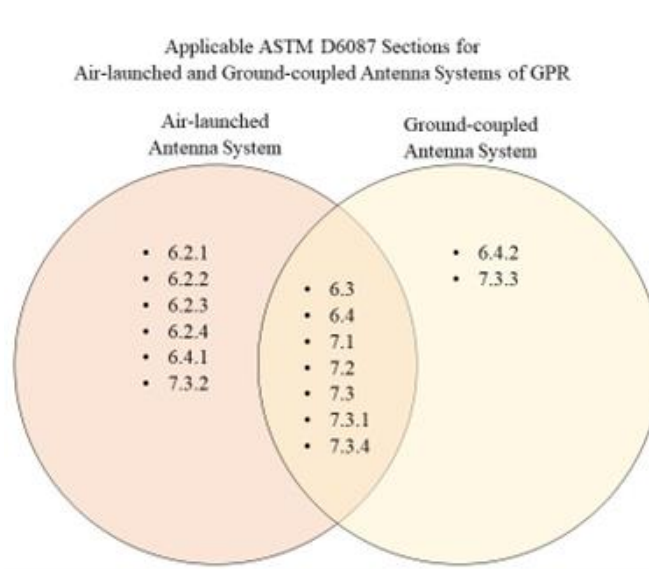


Figure 17. Venn diagram. Comparison of the sections outlined in ASTM D6087 in which GPR system they are to be applied.

Challenges

- *Interpretation of Data*—Before utilizing GPR equipment and interpreting the scans, the user must have an understanding of the behavior of the GPR reflections and signals to properly judge the condition of the material being tested.
- *Obtaining Amplitude Values*—Although the Proceq software application allows the user to see A-scan data format of a scan, there is no numerical amplitude data accessible on the app or easily available from the files.
- *Image Processing Software Purchase*—Available software packages are beneficial for image processing of the GPR data. Specifically, two of these of interest are GPR Slice

and GPR Insight. These may be necessary for analyzing quantitative data of the reflection amplitudes.

ASSESSMENT OF ASTM D4748 STANDARD

The ASTM D4748 standard specifies GPR as the preferred NDT method for measuring the thickness of bound pavement layers, such as bituminous concrete, Portland cement concrete, and stabilized bases. However, due to the increased attenuation of the EM signal, high-conductivity pavements may not be suitable for this test method.

Apparatus

The apparatus may consist of a vehicle or a cart equipped with the following equipment.

GPR Antennas—One or more antennas mounted on the vehicle, cart, or a trailer for this application, which typically have a center frequency that ranges 1.0–2.6 GHz. A typical 1.0 GHz antenna usually has a resolution sufficient to determine a minimum layer thickness of 40 mm (1.5 inch) to an accuracy of ± 5.0 mm (± 0.2 inch). Antennas emitting short pulses containing a center frequency of 2.0 GHz and higher provide resolution sufficient for determination of a minimum layer thickness < 25 mm (1.0 inch) to an accuracy of ± 2.5 mm (± 0.1 inch).

The frequency of a GPR system is an important parameter to understand before choosing suitable equipment for testing due to the correlation between antenna frequency, penetration depth, and the resolution of the GPR results. There is a tradeoff between these three parameters, such that a higher antenna bandwidth or frequency allows for a higher resolution, with the limitation being a lower penetration depth. The spatial resolution can be described as the system's ability to differentiate between the different elements and materials beneath the surface. Depending on the application of the GPR and purpose for testing, a small penetration depth may be acceptable,

such as when locating rebar. Figure 18 shows a schematic of this relationship between antenna frequency, resolution, and penetration depth.

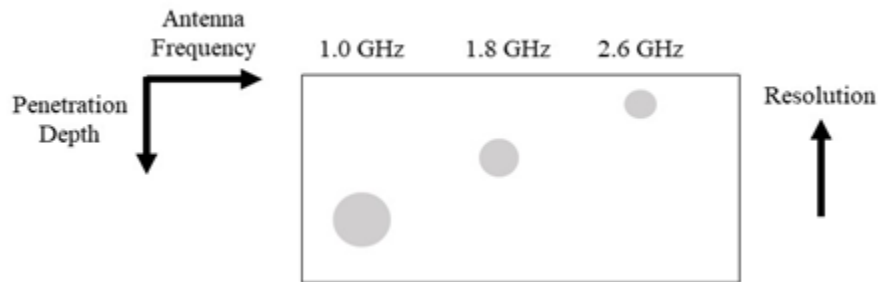


Figure 18. Schematic. Relationship between GPR antenna frequency, resolution, and penetration depth when detecting subsurface objects.

A GPR system with 1.0 GHz has the capability to detect a pavement layer with a minimum thickness of 40 mm (1.5 inch) to an accuracy of ± 5.0 mm (± 0.2 inch). Conversely, increasing the antenna frequency to 2.0 GHz only allows for the detection of a minimum layer thickness < 25 mm (1.0 inch). However, because this will produce better resolution, this can be determined with a better accuracy of ± 2.5 mm (± 0.1 inch). A drawing of this situation is presented in figure 19.

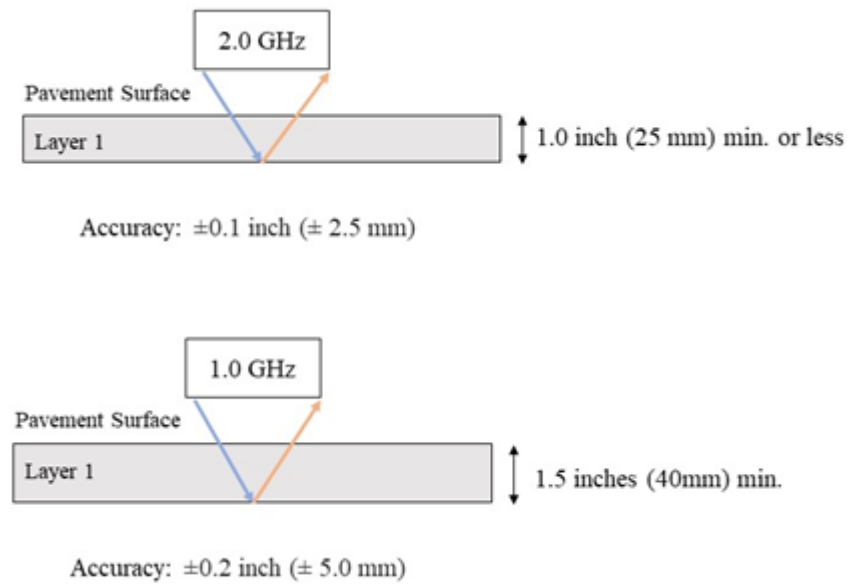


Figure 19. Drawings. Representation of Section 4.1.1.1, showing the comparison of different suggested antenna frequencies and determining layer thickness.

Similar to choosing the antenna frequency, there are advantages and limitations for both air-launched and ground-coupled antennas. Due to having direct contact with the surface, ground-coupled antenna systems are recognized to produce more reliable results. This is because the GPR can transmit more energy at greater depths compared to having the antennas off the testing surface, which lowers spatial resolution [26]. However, there are some cases in which air-coupled antenna systems are more desirable. GPR equipment with air-coupled antennas are generally attached to a vehicle or cart as mentioned in Sections 4.1 and 4.1.1. This testing arrangement allows for quicker surveying time, but the penetration depth is reduced due to reflection losses between the layers. However, for pavement evaluations, air-coupled systems have shown to be sufficient. Figure 20 shows the basic working principle of the ground-coupled and air-coupled GPR systems, where “T” represents the transmitting antenna, and “R” is the receiving antenna. The arrows are the waves that occur during scanning. To the right is an

idealized GPR trace of the signals for the air-coupled system in terms of how the peaks should occur when a new material is encountered.

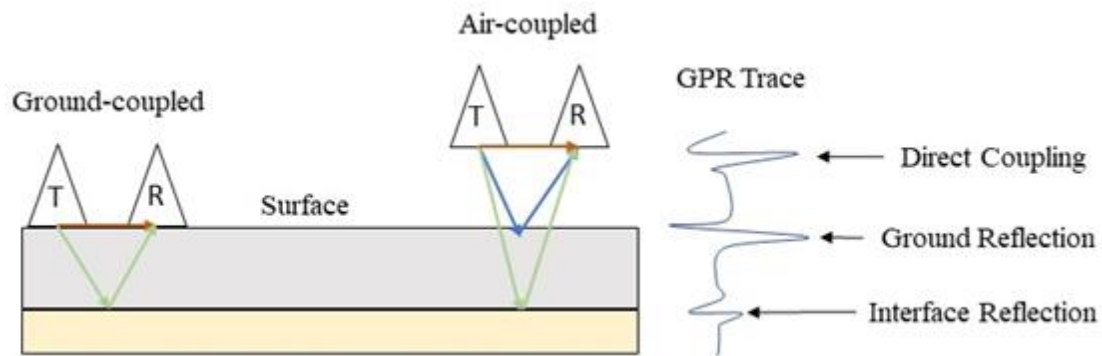


Figure 20. Diagram. Ground-coupled and air-coupled antenna systems of GPR.

Control Unit—Consisting of a transmitter, receiver, and timing control electronics, the control unit transmits and receives low-power broadband radio frequency (RF) signals through the antenna. The RF signals are then converted into a signal suitable for display and resulting interpretation. Control electronics include: DMI with an accuracy of 6190 mm/km (61 ft/mi) and a resolution of 305 mm (12 inch) or better; an optional global positioning system (GPS) with an instantaneous positioning accuracy of 1 m (3 ft) or better; and a personal computer (PC) suitable for data acquisition, display, and storage. Although the standard provides a figure for the schematic drawing of the equipment configuration, an updated version has been produced to provide more details with images. This is shown in figure 21.

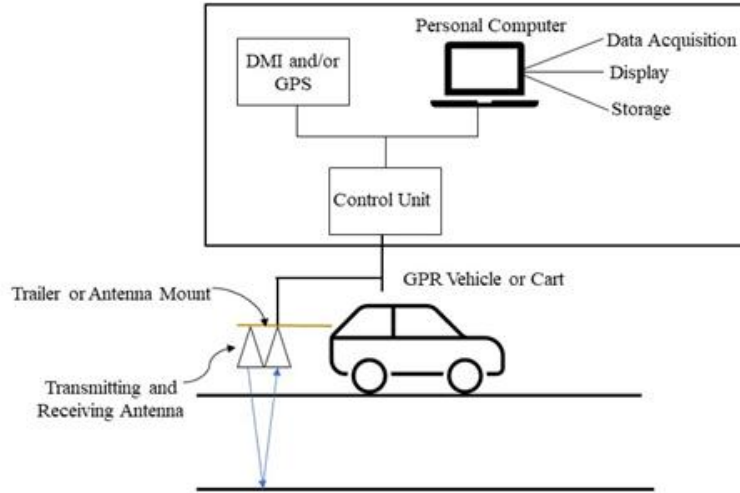


Figure 21. Diagram. Typical equipment configuration for GPR using a vehicle or cart. Air-coupled antenna system is shown.

Summary of Test Method

Layer thickness can be determined using equation 13 if the velocity and the TWTT for the radar wave to travel through a given layer are known.

Equation 13. Layer thickness.

$$T = v \times \frac{\Delta t}{2}$$

where,

T = layer thickness,

v = velocity of the radar wave through a given material, and

Δt = TWTT through layer.

The GPR system measures TWTT, so it is easily obtainable from analysis of the data. For monostatic GPR systems, the velocity of the radar wave can be estimated from the relationship given by equation 14.

Equation 14. Velocity of the radar wave.

$$v = \frac{c}{\sqrt{\epsilon_r}}$$

where,

c = speed of light in air, 300 mm/ns (11.8 inch/ns), and

ϵ_r = relative dielectric constant of layer.

Substituting equation 14 into equation 13 results in the following equation for layer thickness.

Note that equation 15 is necessarily different for bistatic antennas to accommodate for the separation distance between the transmit and receive antennas.

Equation 15. Layer thickness to accommodate for the separation distance between the transmit and receive antennas.

$$T = \frac{\Delta t \times c}{2 \sqrt{\epsilon_r}}$$

Determination of TWTT—TWTT is easily obtained by analyzing data from the GPR system.

Determination of Velocity—The velocity of the radar wave can be estimated using the following relationship for monostatic GPR systems.

Equation 16. Velocity of the radar wave for monostatic GPR systems.

$$v = \frac{c}{\sqrt{\epsilon_r}}$$

where,

c = speed of light in air, 300 mm/ns (11.8 inch/ns), and

ϵ_r = relative dielectric constant of layer.

When equation 16 is substituted for equation 13, the following equation for layer thickness is obtained. It should be noted that equation 17 must be modified for bistatic antennas to account for the separation distance between the transmit and receive antennas.

Equation 17. Layer thickness for bistatic antennas.

$$T = \frac{\Delta t \times c}{2 \sqrt{\epsilon_r}}$$

Monostatic—This term has two meanings: (1) a survey method that utilizes a single antenna acting as both the transmitter and receiver of EM waves and (2) two antennas, one transmitting and one receiving, that are separated by a small distance relative to the depth of interest that are sometimes referred to as operating in “monostatic mode.”

Bistatic—This survey method utilizes two antennas; one antenna radiates the electromagnetic waves, and the other antenna receives the reflected waves.

Relative Dielectric Constants of Typical Pavement Materials

Measurements Performed by a GPR System

An antenna is used for both sending and receiving EM signals in the GPR system. The antenna picks up the reflected and refracted EM wave as it travels through the pavement layers. The GPR system logs the amplitude and TWTT of the received signal.

Determination of the Relative Dielectric Constant or the Radar Wave Velocity of a Layer

Metal Plate Calibration—Place the antenna at operating height over a large metal plate to obtain GPR data. Use the amplitude of the metal plate reflection to calculate the pavement dielectric constant. This method is only applicable to air-coupled GPR antennas.

Ground Truth Core—Extract a pavement core at a fixed point for which GPR data are already available. Determine the core thickness and TWTT of the radar reflection from the pavement bottom, and calculate the radar wave velocity. This method assumes that the velocity is uniform across the test area.

Common Midpoint (CMP) Method—Move two ground-coupled antennas apart; one antenna will be transmitting EM waves, and the other will be receiving reflected waves. Calculate the dielectric constant of the pavement based on the change in TWTT of the reflection from pavement bottom versus separation distance between the two antennas.

This procedure can be done with either an air-coupled or ground-coupled antenna system.

However, this method involves destructive testing for validation of results. A related study by Hasan and Yazdani evaluated the applicability of estimating the dielectric constant with the ground truth core method on a concrete bridge deck as shown in figure 22. Although it is not an asphalt pavement surface, the methodology is similar. Because this specific study was done on a concrete bridge deck, the thickness in this situation was the cover depth of the rebar. Utilizing a ground-coupled antenna system, a bridge deck was surveyed and then cores were drilled to find the actual cover depth. Knowing the TWTT to the rebar, the depth to the rebar, and the velocity, the dielectric can be calculated using equation 13 and equation 14.

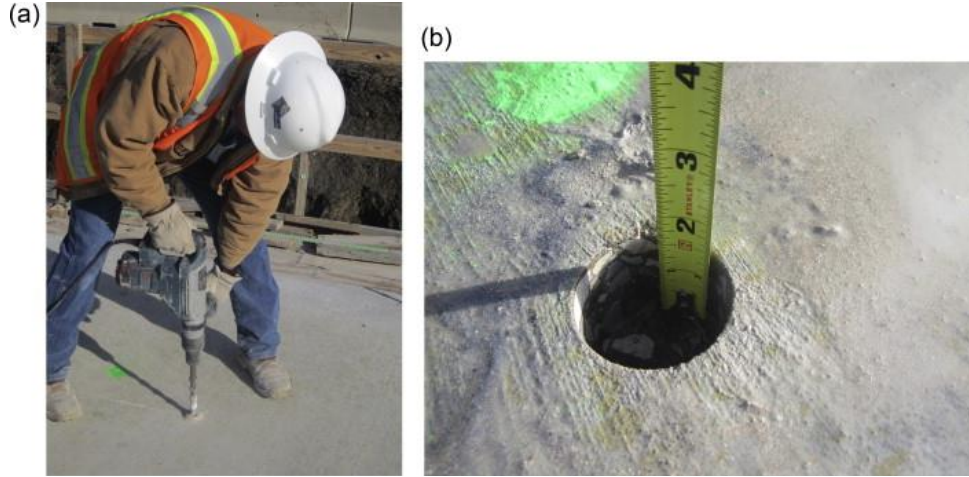


Figure 22. Photos. Hasan and Yazdani study: (a) drilling of bridge deck and (b) measuring actual cover depth after coring [7].

The CMP method describes an increase in the offset between the transmitting and receiving antenna. As a result of this, the signals form to make a stacked profile as shown in figure 23. A study carried out by Liu et al. [28] describes using a GPR setup with an air-coupled antenna system for characterizing asphalt pavement, such as determining the pavement dielectric permittivity and layer thickness.

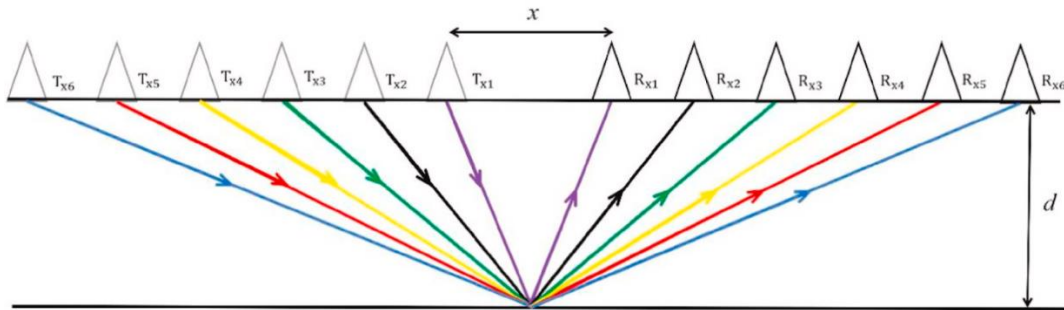


Figure 23. Diagram. CMP method of GPR measurement of a single subsurface layer [27][28].

In this method, the TWTT (t) can be calculated using equation 18.

Equation 18. TWTT.

$$t(x) = \frac{2\sqrt{\left(\frac{x}{2}\right)^2 + d^2}}{v}$$

where the antenna offset is denoted by x , and d is the thickness of the pavement layer. The velocity is found using equation 14, as mentioned previously.

Relative Dielectric Constants of Typical Pavement Materials

The ability to detect a layer depends on the contrast between the dielectric constant of that layer and the layer beneath. Table 13 shows the relative dielectric constants and radar wave velocity through various materials.

Table 13. Relative dielectric constants and radar wave velocity through the materials.

Material	Relative Dielectric Constants	Radar Velocity (m/ns)	Radar Velocity (inch/ns)
Air	1	0.30	11.8
Water	81	0.03	1.3
Asphalt	2–4	0.15–0.21	5.9–8.4
Clay	2–10	0.05–0.21	1.9–8.4
Concrete	4–10	0.010–0.15	3.7–5.9
Granite	5–8	0.11–0.15	4.4–5.9
Limestone	4–8	0.10–0.15	4.2–5.9
Sand	4–6	0.12–0.15	4.8–5.9
Sandstone	2–3	0.17–0.21	6.8–8.4
Sandy Soil	4–6	0.12–0.15	4.8–5.9
Clayey Soil	4–6	0.12–0.15	4.8–5.9
Gravel	4–8	0.10–0.15	4.2–5.9

Determination of Interferences—Radar returns can be obstructed by large objects like vehicles.

The optimal distance to maintain from the zone of influence from large objects can be calculated using equation 19.

Equation 19. Optimal distance to maintain from the zone of influence from large objects.

$$d = \frac{t}{2 \times k}$$

where:

d = the zone of influence,

k = multiplication constant, 3.28 for d (in meters) or 1 for d (in feet); and

t = time in nanoseconds (ns) of the measured data.

At some depth, the reflections at the layer interfaces cannot be detected by the GPR. This maximum penetration depth is a complex function of GPR system parameters such as transmitted power, receiver sensitivity, center frequency, and bandwidth of the GPR system and signal processing, as well as the EM properties of the pavement materials and environmental factors such as moisture content.

Interferences

Determinations made with GPR are adversely affected by surface and subsurface water. Standing water on the surface of the pavement decreases the amount of energy that penetrates the pavement. This effect is difficult to measure and may vary dramatically over a short time interval due to variations in the thickness of the water layer caused by runoff or evaporation. However, in general, testing shall not be conducted in the presence of standing water.

As shown in table 13, the relative dielectric constant of water is 81, which is significantly higher than the values for air and other materials. Because the velocity of the radar wave is dependent on the material's dielectric constant, more water or moisture in a material will slow down the velocity of this wave (see equation 14). This is because more energy will be absorbed in the presence of a saturated or wet material.

The apparatus is subject to interference from other sources of EM radiation. Interference from nearby high-power transmitters manifests itself as large, high-frequency variations in the radar

return across the entire measurement depth. Other sources of intermittent interference may include mobile phones and radios. Testing shall not be conducted in the presence of observed interference.

As mentioned before, some objects may interfere with GPR signals, which can affect the results. Because of these interferences, signal processing steps may be necessary for an understanding of the data. Post-processing techniques can reduce the noise sources from other EM devices.

Ciampoli et al. described some of these methods, specifically for application of GPR data obtained from surveying flexible pavements [28][29]. One of these methods is background noise removal, which is applied to remove the nearby noises for an improvement on the signals.

Another application is referred to as antenna ringing removal and is accomplished by finding the average GPR trace to subtract from the individual GPR traces. Additionally, signal gain can be applied to the raw data for an improvement of the signal amplitudes. Figure 24 shows a general schematic of the procedure for processing the GPR data. This figure displays the ones previously mentioned in no particular order. Post-processing techniques are not limited to only these. Some newer GPR systems may offer these image and signal processing techniques through the software, making the interpretation of results easier for the user.

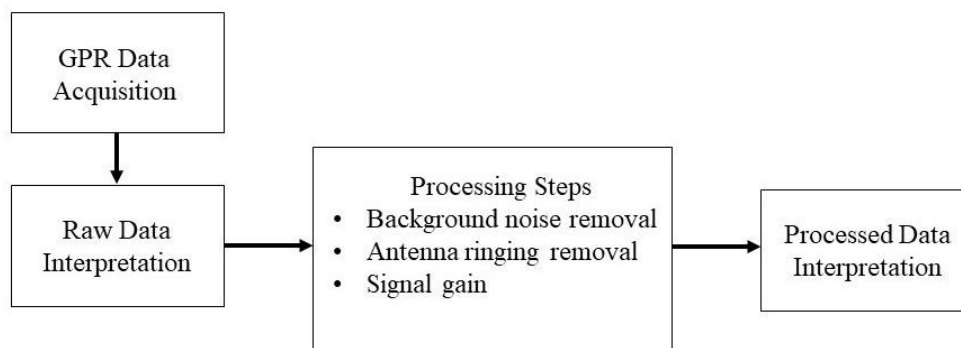


Figure 24. Flowchart. General GPR data processing.

Processing Techniques with Proceq GP App

For the current GPR equipment utilized, GP8000, the compatible application (app) available is the Proceq GPR Live by Screening Eagle Technologies. Through this software, some processing techniques can be applied. These consist of the following:

- Linear gain—gains/amplitudes are adjusted from the top down.
- Time gain—gains/amplitudes are adjusted from bottom down.
- Background removal depth—removes horizontal banding.
- Hyperbolic fitting—the user fits the hyperbola over a buried object (in the form of hyperbolic shape) for finding the dielectric constant of a material.

Large objects, such as vehicles, have the potential to interfere with the radar return. A conservative, equipment-independent approach to minimize the effects of large objects is to maintain these objects at a distance outside the zone of influence as calculated using equation 19.

At the time of this report, there is no current research or work found related to the zone of influence, specifically with GPR technology. Therefore, a clear understanding of Section 9.3 has not been reached in connection as to how vehicles may interfere with the radar return. Because there are many studies using GPR attached to vehicles with no mention of the zone of influence, this brings to question how applicable or necessary it is to calculate the zone of influence.

ASSESSMENT OF ASTM D6432 STANDARD

It is critical to understand how the antenna of a GPR system collects data. A single antenna can function as both a transmitter and a receiver, or they can be physically separated. Bistatic systems have dedicated antennas for both the transmitter and receiver, whereas monostatic (or

transceiver) systems use a single antenna for both operations (figure 25). The source signal in both systems is an EM wave.

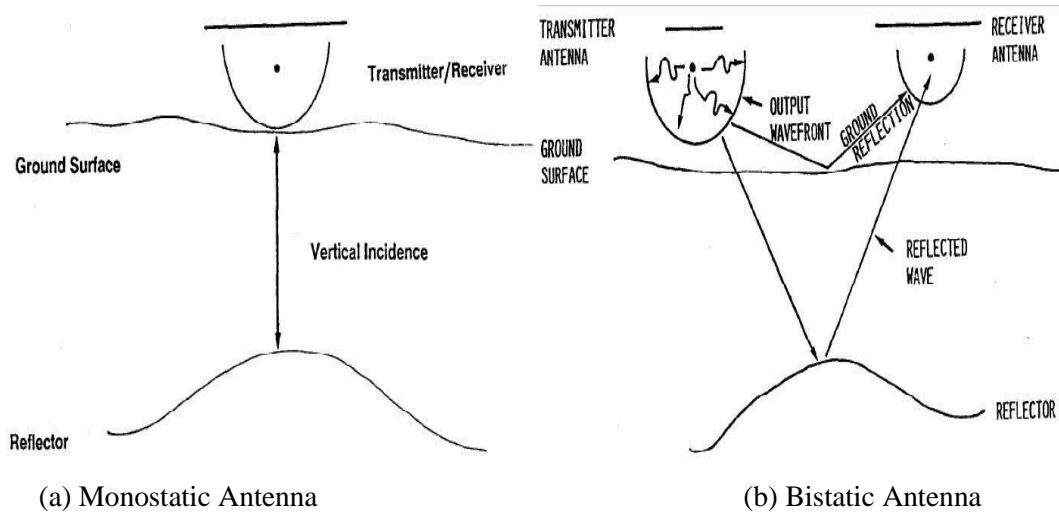


Figure 25. Schematic diagram. GPR system with (a) monostatic and (b) bistatic antenna.

The radar control unit is the next critical component of the GPR system. The majority of commercial GPR systems employ an impulse waveform in which the radar transmits a very narrow pulse (less than a few nanoseconds) with a high peak power at a constant pulse repetition frequency (PRF). The received signal is routed through the nodes of a broadband antenna, and the time-delayed received waveform is saved, typically integrated, and displayed. The stepped-frequency continuous-wave (SFCW) waveform, on the other hand, is implemented by transmitting a few single-frequency tones separated in frequency by ΔF hertz. The amplitude and phase of the received data are sampled and recorded at each frequency. The data are then transformed into the spatial domain using the inverse discrete Fourier transform (IDFT) in most implementations. This generates a synthesized pulse for information extraction and inversion [29][30].

The EM pulse propagates away from the transmitter until it comes into contact with a body with a different electrical impedance than the host material. If a monostatic antenna is used (or the transmitter and receiver are close to each other), and the transmitted pulse does not collide with a buried body, only the transmitted pulse is detected. However, if the transmitted pulse is reflected by a body, both the transmitted and reflected pulses are recorded. The reflected pulse is delayed by a time (t_d , in seconds) that is proportional to the speed of the EM pulse (velocity = v , in meters per second) through the host material and the depth of the body (z in meters), according to equation 20.

Equation 20. Reflected pulse time delay.

$$t_d = zv$$

The time it takes for the incident pulse and the reflected pulse to travel through the host rock is added together to determine the TWTT for the reflected wave. A scan is the representation of a single transmitted pulse and the reflections it causes, plotted as a function of time and amplitude.

The time on GPR records is recorded in nanoseconds (where $1 \text{ ns} = 10^{-9} \text{ s}$), and the typical length of a scan (total recording time) is between 0 and 20 ns. A high-frequency antenna, in general, has higher resolution and lower depth penetration (higher attenuation) than a low-frequency antenna.

Significance and Use

Concepts—This guide summarizes the equipment, field procedures, and data processing methods used to interpret geologic conditions, and to identify and provide locations of geologic anomalies and man-made objects with the GPR method. The GPR uses high-frequency EM waves (from 10 to 3000 MHz) to acquire subsurface information. Energy is propagated downward into the

ground from a transmitting antenna and is reflected back to a receiving antenna from subsurface boundaries between media possessing different EM properties. The reflected signals are recorded to produce a scan or trace of radar data. Typically, scans obtained as the antenna(s) move over the ground surface are placed side by side to produce a radar profile.

The vertical scale of the radar profile is in units of TWTT, the time it takes for an EM wave to travel down to a reflector and back to the surface. The travel time may be converted to depth by relating it to on-site measurements or assumptions about the velocity of the radar waves in the subsurface materials.

Vertical variations in propagation velocity due to changing EM properties of the subsurface can make it difficult to apply a linear time scale to the radar profile [30][31].

Parameter Being Measured and Representative Values

TWTT and Velocity—A GPR trace is the record of the amplitude of EM energy that has been reflected from interfaces between materials possessing different EM properties and recorded as a function of TWTT. To convert two-way times to depths, it is necessary to estimate or determine the propagation velocity of the EM pulses or waves. The relative permittivity of the material (ϵ_r) through which the EM pulse or wave propagates mostly determines the propagation velocity of the EM wave. The propagation velocity through the material is approximated using the relationship in equation 21 [31][32].

Equation 21. Propagation velocity.

$$V_m = c / \sqrt{\epsilon_r}$$

where,

c = propagation velocity in free space (3.00×10^8 m/s),

V_m = propagation velocity through the material, and

ϵ_r = relative permittivity.

It is assumed that the magnetic permeability is that of free space and the loss tangent is much less than 1.

Although GPR surveys can be carried out in a variety of ways, the method typically used in assessing the performance of asphalt overlay involves dragging the transmitter and receiver antennas together across the ground, a technique known as fixed offset reflection mode. The transmitter sends out pulses at regular intervals along a transect, which the receiver detects. A computer (or iPad) collects data and displays it as a 2D profile.

The effectiveness of GPR is determined by the soil conditions in the area. GPR works best in a homogeneous soil matrix with a high electrical resistance to locate buried objects. In a heterogeneous environment with high electrical conductivity, GPR is least effective. A heterogeneous environment contributes to signal scattering, which can lead to insufficient penetration depth and “noisy” reflection (poor SNR). Due to conductive losses, a conductive environment can severely limit the depth of penetration. Conductive loss occurs when an EM wave generates a conductive current in the soil medium, causing signal attenuation.

The GPR works by sending high-frequency EM waves from a transmitter antenna. Some of these waves are reflected back to the surface as they pass through changes in the dielectric permittivity of the matrix and are detected by a receiver antenna. On a portable computer, the amplitude and TWTT of these reflections are recorded. These data are then used to build a 2D plot of horizontal distance versus travel time. The information gathered in the field is saved on a portable computer

for later analysis. A more complete and technical discussion of the method can be found elsewhere [32].

Zhao and Al-Qadi demonstrated simulation in their research using zeroth-, first-, and second-order Tikhonov (TV) regularization, with each case (noise level and layer thickness) repeated 30 times to ensure statistical correctness [33][34]. Because of the longer computation time, only eight repetitions were performed for TV regularization. In applications such as estimating asphalt layer thickness, the accurate determination of the impulse distance is more important than the impulse amplitude; thus, the error in estimated impulse distance for each case was calculated and compared to the true layer thickness in this study.

Figure 26 depicts one simulation example with noise: The first plot shows the incident signal; the second shows the assumed impulse response with a distance of 0.61 ns; the third shows the simulated clean signal; and the fourth shows the noisy data with an SNR of 20 dB. Without regularization, it is impossible to resolve the two pulses in either clean or noisy signals. Because the sign of the impulses is unimportant and the goal is to increase the resolution of the GPR signal, the sign of the impulse response and regularization result were inverted in future plots for better visualization.

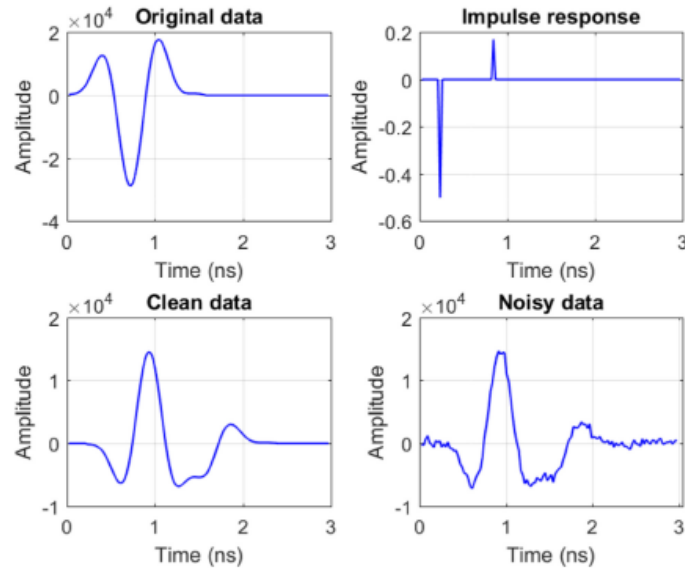


Figure 26. Plots. One example of simulation: incident signal (top left), 0.61 ns impulse response (top right), simulated signal (bottom left), and noisy signal (bottom right).

Table 14 lists the relative permittivity (ϵ_r) and radar propagation velocities for various materials. Relative permittivity values range from 1 for air to 81 for fresh water. For unsaturated earth materials, ϵ_r ranges from 3 to 15. Note that a small change in the water content of earth materials results in a significant change in the relative permittivity. For water-saturated earth material, ϵ_r can range from 8 to 30. These values are representative, but may vary considerably with temperature, frequency, density, water content, salinity, and other conditions.

Table 14. Approximate EM properties of various materials.

Material ^A	Relative Permittivity, K	Wave Velocities, m/ns	Conductivity, mS/m
Air	1	0.3	0
Fresh water (f,t)	81	0.033	0.10 - 30
Sea water (f,t,s)	70	0.033	400
Sand (dry) (d)	4-6	0.15-0.12	0.0001 - 1
Sand (saturated) (d,w,f)	25	0.055	0.1 - 1
Silt (saturated) (d,w,f)	10	0.095	1 - 10
Clay (saturated) (d,w,f)	8-12	0.106-0.087	100 - 1000
Dry sandy coastal land (d)	10	0.095	2
Fresh water ice (f,t)	4	0.15	0.1 - 10
Permafrost (f,t,p)	4-8	0.15-0.106	0.01 - 10
Granite (dry)	5	0.134	0.00001
Limestone (dry)	7-9	0.113-0.1	0.000001
Dolomite	6-8	0.122-0.106	
Quartz	4	0.15	
Coal (d,w,f, ash content)	4-5	0.15-0.134	
Concrete (w,f, age)	5-10	0.134-0.095	
Asphalt	3-5	0.173-0.134	
Sea ice (s,f,t)	4-12	0.15-0.087	
PVC, epoxy, polyesters vinyls, rubber (f,t)	3	0.173	

^A

d = function of density,
w = function of porosity and water content,
f = function of frequency,
t = function of temperature
s = function of salinity, and
p = function of pressure.

If the relative permittivity is unknown, as is normally the case, it may be necessary to estimate velocity or use a reflector of known depth to calculate the velocity. The propagation velocity, V_m , is calculated from the relationship as in equation 22.

Equation 22. Propagation velocity when the relative permittivity is unknown.

$$V_m = 2D/t$$

where,

D = measured depth to reflecting interface and

t = TWTT of an EM wave.

Methods for measuring velocity in the field are found in Section 6.7.3. Note that measured velocities may only be valid at the location where they are measured under specific soil conditions. If there is lateral variability in soil and rock composition and moisture content, velocity may need to be determined at several locations.

Attenuation—The depth of penetration is determined primarily by the attenuation of the radar signal due to the conversion of EM energy to thermal energy through electrical conduction, dielectric relaxation, or magnetic relaxation losses. Conductivity is primarily governed by the water content of the material and the concentration of free ions in solution (salinity). Attenuation also occurs due to scattering of the EM energy in unwanted directions by inhomogeneities in the subsurface. If the scale of inhomogeneity is comparable to the wavelength of EM energy, scattering may be significant [34]. Other factors that affect attenuation include soil type, temperature [35], and clay mineralogy [36]. Environments not conducive to using the radar method include high-conductivity soils, sediments saturated with salt water or highly conductive fluids, and metal.

It is important to calibrate the effect of concrete cover of actual rebars on the GPR attenuation in order to accurately estimate $\delta_{\text{cover_conductive}}$. Figure 27a shows the variation of δ_{cover} ($\delta_{\text{cover_depth}} + \delta_{\text{cover_conductive}}$) with respect to TWTT of GPR signals reflected through concrete cover of the top rebars. To estimate the reference attenuation curve that represents sound concrete, the following assumptions are made: at least some parts of the deck areas in the test bridge remain in sound condition, and the attenuation of GPR signals derived from concrete cover in sound condition is linearly proportional to TWTT [37].

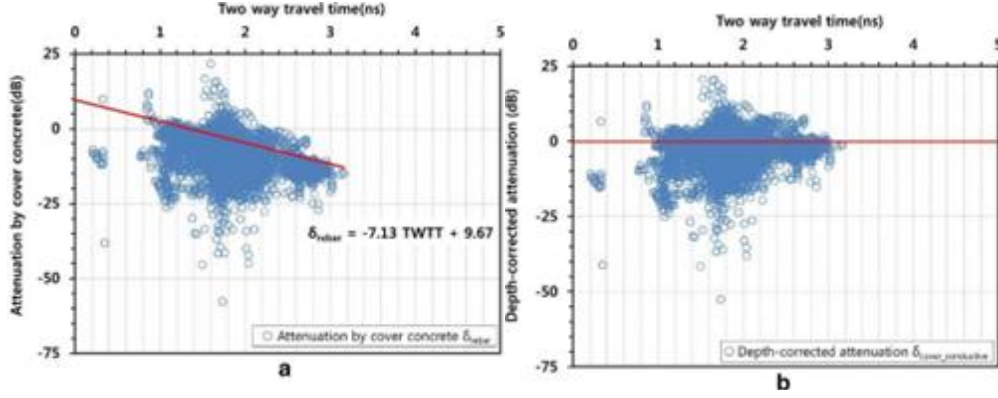


Figure 27. Plots. Variation of attenuation of GPR reflected signal from rebars with TWTT: before and after the depth-correction procedure.

Subsequently, figure 27b shows the depth-corrected attenuation by subtracting the contribution of the geometric damping. As for the overlay thickness, the errors between the predicted and measured thickness are within the range of 1–18 percent (average of 7.8 percent), whereas the range of error values for cover thickness are between 3 and 27 percent (average of 12.5 percent). The errors are attributed to the experimental variations of the EM properties of actual materials (e.g., asphalt overlay, waterproof layer, concrete) that were not considered in the GPR field survey. However, the errors are still within the acceptable range of values in the field survey [37].

Figure 28 shows the variation of the depth-corrected attenuation, $\delta_{\text{cover_conductive}}$, from the GPR survey with the deteriorated depth of concrete bridge deck measured from core samples ($\delta_{\text{conc_damage}}$). An approximate equation representing the relationship between $\delta_{\text{cover_conductive}}$ and $\delta_{\text{conc_damage}}$ is established by a linear regression analysis as in equation 23.

Equation 23. Depth-corrected attenuation.

$$\delta_{\text{cover_conductive}} = 0.076\delta_{\text{conc_damage}} + 4.71$$

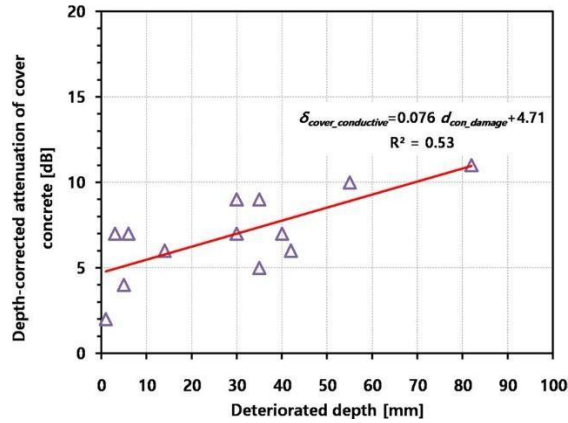


Figure 28. Graph. Relationship between depth-corrected attenuation measured by air-coupled GPR system.

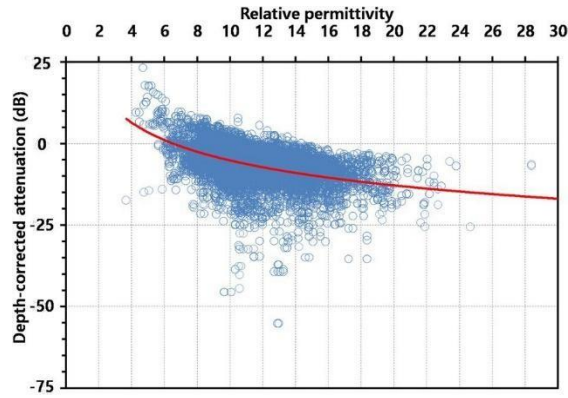


Figure 29. Plot. Relationship between depth-corrected attenuation of concrete cover and relative permittivity of concrete on the top surface of the bridge decks.

Figure 29 illustrates the relationship of the depth-corrected attenuation of concrete cover against the relative permittivity of concrete on the top surface of the bridge decks. Overall, the depth-corrected attenuation tends to increase as the relative permittivity of concrete increases.

However, numerous data points are far from the best-fit line of the two GPR parameters, which is shown as a red solid line in figure 29. This deviation is due to the two GPR parameters that are based on different fundamental principles, physical significance, and properties.

For practical applications, the study proposes two critical values to accurately interpret the depth-corrected attenuation values from the GPR survey. The first criterion is the value of

$\delta_{\text{cover_conductive}}$, which should not be <5 dB and could determine the presence of concrete deterioration on the top of concrete. The second criterion is $\delta_{\text{cover_conductive}}$, where the value should not be <11 dB in order to determine the degree of the corrosive environment around the rebars in concrete. However, the criteria in practice should be carefully utilized because the depth-corrected attenuation of GPR signals could be affected by many factors, such as types of GPR equipment, water content of bridges, severity and types of deterioration in concrete, thickness and condition of asphalt overlay, and procedure of the depth correction. Therefore, it is difficult to generalize the relationship between $\delta_{\text{cover_conductive}}$ and $\delta_{\text{conc_damage}}$. However, the experimental results are useful to better understand the relationship between $\delta_{\text{cover_conductive}}$ and $\delta_{\text{conc_damage}}$ through the GPR field survey. This, in turn, could further improve the reliability of GPR technologies for the condition assessment of actual concrete bridge with asphalt overlay on expressways. Table 15 shows five categories of deterioration based on GPR interpretation for condition assessment of concrete bridge decks with asphalt overlays.

Table 15. Dual criteria–based GPR interpretation for condition assessment of concrete bridge decks with asphalt overlays in Korea expressway networks.

Category	GPR		Assessment and analysis			
	Relative permittivity	Depth-corrected attenuation (dB)	Waterproof function	Deteriorated environment	Concrete deterioration	Rebar corrosion
Good	$\epsilon < 11$	$\delta < 5$	Good	×	×	×
Fair	$\epsilon \geq 11$	$\delta < 5$	Poor	×	×	×
Poor	$\epsilon \geq 11$	$9 > \delta \geq 5$	Good	○	○	×
Serious	$\epsilon \geq 11$	$\delta \geq 9$	Poor	○	○	○
Watch	$\epsilon < 11$	$\delta \geq 5$	Good	○	○	Δ

×: low possibility of damage, Δ: unknown, ○: high possibility of damage.

Limitations and Interferences

Limitations Specific to the GPR Method

The GPR method is site-specific in its performance (depth of penetration and resolution), depending upon surface and subsurface conditions. The method is most effective in clean granular soils (i.e., SP, SP-SM) and may not be effective in soils that contains clayey fines and fine-grained soil. Radar penetration of more than 30 m has been reported in geologic settings of water-saturated sands, 300 m in granite, 2000 m in dry salt, and 5400 m in ice. More commonly, penetration is on the order of 1–10 m. Limitations are discussed in the following section.

Material Properties Contrast—Reflection coefficients quantify the amplitude of reflected and transmitted signals at boundaries between materials. Reflection coefficients depend on the angle of incidence, the polarization of the incident field, and the EM property contrast. In addition to having sufficient velocity contrast, the boundary between the two materials needs to be sharp. For instance, it is more difficult to see a water table in fine-grained materials than in coarse-grained materials because of the different relative thicknesses of the capillary fringe for the same contrast.

Attenuation—Radar signal attenuation is caused by the effect of electrical conductivity, dielectric and magnetic relaxation, scattering, and geometric spreading losses.

- *Electrical Conductivity Losses*—Electrically conductive materials, such as many mineralogic clays and free ions in solution, attenuate the radar signal by converting EM energy to thermal energy.
- *Dielectric Relaxation Losses*—Radar signals can also be attenuated by dielectric relaxation losses due to the rotational polarization of the liquid water molecule and

chemical charge transfer processes on the surface of clay minerals. Attenuation due to dielectric relaxation losses arises from the conversion of EM energy to thermal energy.

- *Geometric Scattering Losses*—Scattering may be a dominant factor in signal attenuation when inhomogeneities in materials with grain sizes in the order of a radar wavelength (table 16) are present.

Table 16. Radar wavelengths (meters) for various antenna frequencies (f) and relative permittivities (ϵ_r).

ϵ_r	1	5	10	15	25	80
f						
25 MHz	12.0	5.36	3.8	3.08	2.4	1.36
50 MHz	6.0	2.68	1.88	1.56	1.2	0.68
80 MHz	3.76	1.68	1.20	0.96	0.76	0.40
100 MHz	3.0	1.36	0.96	0.76	0.6	0.32
200 MHz	1.52	0.68	0.48	0.40	0.32	0.16
300 MHz	1.0	0.44	0.32	0.24	0.20	0.12
500 MHz	0.6	0.28	0.20	0.16	0.12	0.08
900 MHz	0.32	0.16	0.12	0.08	0.08	0.04

Polarization—The type and alignment of polarization of the vector EM fields may be important in receiving responses from various scatterers. Two linear, parallel polarized, electric field antennas can maximize the response from linear scatters like pipes when the electric field (typically long axis of the dipole antenna) is aligned parallel with the pipe and towed perpendicular across the pipe. Similarly, alignment with the rebar in concrete will maximize the ability to map the rebar, but alignment perpendicular to the rebar will minimize scattering reflections from the rebar to see through or past the rebar to get the thickness of concrete. Similar arrangement may be made for overhead wires and nearby fences. Cross-polarized antennas (perpendicular to each other) minimize the response from horizontal layers.

Interferences Caused by Ambient, Geologic, and Cultural Conditions

Measurements obtained by the GPR method may contain unwanted signals (noise) caused by geologic and cultural factors.

Ambient and Geologic Sources of Noise—Boulders, animal burrows, tree roots, or other inhomogeneities can cause unwanted reflections or scattering of the radar waves. Lateral and vertical variations in EM properties can also be a source of noise.

Cultural Sources of Noise—Aboveground cultural sources of noise include reflections from nearby vehicles, buildings, fences, power lines, lampposts, and trees. In cases where this kind of interference is present in the data, a shielded antenna may be used to reduce the noise.

- Scrap metal at or near the surface can cause interference or ringing in the radar data. The presence of buried structures such as foundations, rebar, cables, pipes, tanks, drums, and tunnels under or near the survey line may also cause unwanted reflections (clutter).
- In some cases, EM transmissions from nearby cellular telephones, two-way radios, television, and radio and microwave transmitters may induce noise on the radar record.
- Other sources of noise can be caused by the EM coupling of the antenna with the earth and decoupling of the antenna to the ground due to rough terrain, heavy vegetation, water on the ground surface, or other changes in surface conditions.

Summary—All possible sources of noise present during a survey should be noted so that their effects can be considered when processing and interpreting the data.

ASSESSMENT OF AASHTO-PP 98 STANDARD

Standard Practice for Asphalt Surface Dielectric Profiling System Using Ground Penetrating Radar. American Association of State Highway and Transportation Officials (AASHTO)

PP 98-20 outlines the utilization of a dielectric profiling system (DPS) with GPR. Included in the standard are both the software and hardware requirements for the system. Additionally, there are brief descriptions of the different calibration techniques that can be used. The DPS is only applicable for air-coupled antenna systems. The surface dielectric constant is calculated using equation 24 (S2-R06C-RR-1).

Equation 24. Surface dielectric constant.

$$\epsilon_r = \left(\frac{1 + \frac{A_o}{A_i}}{1 + \frac{A_o}{A_i}} \right)^2$$

where,

ϵ_r = dielectric constant,

A_o = amplitude of the reflection at the air/asphalt interface, and

A_i = initial antenna amplitude (may be measured with a metal plate calibration).

Dielectric Profile—The surface dielectric readings and associated stationing, offset, Global Navigation Satellite System (GNSS) coordinates, and time stamps.

DPS—The specific arrangement of the GPR equipment used to measure the dielectric constant including the GPR antennas, radar control unit, and suitable data storage, calculation, and display devices (figure 30).

Heat Map Plot—A graphic display of data using color scales. These plots may display raw values or employ varying degrees of smoothing (adapted from PP 81).

Hardware Requirements

Dielectric Profiler System Overview—The DPS consists of the following components: vehicle or cart, antenna boom, DMI, and GPS (strongly recommended); single or multi-channel air-coupled GPR system (see ASTM D4748): radar antenna(s) and control unit, computer, or tablet with software; and metal plate and validation block.

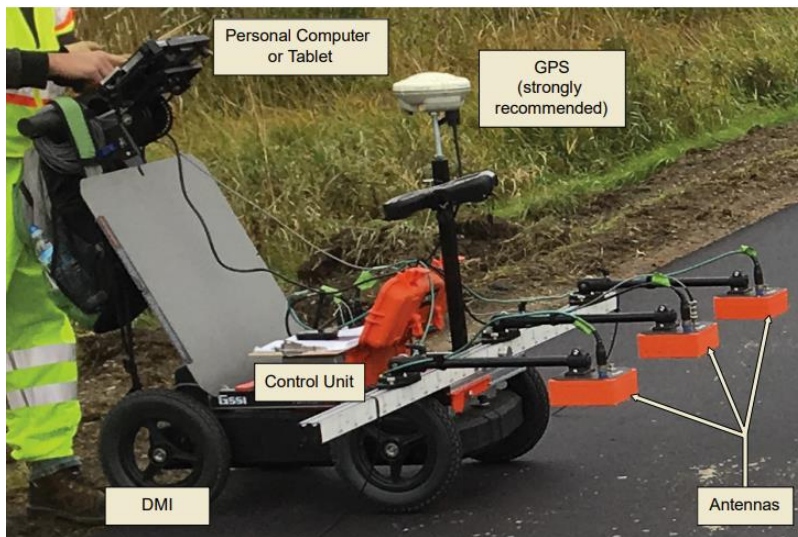


Figure 30. Photo. Basic equipment for DPS.

The DPS shall measure the dielectric constant of the asphalt surface based on the GPR surface reflection. The system shall be capable of recording these data at both fixed distance intervals (distance mode) and at fixed time intervals (time mode). A vehicle or cart shall be provided to carry the GPR system, computer, metal plate, and antenna boom, and be equipped with a DMI and GPS receiver.

Antenna Boom—Nonmetallic boom to maintain the antenna(s) at a fixed vertical height and at least 18 inches away from any large metal body, such as the vehicle frame. Proximity to smaller metallic components on a hand pushcart are permissible as long as the system meets performance

metrics. Processing algorithms should account for vertical movement from the vehicle suspension. When vehicle-mounted, the system shall be structurally capable of traveling up to 50 mph with tolerable antenna movement. The position of the antenna(s) should be adjustable to allow for collection at agency-specific lateral positions within the pavement lane.

DMI—The vehicle or cart should be instrumented with a DMI with a minimum operational tolerance of 1 ft/mi.

GPS—The vehicle or cart should be instrumented with a GPS with a minimum operational tolerance of ± 15 ft and allow for input of an external GPS string.

Air-Coupled GPR

Single- or multi-channel air-coupled GPR system with an operational frequency of between 1 and 3 GHz shall be used. All antennas shall have the same frequency.

Operating Requirements—The GPR system shall pass the operating requirements in table 17.

These are based on the metal plate reflection tests recommended by the Texas A&M Transportation Institute with the Federal Highway Administration (FHWA/TX-92/1233-1) for general-purpose GPR. Each of these measurements shall be determined at the factory prior to delivery of the equipment. Subsequent operating requirement testing will be conducted by the user to meet table 17 requirements.

Table 17. Operating requirements summary table with required limits.

Measure Description	Required Limit (Max)
Short Term Dielectric Stability (STDS)	0.06
Drift Dielectric Stability (DDS)	0.08
Long Term Dielectric Stability (LTDS)	0.08
Inter-Antenna Dielectric Variation (IADV)	0.08
Inter-Antenna Amplitude Variation (IIDV)	5%

Short Term Dielectric Stability (STDS)—Stability of the measured dielectric constant over a short time period. In time-mode, collect 50 surface dielectric measurements over a validation block at a minimum rate of 15 scans/s. Stacking or moving average techniques may be used if the DPS has the capability of collecting data at a faster rate. Calculate the STDS using equation 25.

Equation 25. STDS.

$$STDS = eST_{max} - eST_{min}$$

where,

eST_{max} = maximum recorded dielectric over 50 scans and

eST_{min} = minimum recorded dielectric over 50 scans.

Drift Dielectric Stability (DDS)—Stability of the measured dielectric constant over a typical data collection period. In time-mode, collect dielectric measurements over a validation block for 20 min continuously at a minimum rate of 15 scans/s. Stacking or moving average techniques may be used if the DPS has the capability of collecting data at a faster rate. Calculate the LDS using equation 26.

Equation 26. DDS.

$$LDS = eL_{max} - eL_{min}$$

where,

eL_{max} = maximum recorded dielectric over 20 min time period and

eL_{min} = minimum recorded dielectric over 20 min time period.

Long Term Dielectric Stability (LTDS)—Stability of the DPS between calibrations. Collect 10 data sets where the system is completely turned off between data collection sets. For each data set, collect 5000 scans in time-mode over a validation block. Calculate the LTDS using equation 27.

Equation 27. LTDS.

$$LTDS = eLT_{max} - eLT_{min}$$

where,

eLT_{max} = maximum recorded dielectric over the 10 evaluated data sets and

eLT_{min} = minimum recorded dielectric over the 10 evaluated data sets.

Inter-Antenna Dielectric Variation (IADV)—Variation among the dielectric measurements from the different DPS antennas. Applicable to multi-channel DPS systems only. In time-mode, collect 1000 dielectric measurements with each antenna over a validation block. Calculate the mean dielectric constant of the block for each antenna. Calculate the IADV using equation 28.

Equation 28. IADV.

$$IADV = eA_{max} - eA_{min}$$

where,

eA_{max} = maximum mean dielectric among all DPS antennas and

eA_{min} = minimum mean dielectric among all DPS antennas.

Inter-Antenna Amplitude Variation (IAAV)—Variation among the amplitude measurements from the different DPS antennas when completing metal plate calibration. Applicable to multi-channel DPS systems only. Calculate the median amplitude of the metal plate reflection for each antenna. Calculate the IIDV using equation 29.

Equation 29. IAAV.

$$IIDV = \frac{aA_{max} - aA_{min}}{aA_{min} \times 100\%}$$

where,

aA_{max} = maximum median amplitude among all DPS antennas on metal plate calibration and

aA_{min} = minimum median amplitude among all DPS antennas on metal plate calibration.

Validation Block—A block of plastic insulating material shall be used for performance validation of the GPR antennas. The block shall conform to ASTM D2520 and ASTM D150. The block shall have a known dielectric value between 2 and 15. The minimum block size shall be 24 inch × 24 inch and 3.5 inches thick.

Software Requirements

Data Collection

Metadata—As a minimum, the software shall store the following metadata: Dielectric value, Project name, Road ID, Travel direction, Lift designation, Lane designation, Date-time,

Distance (ft), Station (ft), Lateral offset (ft), Longitude (°), Latitude (°), Elevation (ft), Moving average distance (ft, m) or time (s), Output interval distance (ft, m) or time (s), Date, and FileName.

Calibration—Before every data collection period, the software shall prompt the user to perform an air calibration for each antenna, as described in Section 7.1. Conduct calibration of the DMI as described in Section 7.3.

Note—It is recommended to conduct metal plate calibration as described in Section 7.2.

Dielectric—The software shall calculate the surface dielectric constant from the surface reflection using equation 24. Recording individual trace data is not necessary.

Air Void Conversion—The software should provide an empirical conversion from dielectric constant to asphalt air void content using a linear, logarithmic, or power equation.

Distance-Mode—The software shall be capable of recording dielectric data at fixed distance intervals as small as every 0.5 inch. The reported value may be the result of moving average, stacking, and/or oversampling techniques.

Time-Mode—The software shall be capable of recording dielectric data at fixed time frequency as fast as 15 measurements/s.

Signal Correction—The software shall account for potential cell tower interference. This may be done through oversampling, stacking, and/or averaging the data. The DPS should also account for any changes to the amplitude of the signals caused by changes in antenna height up to 0.5 inch or to the temperature of the hardware components expected during normal operation.

Distance—DMI and GPS measurements shall accompany each dielectric measurement.

Data Display—The DPS software shall display the data in real time. Display the current dielectric values from each antenna, with an appropriate moving average filter; typically, between 0.5 and 5 ft is reasonable.

Provide a plot of dielectric versus distance/time. The plot shall be a heat map and/or line graph (figure 31). The scale for the dielectric axis should allow the user to adjust the displayed dielectric range, typically centered close to the mean dielectric with a range of 1.5 from the minimum and maximum displayed values. Minimize changes to the scale as much as possible.

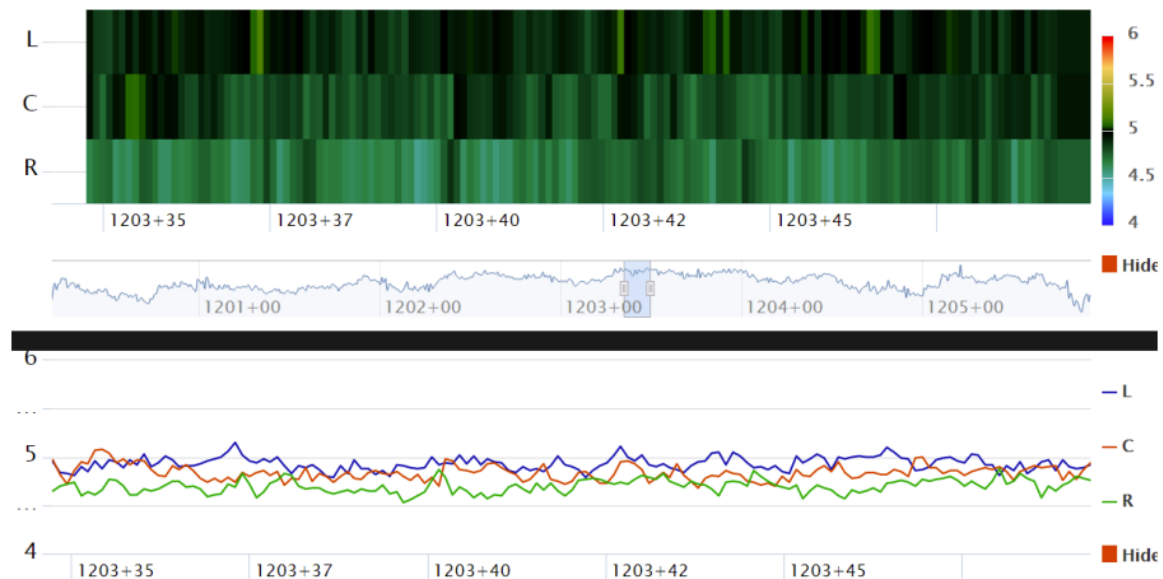


Figure 31. Graphs. Example heat map and line graph.

Data Analysis—The DPS software shall perform the following data analyses on-site: data filtering by: centerline offset, stationing, and antenna serial number; summary statistics (applied to any combination of data filtering): average dielectric, median dielectric, standard deviation of dielectric, dielectric value at n th percentile (user-specified percentage), percent below/within/above limits (user-specified dielectric range), and summary visuals (applied to any

combination of data filtering): plot of dielectric versus distance. The plot shall be a heat map and/or line graph, and histogram of the data.

Calibration

Air Calibration—Air calibration is used to subtract the direct coupling and associated noise from the antenna from the recorded signal. Follow the manufacturer recommendations for performing the air calibration. Generally, position the antennas in the air at least $1.5\times$ the height of the antenna during operation.

Metal Plate Calibration—Metal plate calibration is used to measure the antenna amplitude, A_i , in the dielectric constant calculation. Follow the manufacturer's recommendations for performing the metal calibration.

Metal Antenna Variation—If the metal plate calibration amplitude is outside of three standard deviations from the historic mean metal calibration amplitude, the equipment should be recalibrated.

DMI System—Perform DMI calibration according to the manufacturer's recommendations. Make sure the DMI is fully functional before beginning each project.

GNSS—When analyzing data in conjunction with intelligent compaction and/or IR technology, the global positioning calibration requirements from PP 80 or PP 81, or both, shall be followed.

A schematic for the DPS system setup, as mentioned in Sections 5.1 and 5.2, is shown in figure 32.

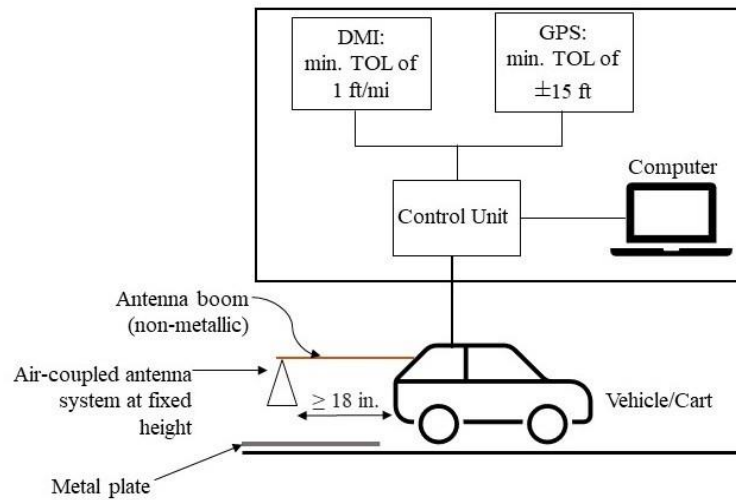


Figure 32. Diagram. Equipment setup for DPS with GPR.

The metal plate calibration technique is a common practice for air-coupled GPR systems and is also described in ASTM D4748, Section 5.4.1. Because the metal plate provides a perfect reflection, the signal is easily detectable. This technique uses the calculation described in equation 26.

Figure 33 shows a graph of dielectric values found for an asphalt pavement with utilization of a 2 GHz GPR system. The lower values for dielectric typically represent that there is a large air-void ratio of hot mix asphalt (HMA). This work presented the use of two NDT methods for evaluating the in-place density during the construction of an HMA pavement. These methods were infrared thermography and GPR.

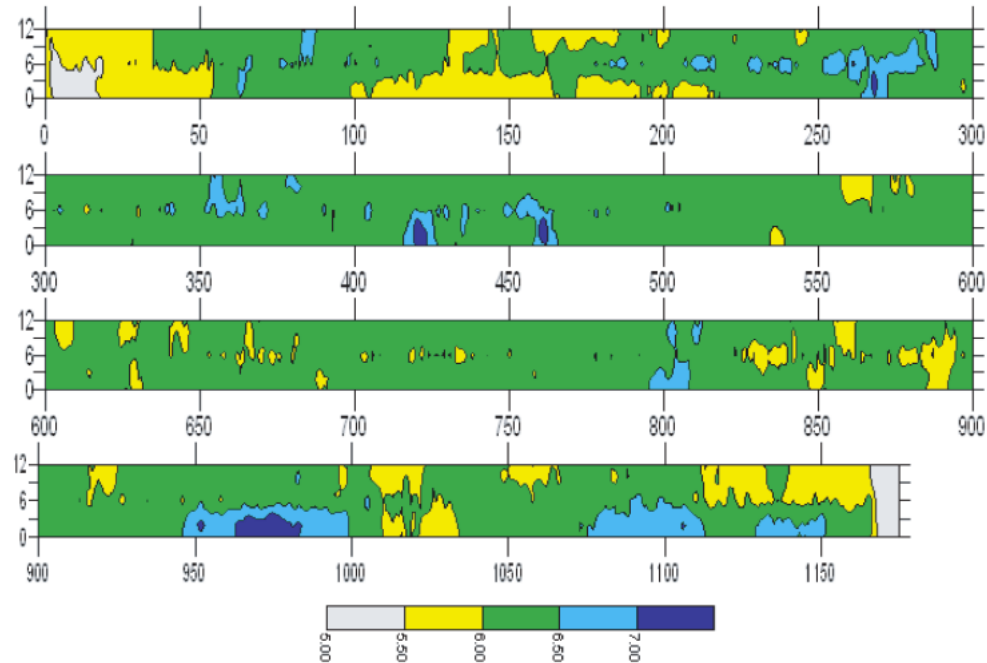


Figure 33. Graph. Dielectric values for an asphalt pavement using 2 GHz GPR [38].

Similarly, Prowell et al. created a report based on utilization of DPS and the applicability of the system to measure in-place density on asphalt pavements [39][40]. In one section labeled “Achieving Success,” the authors describe some of the current departments of transportation (DOTs) that are using DPS equipment along with their objectives. These include the following DOTs: Minnesota, Ohio, and Alaska. Minnesota DOT has been working toward developing new setups to maximize the surveying coverage. The DPS unit utilized by Ohio DOT can collect 54,000 measurements over the 1,500–2,000 tons of asphalt mix placed from taking cores. Ohio DOT takes 10 cores/day on site, but defects are easily not found at this rate. Similarly, Alaska DOT has seen that full coverage testing has the ability to locate almost all defects and has less issues compared to random spot tests.



Figure 34. Photo. Walking cart (left), gator-mounted (center), and prototype (right) robotic DPS units [40].

DPS Equipment

A commercially available DPS system is the PaveScan® RDM 2.0 by Geophysical Survey Systems Inc. (GSSI), as shown in figure 35. With a sensor frequency of 2 GHz, this instrument can assess pavement at the surface level by determining the uniformity and variations in density. This system has the capability to measure the dielectric with an accuracy of ± 0.12 . The visual output can show differences in dielectric measurements and the dielectric output of each sensor as shown in figure 36. This is similar to figure 33 in which the requirements for the DPS software are outlined by AASHTO 98.



Figure 35. Photo. PaveScan RDM 2.0 (GSSI™).

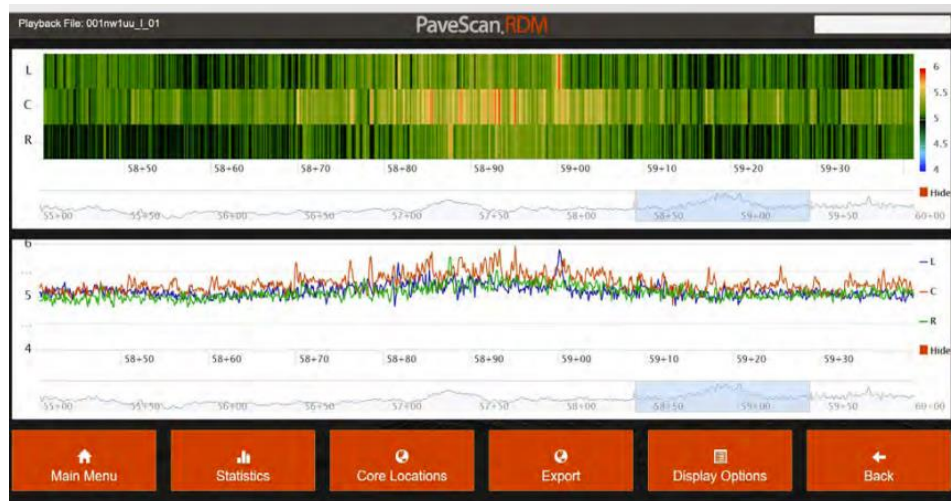


Figure 36. Screenshot. Example of visual output from PaveScan data with a color map showing anomalies in dielectric measurement (top) and a line graph of the dielectric output of each sensor (bottom) (GSSI™).

Advantages of DPS

Using a DPS GPR system makes it possible to measure the in-place density of pavement over a large area. This testing method allows for quick surveying time with dependable results. The density of HMA layers can be measured before and after compaction. However, surveying cannot be done when it is raining. Moisture on the pavement could cause changes in the dielectric values.

EVALUATE THE ADJUSTMENT, MODIFICATION, OR RECOMMENDATIONS NEEDED TO CONSIDER IN COMPARISON TO ASTM D4748 AND ASTM D6432

ASTM D4748 is a standard test method that provides guidelines for determining the thickness of bound pavement layers using short-pulse radar. When using this standard, several key considerations should be kept in mind to ensure accurate and reliable results:

- *Equipment Calibration*—Before tests, the radar equipment must be properly calibrated according to the manufacturer’s instructions. Accurate calibration is essential for precise thickness measurements.

- *Antenna Selection*—Select an appropriate radar antenna or transducer based on the expected thickness of the pavement layers and the desired resolution.
- *Surface Preparation*—Prepare the pavement surface by cleaning it of debris, loose material, and any obstructions that may interfere with the radar signal.
- *Testing Location and Pattern*—Determine the specific locations on the pavement where thickness measurements will be taken. Ensure that measurements are representative of the entire area of interest.
- *Operating Frequency*—Verify that the radar equipment operates at an appropriate frequency for the intended application. The choice of frequency depends on factors such as pavement type and thickness.
- *Waveform Characteristics*—Become familiar with the waveform characteristics of the radar equipment being used. Understand how different features in the waveforms correspond to pavement layers.
- *Measurement Accuracy*—Be aware of the measurement accuracy limitations of the radar equipment. Manufacturers typically provide information about measurement accuracy, which may vary with pavement type and conditions.
- *Data Collection and Processing*—Collect radar data at each measurement location and record it accurately. Ensure that the data collection process is systematic and consistent. Data processing may be required to analyze and interpret the radar signals.
- *Signal Interpretation*—Interpret radar signals carefully to identify interfaces between pavement layers accurately. Become familiar with the characteristics of different radar reflections, such as those from the top and bottom of each layer.

- *Layer Identification*—Identify and label each pavement layer detected by the radar. This may include surface layers (e.g., asphalt), base layers (e.g., aggregate), and subbase layers. Ensure that the layer boundaries are well defined.
- *Calibration Blocks or Standards*—If available, use calibration blocks or standards with known thicknesses to validate the accuracy of the radar measurements. This can serve as a quality control check.
- *Data Recording and Reporting*—Document all relevant information, including measurement locations, equipment settings, and radar data. Report the results accurately and clearly, including the thickness of each pavement layer.
- *Safety Precautions*—Ensure the safety of personnel and the public during testing. Implement traffic control measures and follow safety guidelines when working on roadways.
- *Quality Control and Quality Assurance*—Implement quality control and quality assurance procedures to verify the reliability and consistency of the data collection process. This may involve conducting repeat measurements or cross-checks at select locations.
- *Environmental Conditions*—Be aware of how environmental conditions, such as temperature, moisture, and surface conditions, may affect radar measurements. Take these factors into account when interpreting results.
- *Training and Expertise*—Ensure that personnel conducting the tests are trained and experienced in using short-pulse radar for pavement thickness measurements.

- Complying with these considerations and following ASTM D4748 will help ensure that pavement thickness measurements using short-pulse radar are accurate and reliable, supporting effective pavement management and maintenance decisions.

ASTM D6432 is a standard practice for using the surface GPR method for subsurface investigation. When using this standard, several key considerations should be kept in mind to ensure that GPR investigations are conducted effectively, and the results are reliable. The following are the main considerations:

- *Equipment Calibration*—Ensure that the GPR equipment is properly calibrated according to the manufacturer’s specifications before conducting any surveys. Calibration is crucial for accurate data collection.
- *Antenna Selection*—Choose the appropriate GPR antenna or antennas based on the specific objectives of the investigation. Different antennas provide varying levels of resolution and depth penetration.
- *Frequency Selection*—Select the GPR frequency range that is suitable for the anticipated depth and resolution requirements of the investigation. Higher frequencies provide better resolution but shallower penetration, whereas lower frequencies penetrate deeper but with lower resolution.
- *Data Collection Parameters*—Set the data collection parameters such as scan rate, scan spacing, and receiver gain according to the expected subsurface conditions. Adjust these parameters as needed during the survey to optimize data quality.
- *Surface Preparation*—Prepare the survey area by clearing it of debris, vegetation, and obstructions that may interfere with data collection. A clean, smooth surface is essential for accurate GPR measurements.

- *Environmental Conditions*—Be aware of environmental factors that can affect GPR data quality, including temperature, moisture content, and electrical conductivity of the ground. Record these conditions during the survey.
- *Survey Grid Design*—Plan the survey grid layout to cover the entire investigation area systematically. Ensure that data overlap and redundancy are accounted for to minimize data gaps.
- *Depth Slices and Time Slices*—Consider using depth slices or time slices to visualize and interpret GPR data at specific depths or time intervals. These slices can aid in identifying subsurface features and anomalies.
- *Data Interpretation*—GPR data interpretation requires expertise. Experienced interpreters should analyze the radar data to identify subsurface features, anomalies, and potential targets. Pay attention to reflection patterns and amplitudes.
- *Ground Truthing*—Whenever possible, verify GPR findings through ground truthing, which involves physically inspecting the subsurface at selected locations. This can help confirm the accuracy of GPR interpretations.
- *Depth Estimation*—Be aware that GPR provides relative depth information. Depth estimates are influenced by the dielectric properties of subsurface materials, which may vary. Calibrate depth measurements based on known features if possible.
- *Layer Identification*—Clearly identify and label subsurface layers, interfaces, and anomalies detected in the GPR data. Differentiate between reflections from geologic features, utilities, voids, and other objects.

- *Data Reporting*—Document all aspects of the survey, including equipment settings, survey parameters, environmental conditions, and data interpretation. Clearly present the results, including the depth and nature of detected features.
- *Safety Precautions*—Implement safety measures to protect personnel and the public during GPR investigations, especially if conducted in high-traffic or potentially hazardous areas.
- *Data Storage and Archiving*—Store collected GPR data in a secure and organized manner. Create backups and archives to ensure data preservation for future reference and analysis.
- *Quality Control and Quality Assurance*—Implement quality control and quality assurance procedures to validate data quality and the reliability of the survey results.
- *Training and Expertise*—Ensure that personnel conducting GPR investigations are trained and experienced in the proper use of GPR equipment and data interpretation.

By carefully addressing these considerations, practitioners can conduct GPR investigations in compliance with ASTM D6432 and produce reliable subsurface information for various applications, including geophysics, engineering, environmental studies, and utility mapping.

CHAPTER 4. NDT TOOLS UTILIZED IN TRANSPORTATION PROJECTS IN THE FIELD

TECHNICAL ASSESSMENT OF NDT TOOLS

Cover Meter (Proceq Profometer 650)

Rebar location is highly important in the on-site testing of RC structures. The **Proceq Profometer 650** helps inspection engineers locate rebars and assess concrete cover values and rebar size using eddy current technology. The Proceq Profometer 650 cannot detect corrosion for analysis. The Proceq Profometer 650 is a cross-scan cover meter. This device uses the **Profometer Link** software to save data to a PC for analysis. Figure 37 shows the Proceq Profometer 650 detector and monitor.



Figure 37. Photo. Proceq Profometer 650 detector and monitor (Screening Eagle™).

Operation (Proceq Profometer 650)

- The **Locate mode** of the Profile meter PM relies on a rifle scope view, enabling the user to quickly position the probe on the center of the rebar in order to mark it on-site.

- The cover value is constantly displayed, and a diameter measurement of the rebar can be performed and detected as the operator scans the wall with the rebar. The green areas indicate where coring and drilling can be performed without the risk of damaging the reinforcement.
- With the Profometer 650, the device software can be used for parallel and orthogonal scans simultaneously. The maximum flexibility in the size of the scanning area allows the user to investigate a pillar in a small portion of the wall, concrete slab, or a bridge deck. When testing on horizontal elements such as decks, slabs and soffits, the extension rod can provide the optimal solution for recording the data.
- An immediate overview of the investigated area can be provided on the device screen. This overview using the **Cross-line mode** includes the rebar arrangement and cover values. The signal strength spectrum delivers a customizable view of the raw signal intensity. Figure 38 and figure 39 show examples of Cross-line mode detection in the Proceq Profometer 650.

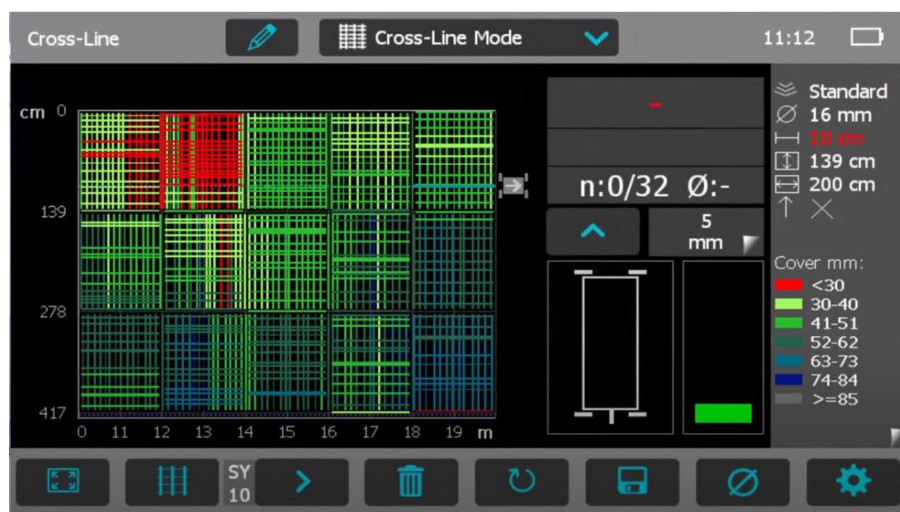


Figure 38. Screenshot. Demonstration of Cross-line mode to display rebar arrangements [21].

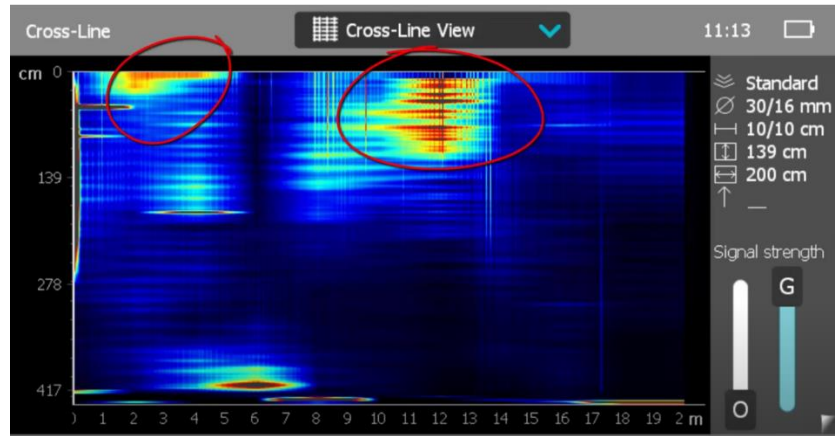


Figure 39. Screenshot. Demonstration of Cross-line view displaying high/low signal intensities [21].

- When detecting the rebar location using the **Single-line view**, the operator can edit the results and remove an inaccurate rebar on the screen. The detection will allow the operator to zoom in and see the exact measurements of the distance between each bar. The Single-line view allows the operator to check for the diameter, desired cover space, and distance traveled by probe. Each line in the Single-line display can be analyzed individually by zooming in on the chosen rebar. Figure 40 shows the Single-line view displaying the rebar parameters and location.

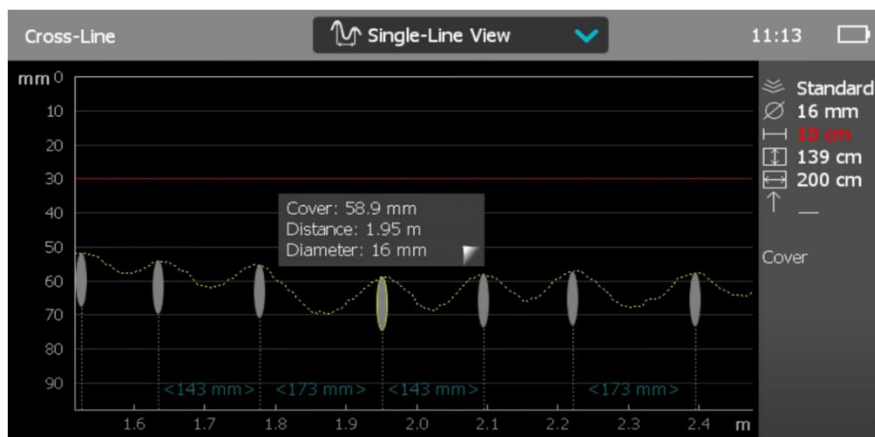


Figure 40. Screenshot. Demonstration of Single-line view displaying rebar parameters and location [24].

- Using the **Multi-line view** combines the number of parallel and linear scans. This means the operator is free to position the scans to any desired spacing. As it scans, a 2D reinforced image is provided with color-coded information about the measured covers. The use of a chalk line delivers a defined grid for an area scan, which is used in combination with the half-cell potential measurements when dealing with corrosion analysis inspections. This device has graphs and statistical charts that can be analyzed for inspection, and these files can be exported. All the tested measurements will be stored in that file for further processing. The graphs highlight the maximum cover value measured in each cell of a user-defined grid and stored. The graphs display the rebar geometry and cover values. The signal strength spectrum measures the signal intensity over the entire (tested) area. When moving the two sliders on the bottom right, the user can refine the spectrum to highlight the desired details in the area for inspection. The overlapping of rebar (or high intensity) is detected by the spectrum of red, orange, yellow, and green colors, versus blue, which indicates lower intensity. Figure 41 shows Multi-line view displaying signal strength intensity.

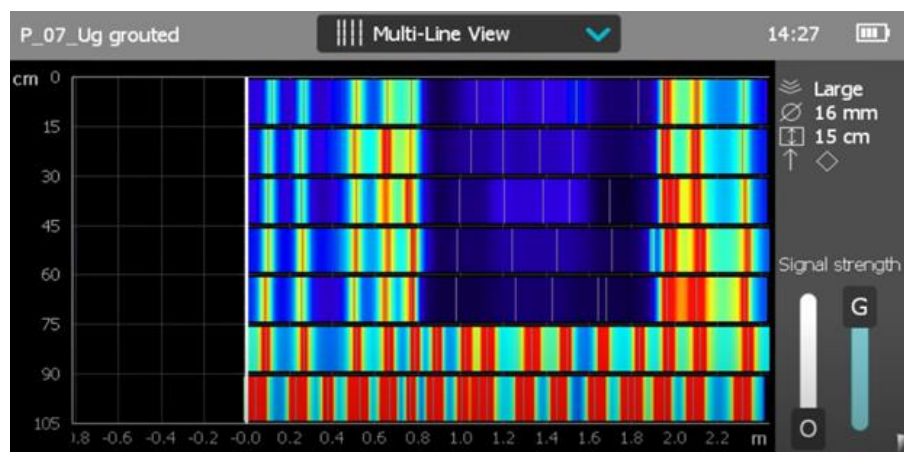


Figure 41. Screenshot. Demonstration of Multi-line view displaying Signal strength intensity [25].

- **Statistics view** allows the operator to view the statistical analysis of the scan, including standard deviation, mean, etc. This allows the operator to check whether the concrete cover is in the expected range. Figure 42 shows the Statistics view for statistical analysis, and figure 43 shows Settings for the Rebar diameter and Maximum and Minimum cover parameters.



Figure 42. Screenshot. Demonstration of Statistics view for statistical analysis [13].

Figure 43. Screenshot. Settings for Rebar diameter, Maximum cover, and Minimum cover parameters (Screening Eagle™).

Profometer Link Software

- The Profometer Link software is based on an integrated suite, enabling the user to process the data coming from rebar detection / concrete cover as well as corrosion potential measurements. The Profometer units can be connected to a PC via USB, and the software is fully compatible with Windows 7, 8, and 10 (32- and 64-bit).
- All features available on the touchscreen unit are also implemented on the PC.
- The user can create custom reports with exported graphs and charts.
- Support is provided for merging of several corrosion scans into a single graph picture and table export (CSV files) for further processing, combined data evaluation, and reporting on any third-party software

Figure 44 shows a screenshot of the Proceq Profometer Link software displaying a Single-line graph, and figure 45 shows Proceq Profometer Link for Multi-line view displaying the Signal strength. Lastly, figure 46 shows examples of Proceq Profometer Link Statistical, Single-line, Multi-line, and Cross-line view graphs.



Figure 44. Screenshot. Proceq Profometer Link software displaying Single-line graph (Screening Eagle™).

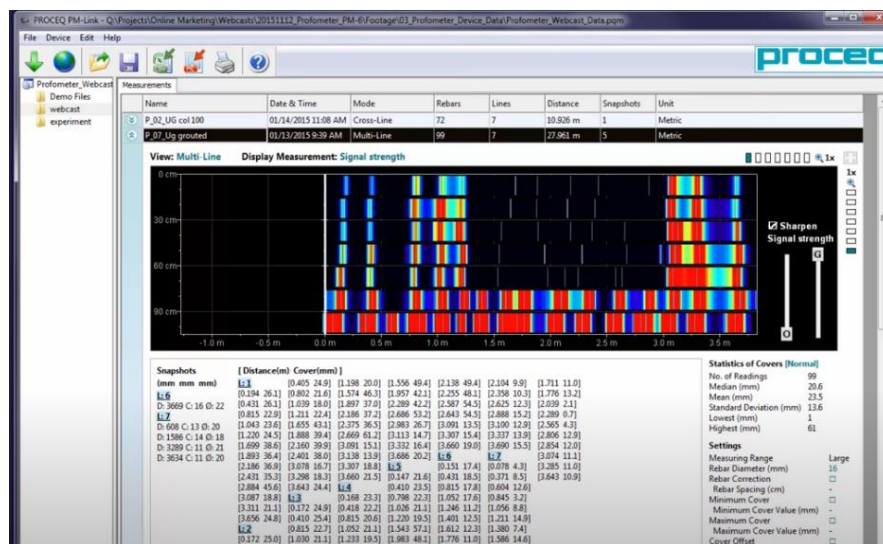
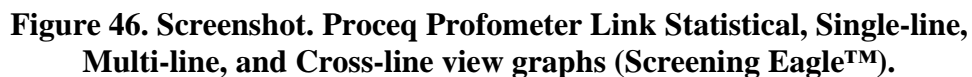


Figure 45. Screenshot. Proceq Profometer Link for Multi-line view displaying Signal strength (Screening Eagle™).



Cover measuring range: Up to 185 mm (7.3 inch); **Cover measuring accuracy:** ± 1 to ± 4 mm (0.04–0.16 inch); **Measuring resolution:** Varies depending on diameter and cover; **Path measuring accuracy on smooth:** Surface ± 3 mm (0.12 inch) + 0.5% to 1.0% of measured length; **Diameter measuring range:** Cover up to 63 mm (2.50 inch), Diameter up to 40 mm (#12), Diameter measuring accuracy ± 1 mm (\pm #1) on single rebar; **Standards and guidelines:** BS 1881-204, DIN 1045, DGZfP B2, SN 505262, SS 78-B4, DBV guidelines, CE certification.

Challenges

- Issues exist with having a clear cover image because of different material properties when using Multi-line view. The solution can be to increase or decrease the filter properties on the device. This can help the user have a clear diameter measurement and check for clear overlapping of rebar.
- The temperature of the concrete can affect the cover image of the rebars.
- The process is known to be time consuming (for ProCeq GPR).
- The device can be difficult to use if the user is not trained properly.

Swiss Hammer (Proceq Schmidt OS8000)

Original Schmidt Live is a versatile tool that works as the following:

- Digital hammer with digital reporting and data sharing (via a free, comprehensive Apple iOS app).
- Digital print console by wirelessly connecting to a Bluetooth printer and directly printing test results.
- Stand-alone digital hammer (using the digital display without the app and downloading the data to the app later, if required).
- Stand-alone analog hammer (using it like an Original Schmidt with the mechanical display, even without a battery).

The Swiss Hammer (Proceq Schmidt OS8000) is used for estimating compressive strength of concrete, mapping concrete uniformity, and controlling concrete curing for formwork removal.

Applications

Original Schmidt Live has multiple applications and is a favorite of the concrete and paper industries and in geology work.

- *Concrete*—Strength estimations, formwork removal, and to complement core testing.
- *Paper*—Roll profiling in mills and converter plants.
- *Geology*—Strength testing, aging, and weathering (field and lab).

Operating Swiss Hammer (Proceq Schmidt OS8000)

European Standard (EN) 12504-2 requires a minimum of nine impacts to calculate one rebound value for the industry standard. This standard describes the data collection and processing of test results. First, unlock the hammer, and then execute the impact. Next, lock the mechanical display in place. Next the scale and write down the number. Repeat these steps eight times.

When using the Schmidt Hammer app, it is connected to the device, which tracks the data for the user. The data are recorded by the hammer and the iPhone app. With the use of the app, the process takes about 25 s. However, if the user does not have access to the app, the process takes about 2 min.

Figure 47 shows the Schmidt Hammer (Schmidt OS8000), and figure 48 shows the Schmidt app demonstration.



Figure 47. Photo. Schmidt Hammer (Schmidt OS8000) (Screening Eagle™).



Figure 48. Screenshot. Schmidt app demonstration (Screening Eagle™).

Calculation of Measurements

The hammer is able to calculate the mean and median and compare each value to the median. Next, the hammer must (1) reject the values that differ from the median by more than 30 percent and (2) reject the entire series if 20 percent or more values are rejected. This process takes a few minutes if the user is performing the calculation by hand. With the Original Schmidt Live app, the median and the impact angle are calculated, which saves time. Figure 49 and figure 50 show the calculation of measurements in the device's app.

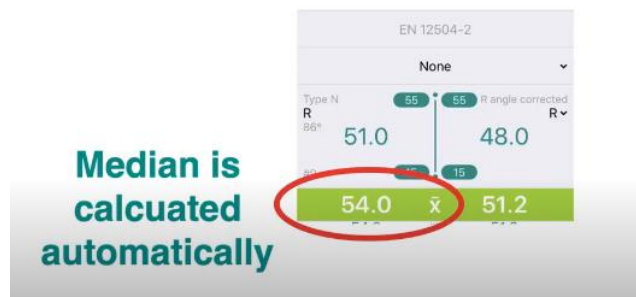


Figure 49. Screenshot. Demonstration of Original Schmidt Live calculating the median (Screening Eagle™).

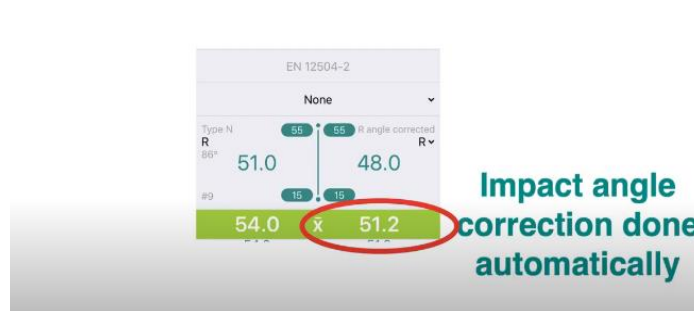


Figure 50. Screenshot. Demonstration of Original Schmidt Live calculating the impact angle correction (Screening Eagle™).

Firmware Upgrade

The Schmidt Live App informs the user when new firmware is available for use. Firmware is a type of software that is etched directly into a piece of hardware. It operates without going through APIs, the operating system, or device drivers. To update the firmware software, the user needs the PQUpgrade software that is available on the Proceq website. First, check if the app is notifying a software update, then go to the website to download PQUpgrade. Next, connect the USB to the Original Schmidt OS8000 hammer and open PQUpgrade. The recommendation is to select “Express” for the latest version. Select the device needed for updating, then click next. The PQUpgrade software will detect the type of hammer. The user will log in to their PROCEQ account, select “Update,” and click “Finish.” Figure 51 shows notification in the app of availability of an update.

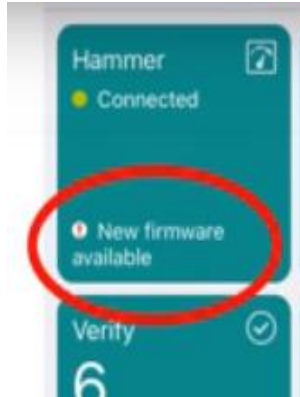


Figure 51. Screenshot. Demonstration of checking the app for availability of an update (Screening Eagle™).

Technical Specifications

Impact energy: Type N 2.207 Nm (1.63 ft lbf); **Impact energy:** Type L 0.735 Nm (0.54 ft lbf);

Housing dimensions: 61 mm × 84 mm × 275 mm (2.4 inch × 3.3 inch × 10.8 inch); **Weight (N-**

hammer): 1090 g (2.4 lb); **Weight (L-hammer):** 850 g (1.9 lb); **Memory:** 2000 measurement

series; **Displays analog & backlit digital:** 100 pixels × 100 pixels, graphic; **Charger**

connection: Micro-USB Battery Standard AAA, alkaline or rechargeable; **IP classification:**

IP54.

Benefits

The Original Schmidt Live app provides the following benefits and advantages:

- Allows for testing in accordance with standards.
- Automatically records all data from the app to a web-based reporting tool.
- Does not require manual data entry.
- Exports reports in PDF or CSV.
- Provides a Logbook feature that summarizes all activity; records GPS locations; and allows the user to add notes, images, and audio comments.

- Provides hammer verification management tools to help keep the hammer calibrated.
- Allows impact results to be heard live in audio on Apple iOS devices via text-to-speech.
- Allows the user to select units, form factor, and correlation curves.
- Allows the user to create custom curve as required by standards.
- Provides automatic data backup.

Standards

- USA—ASTM C805, ACI 228.1R.
- Europe—EN 12504-2, EN 13791.
- China—JGJ-T23
- Japan—JCSE-G504, JIS A1155.
- Russia—GOST 22690-2015.

Standard Warranty

- Electronic components of the instrument—24 months.
- Mechanical components of the instrument—6 months.
- Extended warranty—When acquiring a new instrument, a maximum of 3 additional warranty years can be purchased for the electronic portion of the instrument. The additional warranty must be requested at time of purchase or within 90 days of purchase.

Compressive Strength Range

10–70 MPa (1,450–10,153 psi) 10 to >100 N/mm²

Challenges

Time management can be challenging when the user is calculating the median and impact angle by hand. One rebound value takes about 5 min, and the full nine rebound value checks take over

45 min. In comparison, the Original Schmidt Live app completed one rebound value in 25 s; for the full 9 rebound values, the process took only 3 min 45 s.

Thickness Coating Gage (DeFelsko Corporation, PosiTector 6000)

Introduction/Context

- The rugged, fully electronic **PosiTector 6000** Paint Thickness Gage uses magnetic and eddy current principles to accurately and quickly measure paint thickness on both ferrous and nonferrous metals.
- There are coating thickness gages for all metal substrates.
- The PosiTector 6000 handheld, electronic instrument non-destructively measures the thickness of coatings on metals, quickly and accurately. It consists of a body (standard or advanced) and probe (built-in or separate).

Why Are These Measurements Important to the User?

- Dry film thickness (DFT) is arguably the single most important measurement made during the application and inspection of protective coatings. Coatings are designed to perform their intended function when applied within a tight DFT range as specified by the manufacturer. Correct thickness ensures optimum product performance. Even the most basic specification will require DFT to be measured.
- Many physical and appearance properties of the finished coating are directly affected by the film thickness, including the color, gloss, surface profile, adhesion, flexibility, impact resistance, and hardness of the coating. The fit of pieces assembled after coating can be affected when film thickness is not within tolerance.
- Regular film thickness measurement helps control material costs, manage application efficiency, maintain finish quality, and ensure compliance with contract specifications.

Paint manufacturers recommend target ranges to achieve optimum performance characteristics, and clients expect these parameters to be met.

- Precisely measuring finish thickness has other benefits. Whether to meet International Organization for Standardization (ISO) standards, quality, or customer requirements for process control, companies need to verify coating quality to avoid wasting money reworking products.


How Is This Device Used?

Principles of Operation

- **F** probes use the magnetic principle to measure the thickness of non-magnetic coatings on ferrous metals.
- **N** probes use the eddy current principle to measure the thickness of non-conductive coatings on nonferrous metals.
- **FN** probes combine the full abilities of both the F and N probes.

FN probes first attempt a measurement using the magnetic principle and display a reading with the letter “F” if the coating is non-magnetic over steel. If the coating is non-conductive over metal, then the probe will *automatically* attempt a measurement using the eddy current principle and display a reading with the letter “N”.

First step: The PosiTector 6000 powers up when the center navigation button is pressed. To preserve battery life, it powers down after approximately 5 min of no activity. All settings are retained.

1. Remove the protective plastic cap (if supplied) from the probe.
2. Power up the gage by pressing the center navigation button .

3. Place the probe FLAT on the surface to be measured. HOLD STEADY. When a valid measurement is calculated, the gage BEEPS twice and the measurement is displayed.
4. Lift probe AT LEAST 2 INCHES (5 cm) from the surface between measurements - OR - leave probe on the surface in the same location for continuous measurements.

If memory is ON while continuous measurements are being taken, only the last value on the display (when the probe is lifted) is stored into memory.

Protective Cap and Wrist Strap

Some PosiTector 6000 models are shipped with a protective plastic cap over the probe. Remove this cap prior to use, and replace it when the instrument is not in use to protect the probe. It is recommended to attach and wear the supplied wrist strap.

Plastic Lens Shield

- The LCD is covered with a thin plastic film for protection against fingerprints and other marks during shipment. This film, although usually removed before using the instrument, can be left in place to protect against paint overspray. Replacements can be purchased.

Golden Rule

- Measure your uncoated part first! This quick zero-check determines if a **Calibration Adjustment** is needed for your substrate.
- Next, lay the included plastic shims onto a bare surface and measure them individually to ensure the gage measures a known thickness within tolerance.

Certification of Calibration for Probes

- All probes include a Certificate of Calibration. For organizations with re-certification requirements, instruments may be returned at regular intervals for calibration. DeFelsko Corporation recommends that customers establish calibration intervals based upon their

own experience and work environment. Based on DeFelsko Corporation's product knowledge, data, and customer feedback, a 1 year calibration interval from either the date of calibration, date of purchase, or date of receipt is a typical starting point. Written calibration procedures are available from DeFelsko Corporation at no charge.

PosiTector 6000 probes non-destructively measure the thickness of coatings on metals. Three steps ensure best accuracy:

1. *Calibration*—Typically done by the manufacturer. All probes include a Certificate of Calibration.
2. *Verification*—Typically done by the user on known reference standards, such as plastic shims or coated thickness standards.
3. *Adjustment*—To a known thickness.

Calibration

Calibration is the high-level, controlled, and documented process of measuring traceable calibration standards over the full operating range of the probe and verifying that the results are within the stated accuracy of the probe. Calibrations are performed by the manufacturer, their authorized agent, or by an accredited calibration laboratory in a controlled environment using a documented process.

PosiTector 6000 probes are shipped with a Certificate of Calibration showing traceability to a National Metrology Institution. For organizations with re-certification requirements, probes may be returned at regular intervals for calibration. DeFelsko Corporation recommends that customers establish calibration intervals based upon their own experience and work environment. Based on DeFelsko Corporation's product knowledge, data, and customer feedback, a 1 year

calibration interval from either the last date of calibration, date of purchase, or date of receipt is a typical starting point. Written Calibration Procedures are available online at no charge.

Verification

Verification is an accuracy check performed by the user on known reference standards. A successful verification requires the gage to read within the combined accuracy of the probe and the reference standards.


A reference standard is a sample of known thickness(es) against which a user may verify probe accuracy. Reference standards may be plastic shims, coated thickness standards, or sample parts for which coating thickness has been determined using other means.


Accuracy should be verified at the beginning and the end of each work shift. During the work shift, if the gage is dropped or suspected of giving erroneous readings, its accuracy should be re-verified. In the event of physical damage, wear, high usage, or after an established calibration interval, the probe should be returned to the manufacturer for repair or calibration.

Adjustment

Adjustment, or Cal adjustment, is the physical act of aligning the probe's thickness readings to match those of a known thickness sample (removal of bias) in order to improve the accuracy of the probe on a specific surface or in a specific portion of its measurement range. Either 1-point or 2-point Cal adjustments are possible.

Probes are factory-calibrated and perform an automatic self-check each time a measurement is taken. For many applications, no further adjustment is necessary after a **Reset**. Just check ZERO on the uncoated substrate, and then measure. However, sometimes probe readings can be influenced by changes in substrate shape, composition, and surface roughness or by measuring in

a different location on the part. That is why Cal adjustments are made possible. The  symbol disappears whenever a Cal adjustment is made.

Where a Cal adjustment method has not been specified, use a 1-point method first. If measuring the included shims on the uncoated surface reveals inaccuracies, use the 2-point method. Factory Cal settings can be restored at any time by performing a **Reset**, creating a NEW Cal setting (see **Cal Memory**), or by DELETING the adjustments made to the Cal 1 calibration setting. The  symbol appears on the display whenever factory Cal settings are in use.

With FN probes, calibration adjustments are made only to the “F” or “N” mode (stored independently under a particular Cal), whichever was measured last. Figure 52 shows the typical screen and bottom functions.

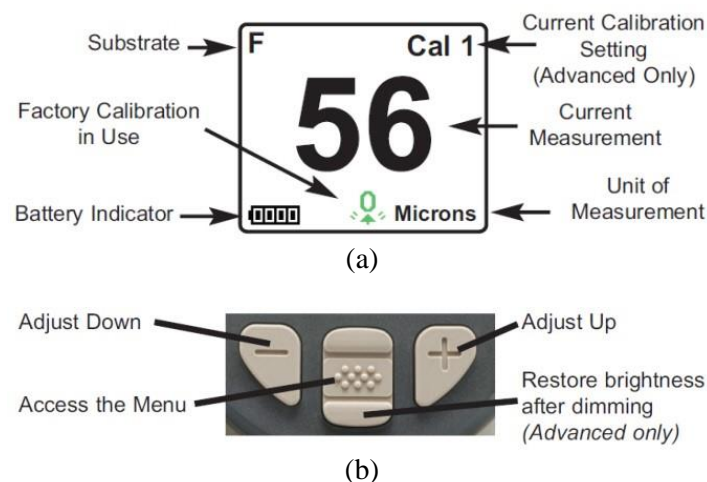


Figure 52. Images. PosiTector 6000: (a) typical screen and (b) bottom functions.

Probe Information

- The PosiTector 6000 consists of a **body** and a **probe**. A wide selection of interchangeable probes is available. Each retains its own unique calibration information. **All gage bodies accept ALL probes.**
- To disconnect a probe from a body, slide the plastic probe connector horizontally (in the direction of the arrow) away from the body. Reverse these steps to attach a different probe. It is not necessary to power down the gage when switching probes.
- When powered up, the PosiTector automatically determines what type of probe is attached and performs a self-check. Coating thickness probes “sense” when they are near metal and immediately attempt a measurement, followed by another every 2 s. They stop when removed from the vicinity of metal and power down after 5 min of no activity.
- This continuous measurement feature is intended to allow careful probe placement on small or odd-shaped surfaces. Ignore all readings taken before the probe is properly placed.

Two Probe Styles

- *Integral*—Sensor protrudes from bottom of probe connector.
- *Cabled*—Sensor is attached to the probe connector by a 1.2 m (3 ft) cable (extended cable length available).

Available Positector 6000 Probes

- *Regular*—These constant-pressure, stainless steel probes are hermetically sealed to be totally waterproof and are ideal for underwater use.
- *Micro*—Ideal for measuring small parts and hard-to-reach areas. Available in 0°, 45°, or 90° angles.

- *Thick*—Ideal for thick, protective coatings.
- *Xtreme*—Ideal for measuring rough and/or hot surfaces up to 250°C (500°F).
- For complete details, see <https://www.defelsko.com/p6000-probe-details>.

Additional PosiTector Probes

- The PosiTector body accepts a wide variety of probe types, including magnetic, eddy current and ultrasonic coating thickness, surface profile, environmental, Shore hardness durometer, salt contamination, and ultrasonic wall thickness probes (figure 53).



Figure 53. Photos. PosiTector probes.

Technical Specifications

Measuring Range: Varies depending on probe model; **Accuracy:** Varies depending on probe model; **Resolution:** Varies depending on probe model.

Temperature Range:	Gage Size:	Weight:
+32° to +120°F (0° to +50°C)	137 mm × 61 mm × 28 mm (5.4 inch × 2.4 inch × 1.1 inch)	140 g (4.9 oz)

Challenges

Common challenges are as follows:

- Probe takes a measurement even while held in the air.
- Thickness readings are inconsistent.
- Gage powers up but will not take any readings.
- Gage will not print to the Bluetooth wireless printer.

These issues can be addressed as follows.

Probe takes a measurement even while held in the air:

- The probe tip may have been left near metal, including jewelry, during power up or at rest, or possibly a finger was held over the probe.
 - Try measuring an uncoated object. Otherwise, turn the gage off and then on again.
- Finally, try a Reset.

Thickness readings are inconsistent:

- Probe tip may be damaged, scratched, or worn.
 - Ensure the probe is fully clearing the surface between measurements.
 - Try measuring a different surface with the included plastic shims.
 - Hold the probe onto the surface and allow it to take several measurements. If the second and subsequent measurements are consistent, the user was not putting the probe onto the surface fast enough.
- The substrate and/or coating surface is uneven, in which case inconsistent readings are to be expected.
 - Take several measurements and average them to get a meaningful result.

Gage powers up but will not take any readings:

- Substrate may not be metal. F probes measure coatings on ferrous metals, such as steel and iron, and N probes measure over nonferrous metals, such as aluminum.
- Protective cap must be removed from probe (if outfitted with one).
- An extreme calibration adjustment might have been made.

Gage will not print to the Bluetooth wireless printer:

- Ensure the gage has been paired for use with the printer and the gage menu option Connect > Bluetooth > Stream box is ticked.
- Check printer batteries.
 - Switch it off and then on again.

Note: Most conditions can be cleared with a hard Reset.

Resistivity Resipod (Proceq)

Introduction/Context

- The Proceq Resipod Resistivity Meter (figure 54) is used to evaluate the electrical resistivity of concrete surfaces that correlates directly to the permeability, likelihood, reinforcing steel corrosion rate, and chloride diffusion rate.
- **Resistivity** is the electrical resistance of a conductor of unit cross-sectional area and unit length. A characteristic property of each material, resistivity is useful in comparing various materials on the basis of their ability to conduct electric currents.
- Resistivity defines the permeability and durability of the concrete.
- The thicker the concrete, the greater the resistance when the current is passing through.

- The thinner the concrete, the weaker the resistance will become when the current is passing through.
- *Lower resistivity* equates to high conductivity.
- *Higher resistivity* equates to lower conductivity.

Background for the needed use of the Proceq Resipod:

- Corrosion of the reinforcing steel is the primary cause of deterioration of concrete structures.
- The lifespan of a structure depends on the concrete's ability to provide physical and chemical protection for itself.
- Electrical resistivity can help the concrete resist the contact of highly hostile substances that will create corrosion that results in a decrease in the life span. Examples of hostile substances are chloride or carbon dioxide. Those substances' high concentration will destroy the iron oxide coating on the rebars in the concrete and it will start to erode.



Figure 54. Photo. Proceq Resipod Resistivity Meter.

How is the Proceq Resipod used?

- The Resipod is fairly easy to use. Once the Resipod is assembled, turn it on and align the sensor with the concrete slab to be measured.
- A calibration device calibrates the Resipod to ensure that it is working correctly.

Applications of the Proceq Resipod include the following:

- Estimate the probability of corrosion.
- Indicate the corrosion rate.
- Correlate the permeability of chloride.

Considerations when testing include the following:

- On-site evaluation of the efficacy of healing.
- Identification of needs by area of cathodic protection systems.
- Identification of wet and dry areas in a concrete structure.
- Notation of statement of changes in relationships water / cement in a concrete structure.
- Identification of areas in a structure more susceptible to penetration of chloride.
- Correlation with early resistance to compression.
- Correlation with the rock permeability to water.

Benefits

- Can be correlated with a likelihood of corrosion of the structure.
- Creates a relationship between the resistivity of concrete and chloride diffusion rate.
- Determines the resistance to compression of concrete early.
- Provides versatility because it has easy applications.

Technical Specifications

Measured Quantity: Electrical resistivity (k Ω cm); **Accuracy:** From ± 0.2 to ± 2 k Ω cm

(depending on resistivity range); **Instrument Firmware:** Highest resolution available for a surface resistivity instrument current flow indication and poor contact indication (Hold, save, and delete function); **PC Software:** ResipodLink to view and manipulate the data on a connected PC.

It also allows a variable contact spacing to be set; **Display:** Pixel graphic LCD; **Memory:** 500 measured values; **Connections:** USB type B; **Measuring Range:** 1 to ~1000 k Ω cm (depending on probe spacing); **Probes/Electrodes:** In addition to the standard Wenner probe with spacing of 50 or 38 mm (1.5 inch), additional variable spacing probe and bulk resistivity accessories are available.

Technical Assessment of GPR (Proceq GP8000)

Introduction/Context

- Proceq GP8000 Live GPR system (figure 55) for concrete testing is a handheld device. This GPR concrete scanner features ultra-wideband detection for unparalleled subsurface evaluation of concrete slab, bridges, buildings, pavements, and other concrete structures.
- GPR Live real-time concrete scanning covers multiple individual GPR antennas ranging 0.2–4.0 GHz.
- GPR operates by transmitting EM waves (in the range of 10 ~ 1000 Hz) into the probed material and receiving the reflected pulses as they encounter discontinuities. The discontinuity can be the boundary or interface between materials.
- The amplitudes of the received echoes and the corresponding arrival times can then be used to determine the nature and location of the discontinuity.
- GPR can be used for subsurface condition assessment in materials consisting of thin layers, such as fiber-reinforced composites. The analysis of different GPR waveforms can potentially help detect subsurface debonds between the wearing surface and the underlying fiber-reinforced polymer (FRP) bridge deck, and delaminations within the flanges of the FRP deck.

- Delamination is a separation along a plane parallel to a surface, as in the separation of a coating from a substrate or the layers of a coating from each other or, in the case of a concrete slab, a horizontal splitting, cracking, or separation near the upper surface (figure 56).



Figure 55. Photo. GPR (Proceq GP8000 TM).

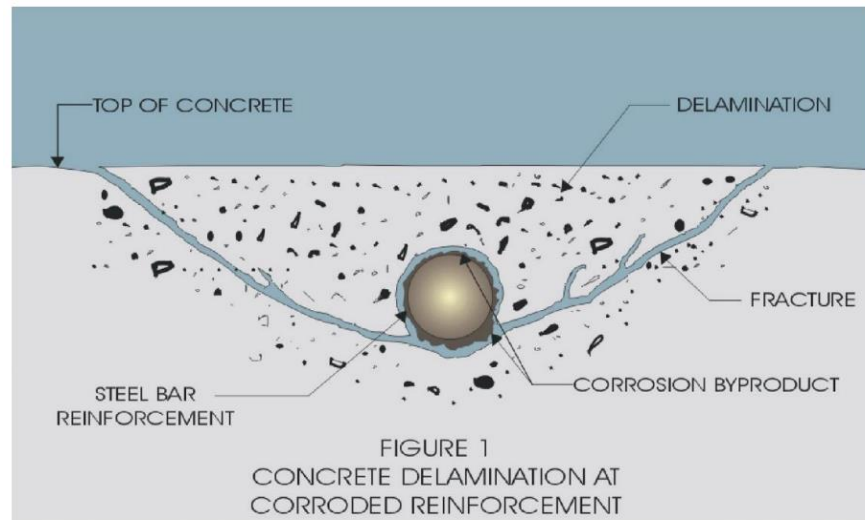


Figure 56. Schematic. Concrete delamination.

Working Principle

Figure 57 shows a schematic of the GPR working principle.

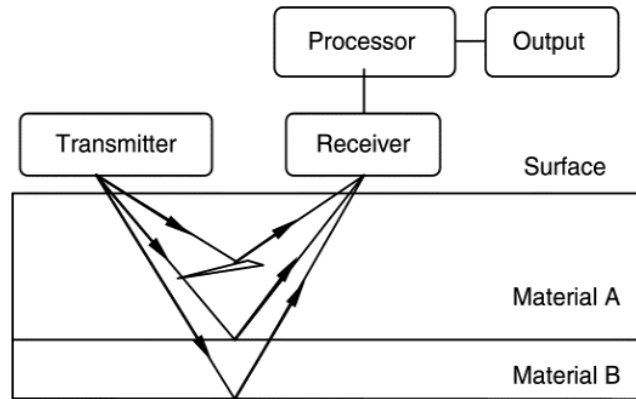


Figure 57. Schematic. GPR working principle.

Measurement Modes

Superline scan (1000 m [3281 ft]); Area scan (with flexible grid up to 100 m² [1076 ft²]).

Review Modes

Superline scan, A-scan (incl. envelope), Migrated view, Non-migrated view, Split view, Time-Slice view, Basic 3D view, Augmented reality (AR).

Advanced Visualization

Time-slice view Pro, 3D view, AR.

Reporting

Workspace integration, Automatic logbook, SEG-Y export, Instant report generation, Share via URL.

Technical Specifications for Instruments

Radar technology; SFCW GPR; **Modulated frequency range:** 200–4000 MHz; **Penetration depth:** 80 cm (31.5 inch); **Battery:** Flight-safe, removable pack; 8× AA (NiMH); **Dimensions:** 22.1 cm × 18 cm × 14 cm (8.7 inch × 7.1 inch × 5.5 inch).

Standards that must be met:

ASTM D4748, ASTM D6087, ASTM D6432, AASHTO R 37, and EN 302066-ETSI.

Other NDT Tools

Proceq GS8000

Introduction/Context

Proceq GPR Subsurface is the all-in-one solution for detecting objects and mapping the underground world using SFCW GPR technology. Proceq GS8000 software can be utilized with a Windows tablet (figure 58a). The base of the Proceq GS8000 is shown in figure 58b.



Figure 58. Photos. Proceq GS8000: (a) device with the tablet and (b) base.

Benefits

Proceq GS8000 Subsurface app; Software / Workspace App; Technical Specifications:

Acquisition modes: Line Scan, Area Scan, Free Path; **View modes:** A-scan, Line Scan non-migrated, Line Scan migrated, Time Slice View, Map View, 3D, Augmented Reality; **On-site**

annotations: Tags, markers, points of interest, lines, photos, notes, voice notes, markups;

Adjustable display settings: Color palette, linear gain, time gain compensation, background removal, multi-layer dielectric constant, time window, noise cancellation filter, frequency filter, low pass filter, slice depth, slice thickness; **Data options:** Cloud storage, SEG-Y export, HTML export, KML export, DXF export, SHP export; **Display unit:** Any iPad® or iPad Pro®,

Recommended: iPad Pro Wi-Fi+Cellular (M1), Screen resolution: up to 2732 pixels × 2048

pixels, Storage capacity: up to 1 TB; **Max. scan length:** Up to 15 km (9.3 mi); **Max. scan grid**

size: Up to 80 m × 80 m (260 ft × 260 ft), Stepped-frequency Continuous-Wave GPR;

Modulated frequency range: 40–3440 MHz; **Effective bandwidth:** 3200 MHz; **Min.**

detectable target size: 1 cm (0.4 inch); **Max. depth penetration:** 10 m (33 ft); **Scan rate:** 500

Hz; **Spatial interval:** Up to 100 scans/m; **Acquisition speed:** Up to 80 km/h (50 mph); **GNSS**

receiver: Multiband GPS + Glonass + Galileo + Beidou, SSR augmentation / RTK-compatible,

Dimensions: 145 mm × 145 mm × 70 mm, Weight: 0.7 Kg, 4× AA batteries, included; **GNSS**

real-time 3D accuracy: Typ. 1–5 cm (0.5–2 inches); **GNSS initialization time:** Typ. 5–30 s;

Wheel encoders: 2; **Configuration:** Wireless integrated push & pull cart; **Weight:** 24 kg;

Dimensions: 61 cm × 57 cm × 38 cm; **Antenna positions:** Ground-coupled with dual-axis

floating, Air-coupled with 25 mm clearance; **Ingress protection (IP) / sealing:** IP65; **Power**

supply: Removable flight-safe battery pack, Off-the-shelf power bank; **Autonomy:** 3.5 hr | Full

working day; **Operating temperature:** –10°–50°C (14°–122°F); **Operating humidity:** <95%

RH, non-condensing; **Connectivity:** Wi-Fi, Ethernet, USB-A, USB-B, USB-C, Lemo.

Additional Information

- Run an up-to-date iOS version; recommended models: iPad Pro[®] Wi-Fi + Cellular 11 or 12.9 inch.
- For USA and Canada: 200–3440 MHz.
- Metallic object buried at 0.3 m (1 ft), in average soil conditions.
- Depending on soil conditions, typ. 6 m (20 ft) in average soil conditions. For USA and Canada: 12 ft in average soil conditions.
- At 50 mm scan interval. For USA and Canada: Up to 35 km/h (22 mph).
- Service available in Europe and USA; needs an active Internet connection on the iPad.
- Via NTRIP RTK or SSR corrections; the achieved accuracy is subject to atmospheric conditions, satellite geometry, observation time, etc.
- Batteries and tablet not included.
- Contains 8× rechargeable C-Type NiMH batteries.
- USB-C PD power bank with maximum dimensions: W 85 mm × H 28 mm; recommended power: 12V/≥1.25A or 15V/≥1A.
- Recommended battery capacity: >4500 mAh.
- Recommended power bank capacity: >20,000 mAh.

Challenges

- The device is relying on the Apple iPad to operate.
- Because of the complex software configuration, connection problems can happen from time to time.

- Bluetooth, Wi-Fi, and internet connections can be a problem in areas with an EM field present, such as power electricity, power substation rooms, etc. This can slow down the process of seeing accurate results in real time.
- Capital costs are comparatively average compared to other GPR units available on the market.

Proceq Pundit PD8050

Introduction/Context

Applications: Location of subsurface defects of concrete; Measurement of thickness of concrete elements; Determination of concrete pulse velocity for homogeneity and strength estimation.

The **Proceq Pundit PD8050** provides consolidated power in a single device for structural imaging and object and defect detection with ultrasound pulse echo.

Working Principle

The following are the types of scans that the Pundit PD8050 can operate on and how it works.

The PD8050's iOS App allows immediate imaging of UPE data. This image can be shown in a conventional B-scan or C-scan format or be processed into a full 3D iso-surface representation on-site. figure 59a shows the Stripe scan (on-site 3D) mode.



Figure 59. Photos. PD8050 iOS app: (a) Stripe scan (on-site 3D) mode and (b) Line scan mode operation.

The user places the AI positioning tape perpendicular to the PD8050 array and then moves it forward in a strip. The Pundit PD8050 starts collecting 3D data in the area underneath the array's motion. It may be shown as a Time-slice/Depth-slice view, or as a 3D iso-surface. The user places the AI positioning tape parallel to the PD8050 array, moving it sideways along the structure and producing one long Line scan. The data may only be shown as a Line scan view. Figure 59b shows the Line scan mode operation.

NDT Tool Not Utilized but Beneficial to Investigate

Cementometer T-C-10R (James Instrument)

This device measures the water/cement (w/c) ratio for Type I/II cements.

Introduction/Context

A microwave meter for rapid determination of moisture content in wet cement and concrete, the **T-C-10 Cementometer Type R™** (figure 60) is for standard-range w/c ratios.



Figure 60. Photo. T-C-10 Cementometer Type R™.

The Cementometer™ represents a breakthrough in modern moisture measurement technology. By utilizing the latest microwave and microprocessor science, the Cementometer™ can determine the moisture content of freshly mixed cement, concrete, and mortar. Simply insert the prongs of the probe into the material to be measured and instantaneously the w/c ratio is shown on the easy-to-read display.

How is This Device Used?

The Cementometer™ Microwave moisture meter uses a two-prong sensor to measure the complex dielectric constant of the material in contact with the prongs. Because the dielectric constant of water is four to eight times greater than most aggregates and cements, changes in water content directly affect the sensor output. An average of 5–10 readings is normally taken to ensure a valid reading. This output is then converted by the integrated microprocessor, and moisture content is displayed directly. Two units are available to encompass the full range of w/c ratios found in wet concrete. The Cementometer Type R™ handles normal w/c ratios with its two-prong probe. The range of this instrument is approximately 0.35–0.65 w/c. Cementometer

Type L™ handles low w/c ratios with its five-prong probe. The range of this instrument is approximately 0.2–0.4 w/c. The units come calibrated for standard Type I, II, and III cements. A unit can also be programmed with up to 10 different mix designs by the user. For highest accuracy, the user should program the unit for the material being used. The Cementometer Type R™ has a user-friendly calibration process that rapidly creates the user programs without the need for external computing devices. Finally, the Cementometer™ can store over 150 readings. Storage is complete with the time and date for future reference. Data can be recalled via USB interface to a PC running the James Cementometer™ software.

Benefits

- Fast and easy to use; simply insert the prongs into the material being tested.
- Accurate.
- Completely portable.
- Full range of w/c ratios instantaneous readings.

Technical Specifications

T-C-10	Cementometer Type R™ for Regular w/c Ranges
w/c Ratio Range	Approximately 0.35–0.7
Power	4 AA batteries
Display	2 × 16 characters transmissive – reflective
Data Link	USB
Weight	Approximately 4 lb (1.8 kg)

REVIEW OF GPR POST-PROCESSING SOFTWARE

The following section is a review of two software packages available for processing GPR data.

Screening Eagle Technologies offers two post-processing applications to GPR users: GPR Slice and GPR Insights. Both require a paid subscription to use, but there is a 30-day free trial available for each. The authors gained access to the free trials for both applications with the objective of extracting the A-scan data from GPR, which shows the energy-curve graph in the form of amplitude versus time. The Proceq GP8000 software does not display any numerical values on the A-scan data. As shown within the ASTM standards and other related literature, obtaining amplitude values for a set of GPR data can provide information regarding the materials beneath the surface. Specifically, the reflections from rebar can indicate the condition of the surrounding area. Strong reflections typically represent sound concrete, whereas weak reflections indicate deterioration. Obtaining the amplitude values allows users to plot and create graphs that display levels of deterioration, as mentioned in ASTM D6087 for evaluating concrete bridge decks with GPR.

GPR Slice

The GPR Slice application provides post-processing techniques, such as signal processing and image processing. This software requires installation on a desktop, so it can only be accessed through the computer it was downloaded on. The process of uploading a file and analyzing it was not user-friendly and may be difficult to navigate for someone who has never used it before. Lastly, extracting the amplitude values did not seem possible through this application. After contacting Eagle Screening, they suggested we try GPR Insights. A snapshot of GPR Slice is shown in figure 61. This image shows the hyperbolic fitting to find the dielectric of the material by fitting the hyperbola over the rebar. However, this specific result does not seem accurate, as it shows the dielectric of a concrete floor being 11.11. The dielectric constant of concrete ranges 4–10 and is mentioned in ASTM D4748. Therefore, this specific feature is dependent on the

interpretation of the user and must be done carefully. However, GPR Slice offers many other features and more information can be found at <https://www.gpr-survey.com/>.

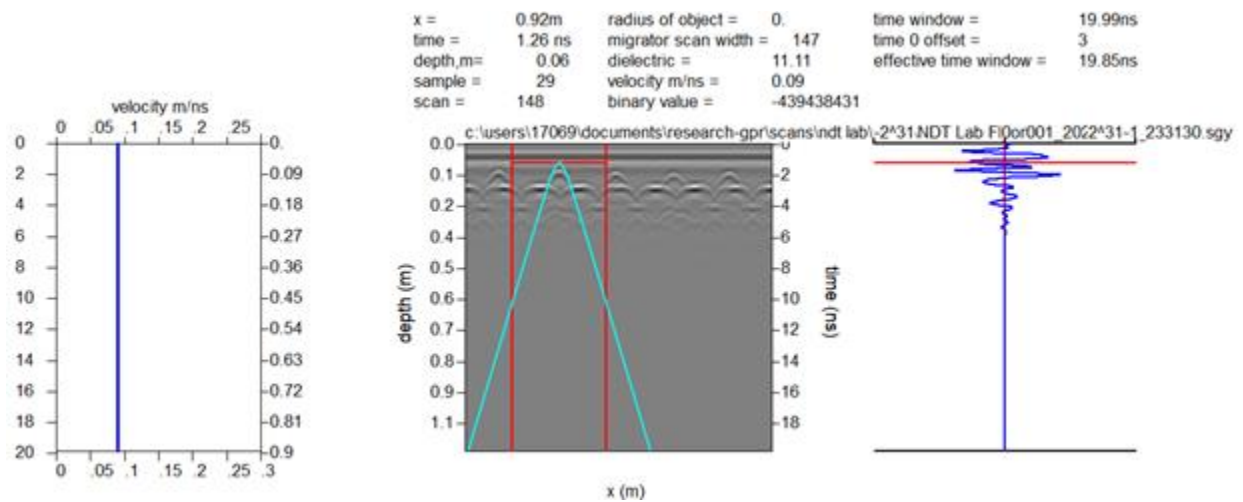


Figure 61. Graphs. GPR Slice results of hyperbola fitting.

GPR Insights

GPR Insights is a web-based application, so it can be accessed on any device through the Screening Eagle Workspace. From there, the user can easily transfer the GPR files onto the platform. This software is simple to use and straightforward for editing the scans. The user can export the GPR data into many different file formats: Video, DXF, SHP, KML, CSV, XYZ, and XYZA. The authors evaluated the XYZA file format. This is a comma delimited text file and can be opened with Notepad. From this, the data are shown in column form, displaying the X and Y points, which could be relative or UTM coordinates if used with a GPS. The Z represents the time in nanoseconds, and A is the normalized signal amplitude. Normalizing the amplitude means to change the amplitude to meet specific criterion or norm. When exporting an XYZA file from GPR Insights, the user selects a specific depth or time from which to extract the amplitude

values. Figure 62 shows a GPR scan that was uploaded to GPR Insights to test this feature. The depth was set to 2.718 inches at the top of the rebar, and the values were extracted.

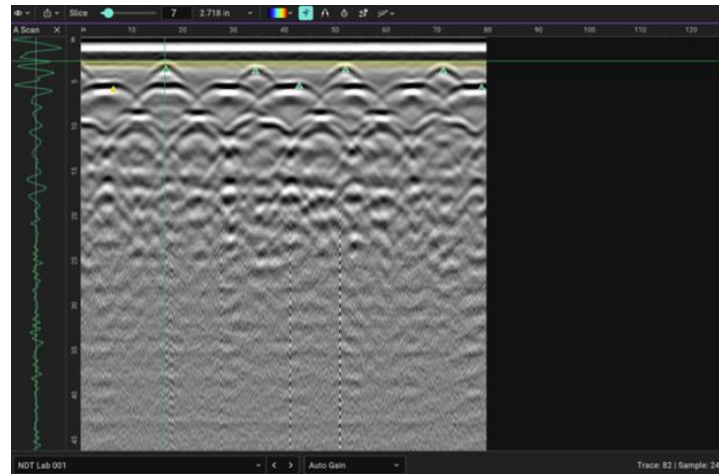


Figure 62. Scan. GPR data in GPR Insights with time gain.

Because the user only obtains amplitude values for that specific time or depth, plotting the amplitude versus time graph cannot easily be done. The user would have to go through every depth of the scan and extract the values and then match them with the corresponding position to obtain a similar energy-curve graph as shown on the left of the scan. Keep in mind that this graph changes with each x -position, so doing this for a whole scan would be time-consuming.

Although obtaining amplitude values with the current equipment is not easy, GPR Insights also offers the following:

- Deterioration map—Qualitative map of the condition of the bridge decks based on ASTM D6087.
- Condition map—Qualitative map of the degradation of concrete or steel at the top rebar layer.

These maps show the GPR results in a way that is easier for interpretation because certain colors represent deterioration. A snapshot of these features is shown in figure 63.

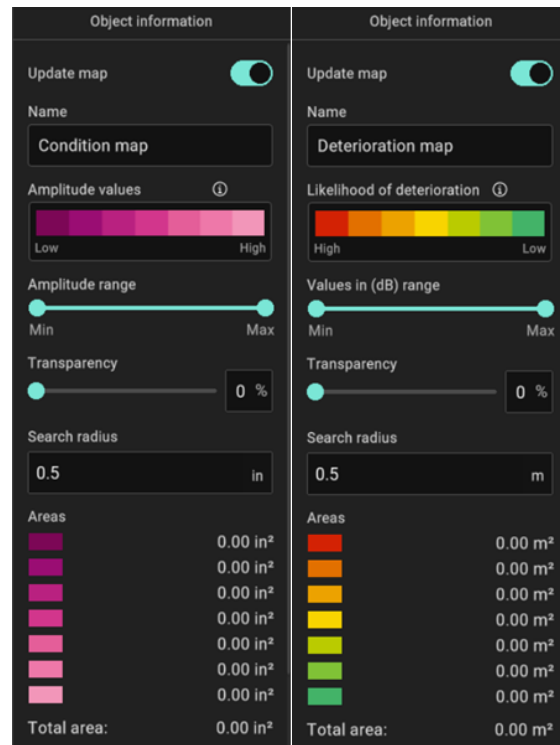


Figure 63. Screenshots. GPR Insights: features of the condition map (left) and deterioration map (right).

Figure 64 illustrates how the reflection amplitudes will appear when there is sound concrete versus signs of deterioration [24]. As mentioned above, a higher reflection amplitude produced from the rebar indicates sound concrete, whereas a lower reflection amplitude produced from the rebar likely shows signs of deterioration. Similarly, this information can be observed on the B-scan image produced from the GPR, and an example is shown in figure 64 [25]. The hyperbolic signature for rebar in sound concrete is distinct because there is a strong reflection. Comparably, if there is a weak reflection from the rebar, the hyperbolic signatures are not as visible.

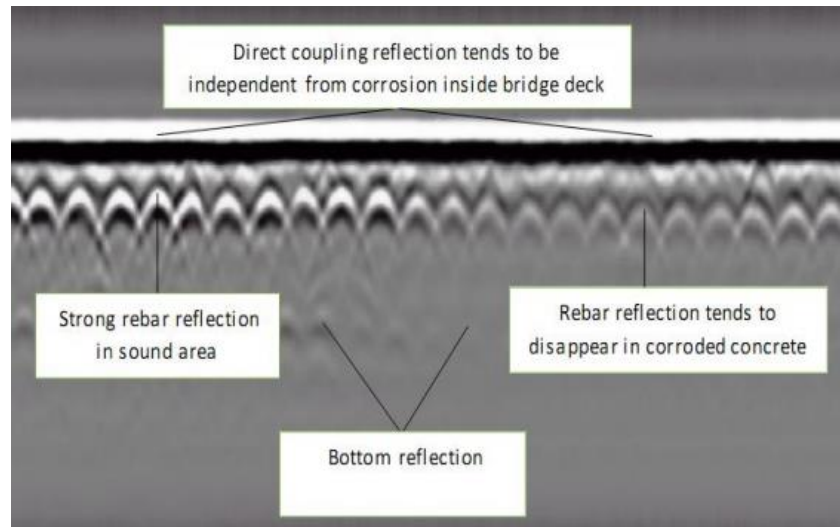



Figure 64. Image. B-scan image of bridge deck [25].



COMPARISON OF EQUIVALENT AND MAJOR GPR PRODUCTS


Table 18 presents summaries of equivalent major GPR products from two main suppliers (Screening Eagle TechnologiesTM and GSSITM) for comparison purposes.


Table 18. Summary of GPR products (Screening Eagle™ and GSSI™).


Proceq GS8000 Proceq GS8000 Subsurface mapping	GSSI UtilityScan https://www.geophysical.com/products/utilityscan
	
Radar Technology: Stepped-frequency Continuous-Wave GPR, Wireless Satellite Antenna	Radar Technology: RADAN 7 for UtilityScan, Wireless Satellite Antenna
Modulated Frequency Range: 40 – 3440 MHz	Modulated Frequency Range: 350 MHz
Penetration Depth: 10 m 33 ft ³	Penetration Depth: 10 m (35 ft)
Battery: Removable flight-safe battery pack ¹¹ Off-the-shelf power bank ¹²	Battery: Lithium-Ion
Dimensions: 61 x 57 x 38 cm ⁹	Dimensions: 22 x 19.25 x 12.5 in / (56 x 49 x 32 cm)
Weight: 24 Kg	Weight: With Tablet & Battery 16.8 kg (37 lbs)
Applications: Damage prevention, Excavation safety, Utility locating & mapping, Subsurface utility engineering (SUE), Surveying & Reality Capture, Road inspection, Bridge inspection, Geophysical investigations, Archaeology, Forensics & UXO, Precision Agriculture	Applications: Scan utilities – metallic and non-metallic, Locate water lines, Detect voids and underground storage tanks (USTs), Identify soil and foundation characteristics, Locate shallow objects for archaeology
Proceq GS8000 Includes:	UtilityScan Includes: 350 HS antenna (350 MHz), Panasonic G2 Toughpad, Lithium-ion battery (2), Dual-bay battery charger, Rugged 2 m ethernet cable, LineTrac, optional, Sunshade for G2 Toughbook, Quick Start Guide, 2-year warranty
Accessories: Battery pack, Power bank drawer, Wear plate, GNSS pole fixation kit, Wheel position adapter kit, Wheel 30cm, Universal tablet holder, Sun & rain cover for tablet, Umbrella holder kit, RAM-mount adapter for tablet, DB9 to Lemo adapter, Lemo to lemo cable, Hard transportation case	Accessories: Geode GPS, Transit case, Model 626 survey cart, Model 656 survey cart

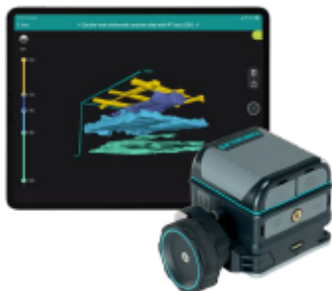
Proceq GS9000 Pro GX1 GS9000 Multichannel GPR system	GSSI Utility Scan Pro GPR For Utility Mapping and Locating UtilityScan Pro System GSSI (geophysical.com)
	
Radar Technology: Stepped-frequency GPR, Wireless Satellite Antenna	Radar Technology: RADAN 7 for UtilityScan, Wireless Satellite Antenna
Modulated Frequency Range: 500 – 3000 MHz ² 30 – 750 MHz ³	Modulated Frequency Range: 400 MHz, 300/800 DF, 350 HS
Penetration Depth:	Penetration Depth: 0-12 m (0-40 ft)
Battery: Off-the-shelf power bank ⁴	Battery: Inspired Energy Ni2040ED, 3 hour runtime (battery life dependent on level of display brightness)
Dimensions: 722 x 1178 x 443 mm	Dimensions: 14x10x2.75 in / (36x25x7 cm)
Weight: 45 Kg ²	Weight: 27.2-34 kg (60-75 lbs) (cart dependent)
Applications: Damage prevention, Excavation safety, Utility locating & mapping, Subsurface utility engineering (SUE), Surveying & Reality Capture, Road inspection, Bridge inspection, Geophysical investigations, Archaeology, Forensics & UXO, Precision Agriculture	Applications: Underground utility detection, Environmental remediation, Damage prevention, Geological investigation, Archaeology, Forensics, Road inspection
GS9000 Includes:	Utility Scan Pro Includes: SIR 4000 Control Unit, 400 MHz, 300/800 DF, or 350 HS Antenna, Choice of 3-wheel or 4-wheel cart, 2 m control cable, SIR 4000 sunshade, SIR 4000 AC/DC power supply, Lithium-ion battery (2), Dual-bay battery charger, Transit case, 2-year warranty
Accessories:	Accessories: LineTrac, Juniper Geode GPS, Tripod for 3-wheel survey cart

Proceq GP8000 Proceq GP8000 Portable Ground Penetrating Radar	GSSI Flex NX Flex NX - GSSI Geophysical Survey Systems, Inc.
	
Radar Technology: Stepped-frequency continuous-wave (SFCW) GPR, Wireless Satellite Antenna	Radar Technology: Wireless Satellite Antenna
Modulated Frequency Range: 200 – 4000 MHz	Modulated Frequency Range: 2700 MHz
Penetration Depth: 150 cm / 60 in	Penetration Depth: Flex NX and NX25: 0-75 cm (0-30 in) NX15: 0-100 cm (0-40 in) typical, 0-150 cm (0-60 in) based on site conditions
Battery: Flight-safe, removable pack, 8x AA (NiMH)	Battery: Lithium-ion battery (2)
Dimensions: 22.1 x 18 x 14 cm / 8.7 x 7.1 x 5.5 in	Dimensions: 25.3 x 13.2 x 18.9 cm (9.9 x 5.2 x 7.4 in), Display 17.8 cm (7 in) High Resolution Touchscreen
Weight: 1.5 kg / 3.3 lbs (excl. battery pack)	Weight: 2.2 kg (4.9 lbs) including battery 2.4 kg (5.3 lbs) including battery and handle
Applications: Investigation of pavement and bridge decks, Locating of rebars and live wires before drilling, cutting and coring, Shallow utility locating, Concrete Quality Assessment	Applications:
Proceq GP 8000 Includes:	Flex NX Includes: Flex NX Controller, Flex NX Transit Case, Wrist Lanyard, Quick Start Guide, Extra RAM® Mount, Lithium-Ion Battery (2X), 2-Bay Charger
Accessories: Telescopic rod with tablet holder, Universal Tablet Holder, Universal Tablet Holder with chest strap	Accessories: NX25, NX15, NX Telescoping Pole

	<p>GSSI StructureScan Pro</p> <p>Ground Penetrating Radar Equipment StructureScan Pro GSSI</p>
	 <p>The image shows the GSSI StructureScan Pro Ground Penetrating Radar (GPR) system. It consists of a blue SIR 4000 control unit with a screen and buttons, and a Model 615 handcart with an orange and blue frame and black wheels. The control unit is mounted on the handcart.</p>
Radar Technology:	Radar Technology: RADAN 7
Modulated Frequency Range:	Modulated Frequency Range: 1600 MHz, 2600 MHz
Penetration Depth:	Penetration Depth: 46 cm (18 in)
Battery:	Battery: Inspired Energy Ni2040ED, 3 hour runtime (battery life dependent on level of display brightness)
Dimensions:	Dimensions: 14x10x2.75 in (36x25x7 cm)
Weight:	Weight: 9.07 kg (20 lbs)
Applications:	Applications: Scan for rebar, post tension, conduits, and non-metallic objects, Concrete slab scanning, Locate voids, Concrete imaging, Condition assessment, Structural inspection
Includes:	StructureScan Pro Includes: SIR 4000 Control Unit, 1600 MHz or 2600 MHz antenna, Model 615 handcart with encoder, 7-meter control cable, Lithium-ion battery (2), Dual-bay battery charger, Rugged transit case, 2-year warranty
Accessories:	Accessories: Palm Antenna, SIR 4000 stand, SIR 4000 carry harness

	StructureScan Mini XT StructureScan Mini XT GSSI
	
Radar Technology:	Radar Technology:Using RADAN for StructureScan Mini Data Transfer
Modulated Frequency Range:	Modulated Frequency Range:2700 MHz
Penetration Depth:	Penetration Depth: 60 cm (24 in)
Battery:	Battery: Lithium-ion battery (2)
Dimensions:	Dimensions: Display 6.5" Touchscreen LED
Weight:	Weight: 1.8 kg (4 lbs)
Applications:	Applications: Find rebar, post tension, conduits, and non-metallic objects, Measure slab thickness and void location, Concrete scanning and imaging, Condition assessment, Structure inspection
	Mini XT Includes: StructureScan™ Mini XT with 3D software, Lithium-ion battery (2), Dual bay battery charger, Rugged transit case, Quick Start Guide, 2-year warranty
Accessories:	Accessories: Palm XT, LineTrac XT, Carry Harness, Accessory pole

	GSSI Structurescan Mini LXT StructureScan Mini LXT - GSSI Geophysical Survey Systems, Inc.
	
Radar Technology:	Radar Technology:RADAN 7 for StructureScan Mini
Modulated Frequency Range:	Modulated Frequency Range:2700 MHz
Penetration Depth:	Penetration Depth:60 cm (24 in)
Battery:	Battery: Lithium-ion battery (2)
Dimensions:	Dimensions:23.6 x 15.8 x 18.5 cm / (9.3 x 6.2 x 7.3 in)
Weight:	Weight:1.8 kg (4 lbs)
Applications:	Applications: Find rebar, post tension, conduits, and non-metallic objects, Measure slab thickness, Concrete scanning and imaging, Condition assessment, Structure inspection
Flex NX Includes:	Flex NX Includes: StructureScan™ Mini LXT with 3D software, Lithium-ion battery (2), Dual bay battery charger, Rugged transit case, Quick Start Guide, 2-year warranty
Accessories:	Accessories:Extension pole

Proceq GP8800 Proceq GP8800 Ground Penetrating Radar	
	
Radar Technology: Stepped-frequency continuous-wave (SFCW) GPR, Wireless Satellite Antenna	Radar Technology:
Modulated Frequency Range: 400 – 6000 MHz	Modulated Frequency Range:
Penetration Depth: 65 cm / 25.6 in	Penetration Depth:
Battery: Flight-safe, removable pack, 4x AA (NiMH)	Battery:
Dimensions: 8.9 x 8.9 x 7.6 cm / 3.5 x 3.5 x 3 in	Dimensions:
Weight: 487 g / 17.2 oz (excl. battery pack)	Weight:
Applications: Congested rebar configurations, Areas close to walls & underneath pipes, Irregular and curved surfaces, Concrete Quality Assessment	Applications:
Proceq GP8800 Includes:	Palm XT Antenna Includes:
Accessories: None	Accessories: None

CHAPTER 5. EXPERIMENTAL INVESTIGATIONS

The following section is a review of on-site testing activities.

LABORATORY-SCALE INVESTIGATION

Methodology

The laboratory setup designed for GPR surveying consisted of four concrete slabs that were constructed with objects placed during the pouring process to mimic common defects found in concrete structures. Similarly, Rathod and Gupta created structural imperfections in a laboratory setting and used GPR along with other NDT methods for distinguishing these flaws (Rathod & Gupta, 2019) [42]. For the current investigation, the objects included corroded rebar, polyvinyl chloride (PVC) pipes, polystyrene sheets as delamination, and water bottles and balloons to imitate voids. Although these items were known prior to scanning, their locations and placements were not because the slabs were designed and constructed by a different research team member. Each specimen was 3 ft \times 3 ft, with a slab thickness of either 5 or 5.5 inches. The w/c ratio was 0.45 with a compressive strength of 25.8 MPa. The purpose for this case study was to analyze the applicability of locating these flaws with GPR, particularly through the B-scan data. The results were later discussed with the researcher who had placed the items to verify the findings.

The specific GPR device utilized was the Proceq GP8000, which is commercially available equipment manufactured by Screening Eagle Technologies. This device is portable and can be handheld, as shown in figure 55. The GPR consists of the following parameters: (1) SFCW, (2) monostatic antenna with a central frequency of 2.4 GHz, (3) penetration depth of 31.5 inches, and (4) ground-coupled system. SFCW describes the specific type of signals within the radar and

determines energy and resolution [43]. The monostatic antenna system means there is only one antenna, so the transmitting and receiving antenna act as one unit. Lastly, ground-coupled GPR systems describe the antenna hardware and require the device to be in contact or very close to the testing surface, which allows them to integrate more energy into the surface than air-coupled antenna systems [44].

Line scans were taken across the entire slab surface in both x - and y -axis directions, as shown in figure 65. To cover the whole area, the slab was divided into five sections in both the x - and y -directions, resulting in a total of 10 scans for each slab. The scanning started and ended on the slab with the GPR equipment entirely on the surface to avoid any reflections going off the edge. The line scans produce the A-scan and B-scan data formats. Through the compatible processing software, the A-scan data displays the signal for a specific horizontal distance on the radargram. From this, the signal reflections can be seen in relation to the time domain. However, the numerical amplitude values are not provided. Because of this, an assessment of the results was done purely based on an image analysis as opposed to a numerical analysis.

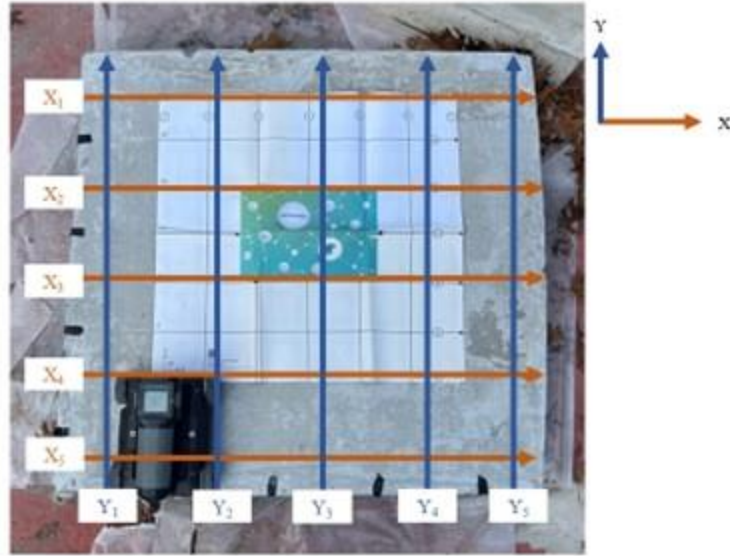


Figure 65. Photo. Surveying grid and directions for GPR scanning on top of slab.

The image processing software that is linked with this specific equipment allows the user to adjust both linear gain (dB) and time gain compensation (dB/ns). Linear gain describes changing the gain or amplitudes from the top down, whereas the time gain compensation adjusts these from the bottom up. For this study, the time-gain compensation was set to 0 dB/ns because the depth of the slab was less than 6 inches. Therefore, any data recorded after that were of no interest. To clearly see the hyperbolic shapes, the linear gain was set to 15 dB. The application has an auto gain feature that is applied as the GPR is scanning, but the user can adjust these qualities as deemed appropriate for interpretation. To stay consistent with analyzing the results, the image processing steps were set the same for all the scans shown, consisting of a linear gain of 15 dB and time gain compensation of 0 dB/ns.

Results

Because the rebar placed in the concrete slab was already corroded before the pouring process, an observation of how the corroded rebar affects the surrounding concrete cannot certainly be

made from this experiment. In natural conditions, the expansion of corroded rebar weakens the concrete with time. Therefore, the main objective of scanning a slab with rebar was to, first, recognize the rebar and, second, determine the spacing and cover depth. Recall that for the GPR to properly display the rebar on the B-scan, the antenna system needs to cross over at a 90° angle. Because the rebar was not visible from outside of the slab, scanning in both the x - and y -directions was necessary. The embedded reinforcement was easily detectable on the line scan Y_3 with the display of three hyperbolic shapes. The B-scan data from this scan are shown in figure 66. Although the slabs were $3\text{ ft} \times 3\text{ ft}$, the scan does not accurately represent this distance because the GPR started and ended entirely on the slab, meaning the antenna system did not transmit and receive signals from the exact edge. A total of three steel members were located, the first two located at around 3 inches and the third at 3.5 inches. The spacing between each was 3 inches and verified by the researcher who designed and built the slabs. However, the rebar at the end should have also had a cover depth of 3 inches. It is possible that it shifted during the pouring process.

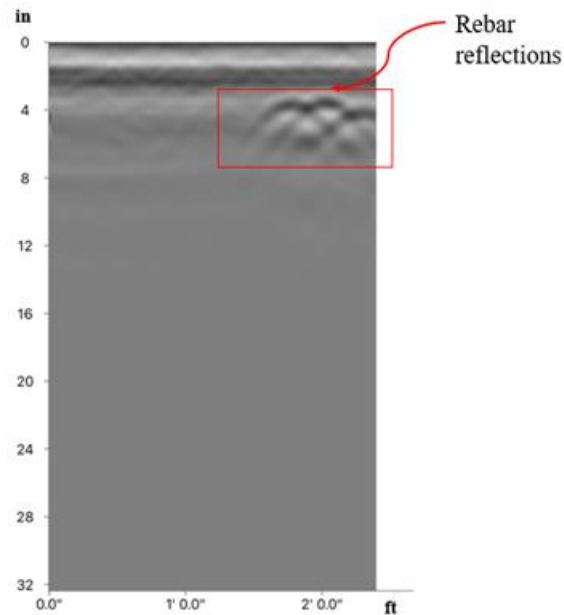


Figure 66. Image. GPR line scan result with corroded rebar.

Three of the four slabs included artificial defects to represent voids and delamination. The results of these three slabs are described below, including some of the images obtained and how the flaws were pointed out. Not every scan image that was produced is presented here because some resulted in no major findings, and some of the same objects appeared on other scans. The objective of this section is to exhibit how the delaminated and void areas were located from the B-scan data.

One slab was known to have two different-sized polystyrene square sheets buried beneath the concrete. One was 4 inches from the top surface and 3 ft × 3 ft, and the other was 2 inches from the top in one corner with dimensions of 1.5 ft × 1.5 ft. These sheets were noticeable on the scans due to the change in material properties from the concrete to polystyrene, and this scenario can represent delamination. The B-scan results are shown in figure 67.

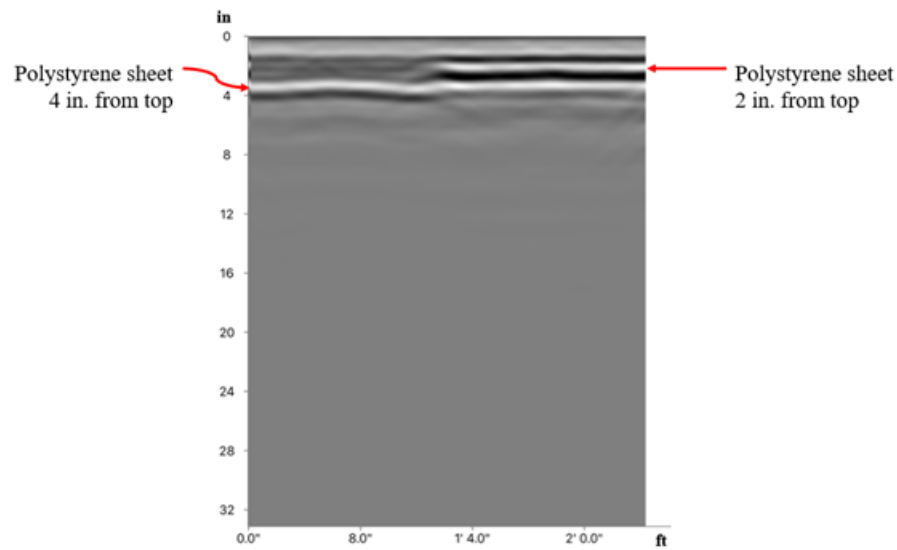
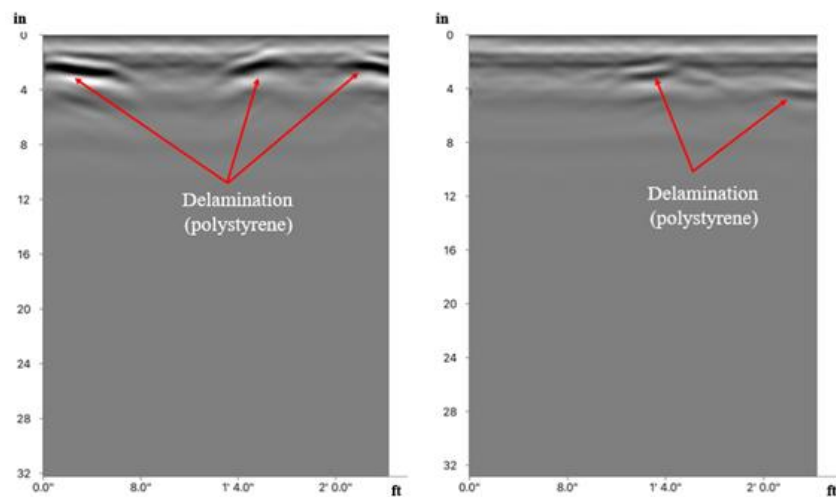


Figure 67. Image. GPR line scan result for slab with polystyrene sheets.

Similarly, another slab had embedded polystyrene sheets but in smaller sizes to also imitate delamination in the concrete. These were found in all scans in both directions, some at 2 inches and others at 4 inches from the surface. Figure 68 displays two separate line scans obtained from the slab, one from the X_3 scan and one from the Y_2 scan.



**Figure 68. Images. GPR line scan results for slab with small polystyrene sheets:
(a) X_3 scan and (b) Y_2 scan.**

Lastly, one slab consisted of water bottles and balloons to imitate voids, along with PVC pipes on a separate side. The PVC pipes had a 0.5 inch outer diameter and 0.25 inch inner diameter with open ends. The balloons did not stay inflated during the concrete pour, which created large air voids on the surface of the slab. Also, one water bottle was not completely buried and could not be scanned due to the rough surface. These flaws are visible on the concrete slab in figure 69.

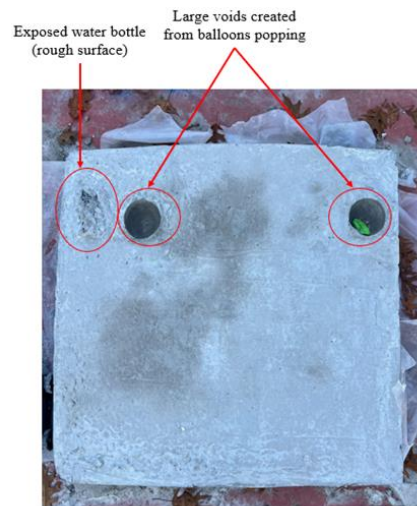


Figure 69. Photo. Slab with visible voids from balloons and one water bottle beneath the surface.

The B-scan results from surveying this slab are shown in figure 70. However, the PVC pipes were basically undetectable on the scans, even after making different gain adjustments. Using the same coordinate system shown earlier, there were five pipes placed in the y -direction at 4 inches deep and three placed over these in the x -direction, 2 inches from the surface. Each pipe was placed 6 inches apart. With this knowledge, the scans over those spots were analyzed again to attempt to locate any hyperbolic shapes from the pipes. The X_4 line scan should have been able to pick up the five pipes in the y -direction, and it is shown in figure 70(a), where the red box indicates the area of the PVC pipes. Although some small hyperbolic shapes are seen, it is nearly

impossible to locate each one. A possible explanation for this could be the small size of the PVC pipes and that the reflected signal of plastic is not as strong as metal. Lastly, the large void to the right of the slab was detected on the Y₅ line scan and is shown in figure 70b.

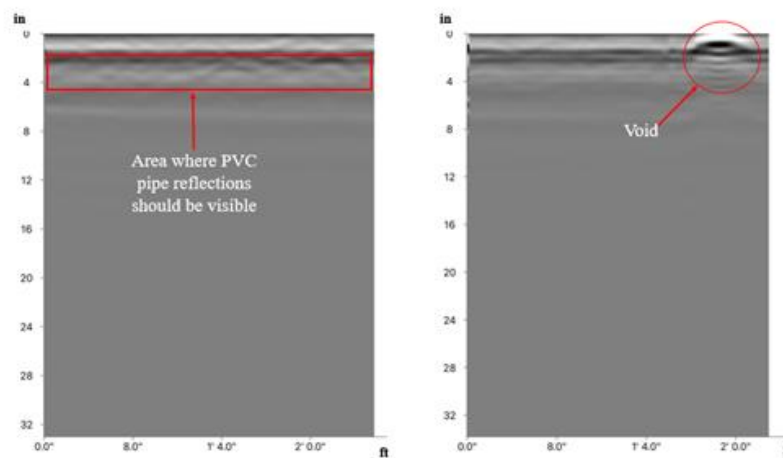


Figure 70. Images. GPR line scan results: (a) PVC pipe location and (b) void location.

Discussion

Based on a study of the literature, the GPR image-based method was used to evaluate artificial defects in concrete slabs in a laboratory setting. Although the B-scan data were analyzed successfully, there were still some challenges encountered regarding this setup and only utilizing GPR equipment. For future work and experimental setups, the following information should be considered:

- For the GPR to accurately obtain results, the surface should be smooth and cleared of any debris.
- For an improvement of results, a placement of rebar in good condition and rebar in poor condition (corroded) should be placed in the same slab to easily compare and observe any differences.

- The slab with rebar could also have artificial defects under the members to mimic the effects of corrosion in concrete.
- Placing the rebar too close together results in an overlapping of the hyperbolic reflection, making it more difficult to accurately observe the location of each.
- The PVC pipes were not distinguishable, but pipes with a larger diameter should be more detectable on the scans.

This preliminary investigation with GPR provided an established method on how to detect typical flaws in concrete with NDT. The GPR technique serves as a practical application for assessing the condition of different types of concrete structures, with and without steel bars. The four concrete slabs were surveyed for artificial defects and evaluated. Although there are some limitations with this approach, GPR still provides a well-grounded method for detecting subsurface objects and locating weaknesses within a structure. Comparison of results from other NDT methods alongside GPR should be used for more confidence in the findings.

GPR 6 ft Concrete Test Using Proceq GP8000

As pictured in figure 71, the test was run on a concrete floor with rebar running through it. In the image shown, there appears to be a surface crack at 5 ft, as well as a spot of delamination at 2 ft.

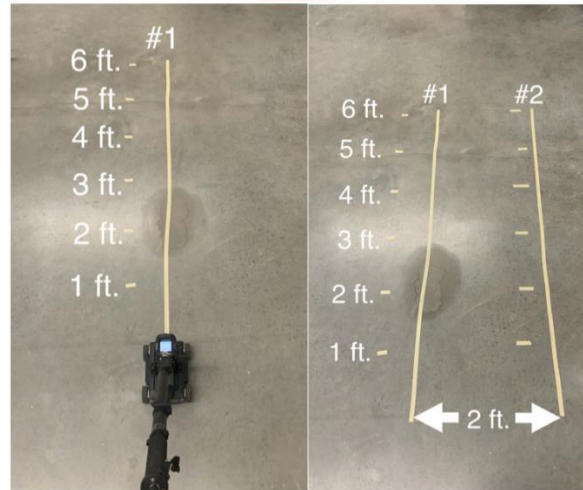


Figure 71. Photos. Laboratory-scale GPR testing.

Repetition Rate

The repetition rate is the number of pulses per frequency. This determines how frequently the radar from the system emits pulses. This is important because it affects the depth of the scan and the resolution of the image. The GPR Proceq GP8000 used to conduct the experiment has a frequency range of 40–3440 MHz. The higher the resolution rate, the more frequent pulses occur; the lower the number, the less frequent the pulses are, resulting in a decrease in resolution.

Dielectric Constant

GPR is a geophysical technique that uses radar pulses to image the subsurface, with a key parameter being the dielectric constant of the material. This constant measures a material's ability to store electrical energy in an electric field, considering both its magnetic and electrical properties. Dielectric constants range from about 1 (for air) to around 81 (for water). The dielectric constant directly impacts the velocity of radar. A higher dielectric constant results in slower wave velocity.

GPR systems measure the time it takes for a radar pulse to travel to a target and reflect back, with this time interval, combined with wave velocity, used to calculate the target's depth. Higher

dielectric constants slow down radar waves, whereas lower constants allow faster travel. The dielectric constant also affects how radar waves reflect at interfaces between different materials. These reflections, due to changes in dielectric properties, are recorded by the GPR system and used to create images of the subsurface (figure 72 and figure 73).

Materials with higher dielectric constants, such as water and wet soils, slow down radar waves more than materials with lower constants, such as dry soils and rocks. This variation is crucial for interpreting GPR data and understanding subsurface structures. Thus, the dielectric constant is essential in GPR surveys, influencing radar wave velocity, depth calculation, and reflection characteristics, and thereby affecting the accuracy and resolution of subsurface images.

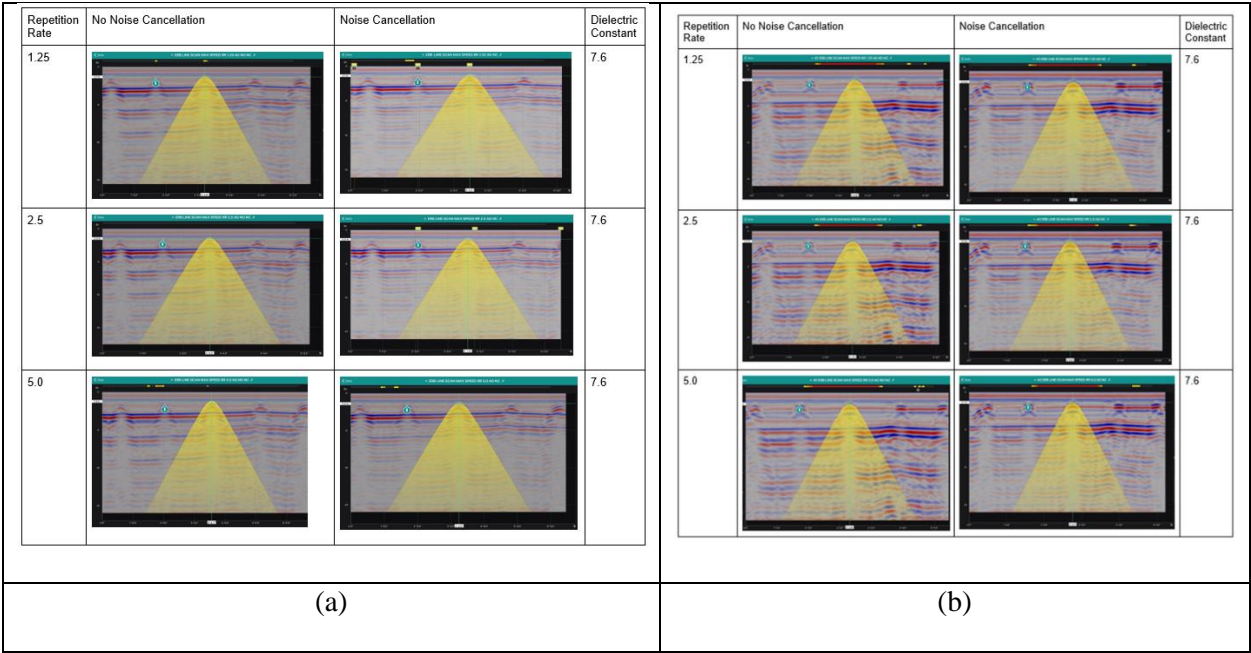


Figure 72. Images. Maximum speed: (a) Test 1 and (b) Test 2.

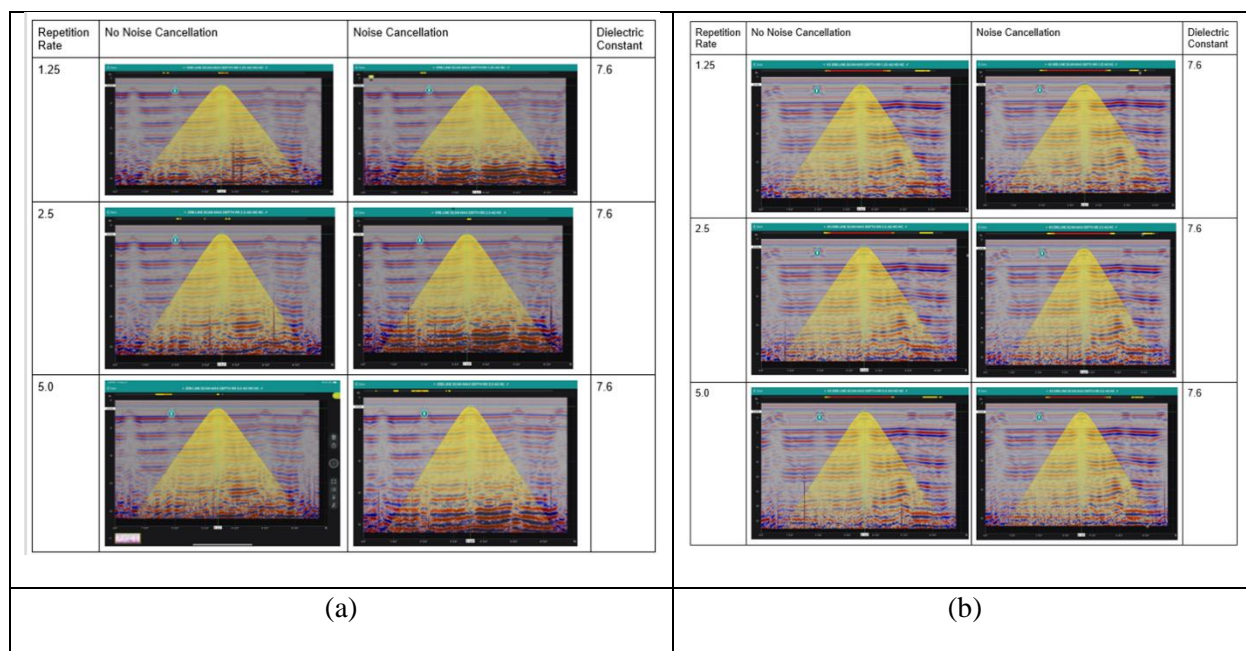


Figure 73. Images. Maximum depth: (a) Test 1 and (b) Test 2.

I-16 BRIDGE IN MACON, GA

On February 7, 2023, the GSU research team joined GDOT for two individual bridge deck evaluations in the Macon, Georgia, area on I-16. The objective of this visit for GSU was to observe the standard testing procedures utilized by GDOT's Office of Materials and Testing (OMAT) when surveying with GPR. The bridge decks were being inspected with plans to overlay with latex-modified concrete. Therefore, checking the cover depth of the rebar was needed to avoid it during the construction process. GDOT scanned the bridge deck, and the GSU researchers followed behind with GSU's GPR equipment (figure 74). Similarly, GDOT implemented the Profometer to detect the rebar and cover depth. GDOT chose the location where to extract a core, making sure to core past the rebar to confirm the depth by visual inspection. Afterward, the hole was filled with Set 45 repair mortar. The distances from the joint to the core location and curb to the core location were measured. Measuring from the curb to the location of

the core extraction is shown in figure 75. Only one core was taken from each bridge inspection in this case.



Figure 74. Photo. Surveying bridge deck with Proceq GP8000 GPR (GSU research team).



Figure 75. Photo. Measuring distance to the core location from curb.

BRIDGE OVER OGEECHEE RIVER

A bridge deck located in Screven County, Georgia, was surveyed and analyzed using NDT applications, including GPR, IE, and a rebar locator. The devices used are all products manufactured by Screening Eagle Technologies. This bridge deck was desirable for evaluation

because it was built in 1941 and suspected to be in poor condition. It was constructed over the Ogeechee River to carry the highway over the waterway; however, it is currently permanently closed off to traffic, so surveying the bridge was easily accessible. Figure 76 shows the satellite view of the bridge used for testing, located to the right of the bridge that is currently in use.



Figure 76. Photo. Satellite view of bridges over Ogeechee River: bridge in use (left) and subject bridge not in use (right).

Multiple NDT applications were utilized for this case, but GPR was the primary method used for assessing the condition of this bridge. The GSU research team visually inspected the bridge, looking for any obvious signs of delamination or spalling on the deck surface. Although there were no clear signs of deterioration on the top slab, corrosion and mold were visible under the bridge. Figure 77 shows the top of the concrete deck and underneath. Two spans were surveyed and analyzed with GPR. Each span was divided into a grid system for implementing line scans across the span. The grid consisted of five scans in the north direction and four in the east direction, resulting in a total of 20 scans for each span to be evaluated. For purposes of this

report, the north direction is referred to as the y -axis and the east direction is referred to as the x -axis.

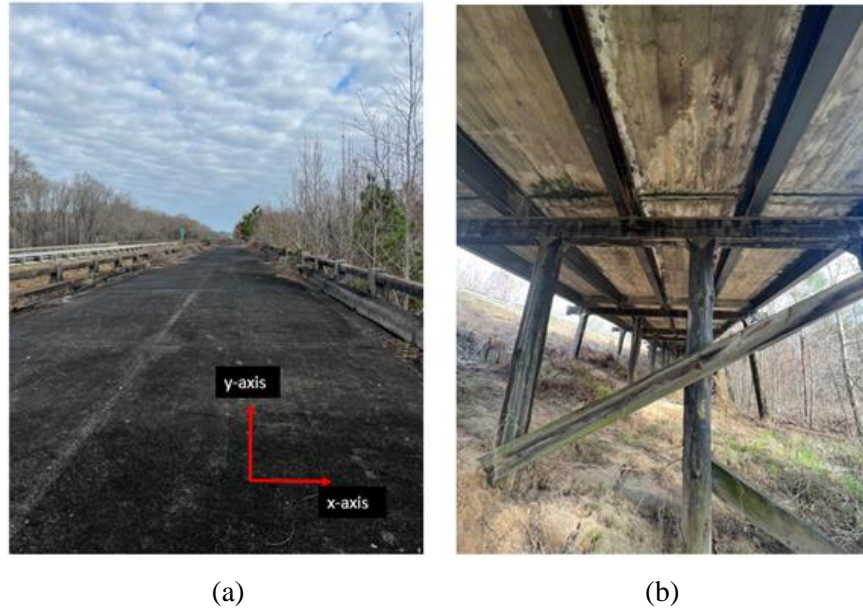


Figure 77. Photos. Bridge deck: (a) top and (b) underside.

The GSU research team scanned the bridge deck and marked areas of concern on the deck on February 14, 2023, to prepare for coring. From analyzing the B-scan data, deterioration and corrosion were spotted based on the theories of GPR. Some areas did not display any serious problems. Signs of corrosion were identified by blurry or unclear hyperbolic shapes, which are weak rebar reflections. GPR data from a line scan in the y -axis are shown in figure 78, where there are clear and unclear hyperbolic shapes. Delamination was suspected where scans displayed a sharp contrast line compared to the surrounding image. An image showing possible delamination is shown in figure 79.

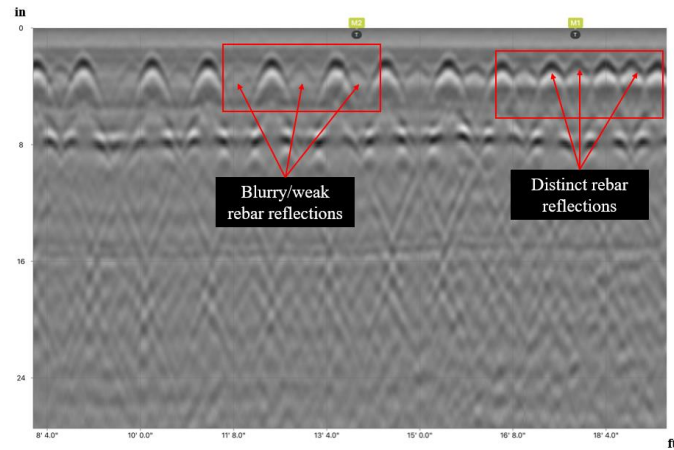


Figure 78. Image. GPR B-scan data in the *y*-axis.

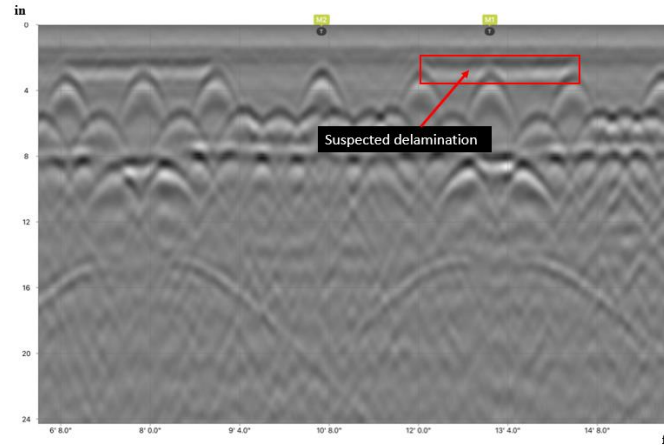


Figure 79. Image. GPR B-scan data in the *x*-axis.

From reviewing similar scan data, multiple spots were marked for GDOT to core on February 15, 2023. Because the bridge is closed to the public, concrete barriers had been placed to block access for vehicles. This limited the placement of the core drill, which was attached to the generator on the vehicle. Therefore, not all marked spots had cores taken. A total of 12 cores were extracted; 3 cores were sent to OMAT for compressive test, and the other 9 were taken by GSU for visual observations. Each core had a diameter of 2.75 inches and ranged 6.875–7.5 inches in length. The core drilling machine is shown in figure 80. The cores taken from

analyzing the scans in figure 78 and figure 79 are shown in figure 81 and figure 82, respectively. The images in Figure 81 show signs of corrosion on the rebar. However, this was not noticeable immediately after coring. These pictures were taken 12 days after. Similarly, the core shown in figure 82 was expected to have delamination from the GPR scan, but there were no signs of this between the reinforcement after coring nor after the 12 days.



Figure 80. Photo. Core drill in use.



Figure 81. Photos. Core 12 days after extraction, corresponding to GPR data in figure 78. Length = 7 inches.



Figure 82. Photos. Core 12 days after extraction, corresponding to GPR data in figure 79. Length = 7.5 inches.

The IE and rebar locator utilized were the Pundit PI8000 and PM8000 Pro, respectively. These methods were applied after coring to obtain additional data. The testing equipment and setup are shown in figure 83 and figure 84, respectively. The IE was used close to the core location with three hits recorded by the impactor. The rebar locator, known as the Profometer, was used over the core location in both directions to obtain rebar depth and diameter. Data analysis still needs to be completed to compare with GPR data and visual inspection.



Figure 83. Photo. Pundit PI8000 probe and impactor.



Figure 84. Photo. PM8000 Pro equipment and drawn grid for surveying.

The GSU research team implemented the UPE technique on the bridge deck over the Ogeechee River in May 2023. This method was used after cores were extracted from the deck to compare the results with the other NDT applications used (i.e., GPR, IE, and a cover meter). Because GPR was the main testing technique for this case, the other practices served as complementary methods to evaluate the areas of concern. Typically, the engineer or technician would use all available NDT methods prior to coring to ensure the location is desirable for assessment. However, it is still possible to obtain information on the surrounding embedded rebar and slab depth for an evaluation of the structure.

The instrument used for surveying is a multi-channel UPE known as the Pundit Ultrasonic PD8050, which is manufactured by Screening Eagle Technologies. Shown in figure 85 is the pulse echo being utilized on the bridge deck near a core location. This technique can be used for a variety of applications, including the following: void and delamination detection, thickness measurement, rebar imaging, and honeycomb detection. GPR is ideal for mapping rebar, whereas pulse echo is more suitable for detecting voids and honeycomb beyond the rebar layer. Different review modes can be used for the evaluation, including A-scans, B-scans, C-scans, heat maps for

depth, and heat maps for pulse velocity. This device measures the pulse velocity of the *S*-waves (secondary waves), which are slower than *P*-waves (primary waves). According to ASTM C597 (Standard Test Method for Pulse Velocity Through Concrete), the pulse velocity is dependent on degree of saturation of the concrete, so this must be considered when analyzing results as saturated concrete produces up to 5 percent higher pulse velocity.



Figure 85. Photo. Surveying bridge deck with Proceq GP8000 GPR (GSU research team).

Methodological Approach

The measurement modes possible with the Pundit PD8050 include a line scan, stripe scan, and grid scan. Both the line scan and grid scan surveying techniques were implemented for this study. A total of eight scans were taken in both modes, consisting of each area where cores were extracted. From a visual inspection from the bridge deck and cores, there were no signs of delamination or honeycomb. Therefore, the results from these tests were primarily used to analyze the depth of the bridge deck for comparison with GPR and cores. Before surveying, the pulse velocity must be calibrated. This consists of pressing the instrument on the testing surface multiple times to obtain an average measurement, which is automatically calculated on the Pundit app. For this bridge deck, the pulse velocity was found to be 8182 ft/s (~2494 m/s) for the *S*-waves. The pulse velocity provides information related to the homogeneity and strength

estimation of the concrete. The pulse velocities for both *S*-waves and *P*-waves and their corresponding concrete quality are shown in table 19, provided by Screening Eagle Technologies (Screening Eagle™). The concrete of the bridge deck is considered to be in good condition, with an *S*-wave velocity in the 2100–2800 m/s range.

Multiple NDT applications were utilized for this case, but GPR was the primary method used for assessing the condition of this bridge. The GSU research team visually inspected the bridge to look for any obvious signs of delamination or spalling on the deck surface. Although there were no clear signs of deterioration on the top slab, corrosion and mold were visible under the bridge. Two spans were surveyed and analyzed with GPR. Each span was divided into a grid system for implementing line scans across the span. The grid consisted of five scans in the north direction and four in the east direction, resulting in a total of 20 scans for each span to be evaluated. In this report, the north direction is referred to as the *y*-axis, and the east direction is referred to as the *x*-axis.

Table 19. Pulse velocity measurements and concrete quality.

<i>S</i>-wave Velocity (m/s)	Corresponding <i>P</i>-wave Velocity (m/s)	Concrete Quality
>2800	>4500	Excellent
2100–2800	3500–4500	Good
1700–2100	3000–3500	Medium
<1700	<3000	Doubtful

For the grid scan measurements, a 5×5 grid was chosen to ensure sufficient data around the cores were measured, resulting in a total of 25 points for one location. One area is shown in figure 86, where each mark represents a new measurement, and the pulse echo was applied to each mark. These were spaced 9 inches apart with consideration of the size of the instrument.

The grid scans provide information on the backwall depth and provide the measurements in the heat map for easy interpretation of the area. On each point scanned, the user can also view the individual B-scan data that were generated, which shows the backwall depth and any possible delamination, voids, or honeycomb along with rebar. Additionally, line scans were taken in the middle along the horizontal direction to go over the core location, which resulted in five scans for the area. These data include the A-scan and B-scan formats.



Figure 86. Photo. Location of a drilled core.

Results

GPR and Core Data

After the bridge deck was scanned according to the grid lines, core locations were marked for both areas of concern and areas that appeared to be in good condition. A similar case study was done by Sham and Lai to evaluate a bridge deck with GPR and visual inspections from coring, along with compressive tests (Sham & Lai, 2017)[45]. Overall, the bridge over the Ogeechee River did not have many locations that appeared to be in poor condition based on the GPR scans. The coring of the bridge deck was completed in one day with the assistance of GDOT. A total of 11 cores were taken; three of these include the cores taken for compressive tests. The areas of

these cores were not assessed by any other NDT methods. The eight cores that were studied for visual inspections are shown in figure 87; the images show the corresponding grid label where they were taken on the bridge deck. The length of the cores varied from 6.875 to 7.5 inches, and not all of the cores went completely through the deck. The diameter of the core drill was 2.75 inches. None of the cores showed delamination or voids after extraction. However, a few showed some possible signs of rebar corrosion and expansion.

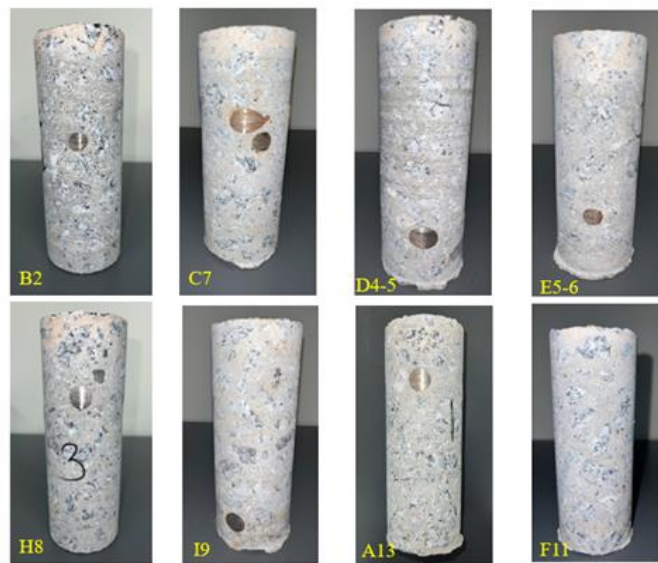


Figure 87. Photos. Eight core specimens chosen for visual inspection.

One scan measurement is presented in figure 88 **Error! Reference source not found.** where suspected corrosion of rebar was marked due to unclear hyperbolic shapes. The A-scan data are displayed on the left, and the B-scan data are on the right. This scan was taken along the y-axis of the bridge deck, or parallel to the direction of traffic. The top layer of rebar can be seen; however, there are a few spots that display unclear hyperbolic shapes. A core was extracted from the marked location, known as core C7. The rebar circled in the figure is shown as the top rebar

on the core, which shows some signs of rust and possible corrosion with the expansion of the rebar.

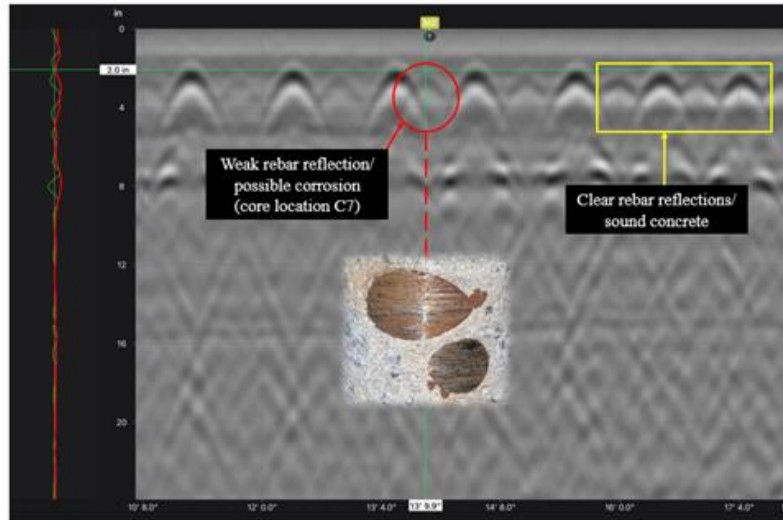


Figure 88. Image. A-scan and B-scan data for core location C7.

Another scan showed a location with a cluttered signal reflection from the bottom layer of rebar, which was also detected in the y-axis direction. The radargram data are shown in figure 89; this location was cored and is labeled as I9. Corrosion can slightly be seen around the rebar, and there is also a small crack near the left, top side of the rebar.

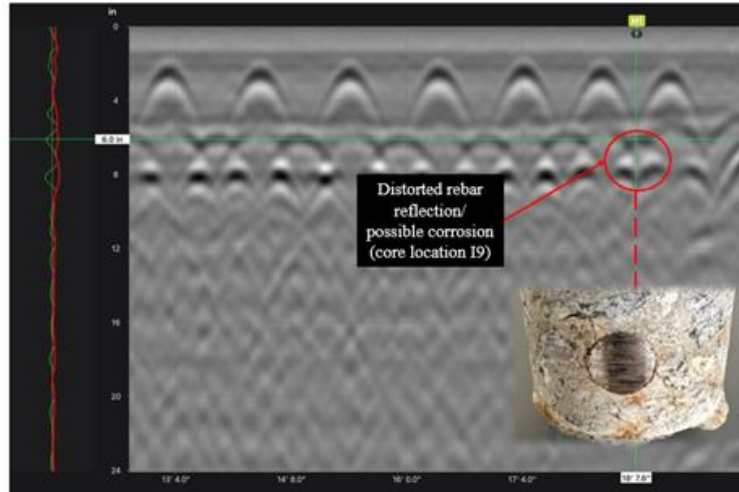


Figure 89. Image. A-scan and B-scan data for core location I9.

Lastly, there were some areas on the bridge deck that appeared as possible subsurface delamination on the GPR scans. Delamination typically presents as an air cavity between the reinforced layer and surrounding concrete [46]. Although it is possible to detect delamination with GPR, it is not the ideal NDT practice for this. One research study implemented GPR on a concrete slab specimen that was implanted with simulated defects to study the challenges and factors when detecting delamination in concrete (Dinh & Gucunski, 2021)[47]. A waveform is still reflected from concrete delamination, but the strength can be affected by the thickness, depth, and even what material fills the delamination, such as air or water. In this study, the “delaminated” areas were identified as locations that had a sharp contrast compared to the surrounding image and displayed as a horizontal line above the rebar. A core was taken in one of these locations for visual observation. The GPR scan measurement and corresponding core is shown in figure 90. The reflections from the steel girder can also be seen below the rebar reflections. However, there were no signs of rebar corrosion or delamination from the extracted core. This reflection in the concrete was caused by some change in material, but the core did not verify what this was from.

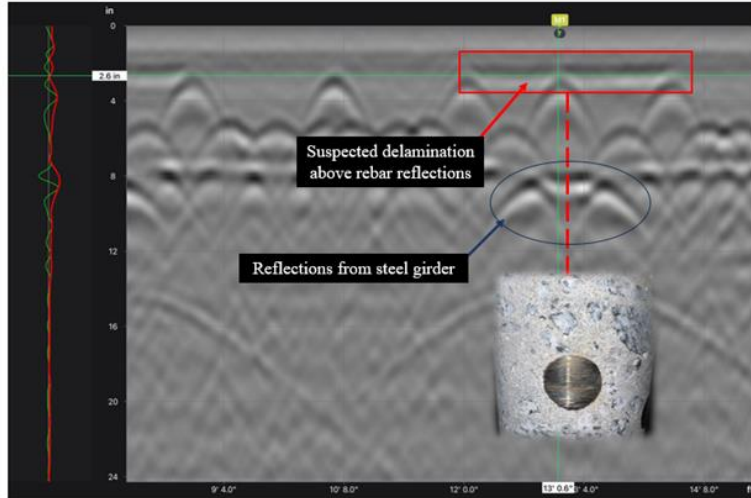


Figure 90. Image. A-scan and B-scan data for core location H8.

A 3D visualization of a section of rebar in the bridge deck is shown in figure 91. This image was created with the B-scan data, and individual reinforcement bars were placed at the hyperbolic peaks. The top layer of rebar can clearly be seen in both directions. The bottom layer of rebar appears to be more closely spaced together in the x -axis. This image provides a general idea on how the rebar was placed because there are no drawing details available. The rebar spacing is discussed in the next section.

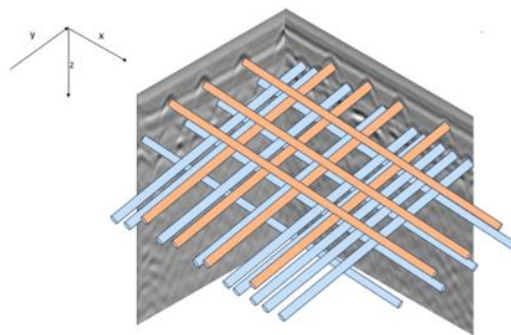


Figure 91. Diagram. 3D visualization of rebar in the bridge deck based on GPR scans.

Cover Meter

The rebar locator was implemented around each core location for obtaining the rebar depth and spacing. For this specific instrument, a rebar diameter estimation must be known prior to scanning. If this is not possible, then the diameter can be set to 16 mm or 0.63 inch for both layers; this imperial bar size is known as #5. From the actual cores, the rebar was manually measured, and the bridge deck consists of #5 and #6 rebar, which has a nominal diameter of 0.75 inch. Recall that although there was a total of 11 cores extracted, the area of the 3 cores sent for compressive tests was not evaluated. Additionally, cores D4-5 and E5-6 represented one location because they were only 3 inches apart, so the area around those cores were evaluated as one location in the NDT inspections. The spacing and depth of the rebar surrounding the core were evaluated in both directions on the bridge deck. For the spacing and depth, the averages and standard deviations were calculated to see how spread out the values were. Only the top layers of reinforcement were detected, and none of the rebar in the 4–6 inch range were spotted as it was on the GPR and core data. However, the cover measuring depth of the Profometer has a detection range up to 7.3 inches. The average depth of the rebar parallel to the direction of traffic (x -axis scans) ranged 2.0–2.8 inches, and the depth of the rebar perpendicular to the direction of traffic (y -axis scans) ranged 1.7–2.2 inches. The average rebar spacing ranged 2.0–5.0 inches in the x -axis scans and 3.7–5.8 inches in the y -axis scans. Figure 92 and figure 93 summarize these findings. The height of the bars are the mean values, and the error bars display how spread out the data are, which were inserted from the standard deviation calculations. The error bars for the rebar depths are smaller compared to those for the rebar spacing, so the data are more spread out around the average value.

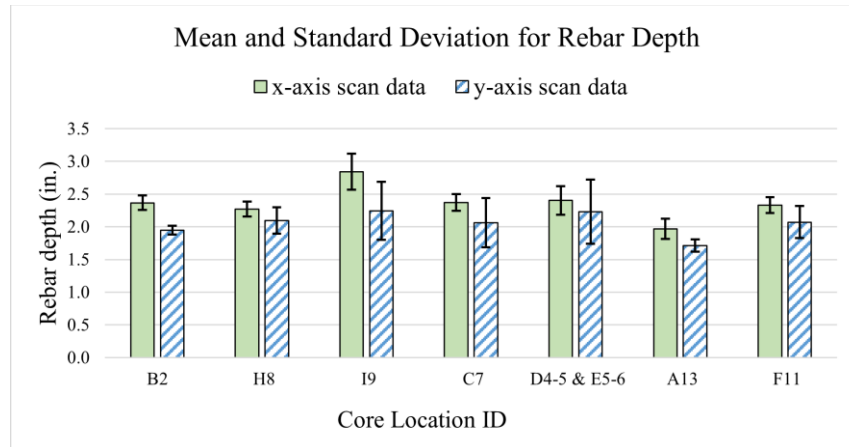


Figure 92. Graph. Mean and standard deviation for rebar depth in both directions.

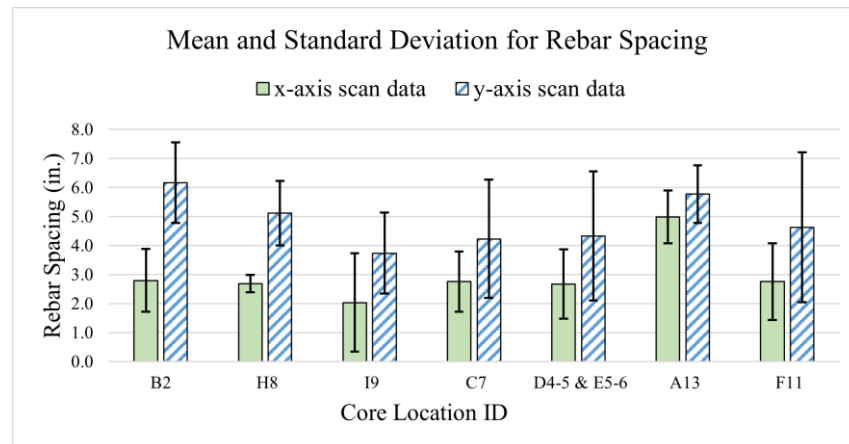


Figure 93. Graph. Mean and standard deviation for rebar spacing in both directions.

UPE

The average global pulse velocity of the concrete that was measured through calibration of the UPE instrument was estimated to be 8,182 ft/s or about 2,493 m/s for the *S*-wave velocity.

According to the table provided by the manufacturer, the concrete is considered to be in good condition because the velocity is in the range of 2100–2800 m/s for the *S*-wave velocity (**Error! Reference source not found.**).

From the grid scan measurements, the heat map provided an *in situ* estimated slab depth. The average slab depth was calculated after exporting all of the data from each measurement at each

core location. However, there were measurements that could not pick up any data, and the spot on the grid was left blank. Additionally, there were readings that were considered outliers that were nowhere close to the thickness of the slab. Although it was expected to see these anomalies at the core location because there was empty space, there is uncertainty as to why the UPE device could not read some of the surrounding spots. Both the blank values and outliers were excluded from calculating the average depth to avoid skewed data. The slab depth averages for the core areas are presented in table 20.

Table 20. UPE data for slab depth estimation.

Core Location ID	B2	C7	D4-5 & E5-6	H8	I9	A13	F11
Average Slab Thickness (in.)	7.00	7.25	7.11	7.17	6.46	7.00	7.10

The B-scan data output from the UPE device displays the subsurface objects and flaws along with an automatic detection for the backwall depth. These are located on the image as high-amplitude reflection responses and can be identified with the spectrum display. One of the line scan measurements is shown in figure 94, which is data from the core area H8. The rebar spots can be seen as the smaller dots near the top, and the slab depth is visible around 7–7.5 inches. This location was suspected to have delamination according to the GPR scan, but the core itself did not show any flaws. The UPE B-scan data show the bottom of the slab and some of the rebar that were perpendicular to the instrument. The location in the middle (labeled 3) is the location where the core was extracted, so there are no backwall data available. The next scan measurement (labeled 4) shows a large area of high reflections but does not appear to be delamination due to the size; delamination would appear as a horizontal line of reflections. This core location was above a steel girder, so it is possible this caused a high reflection response.

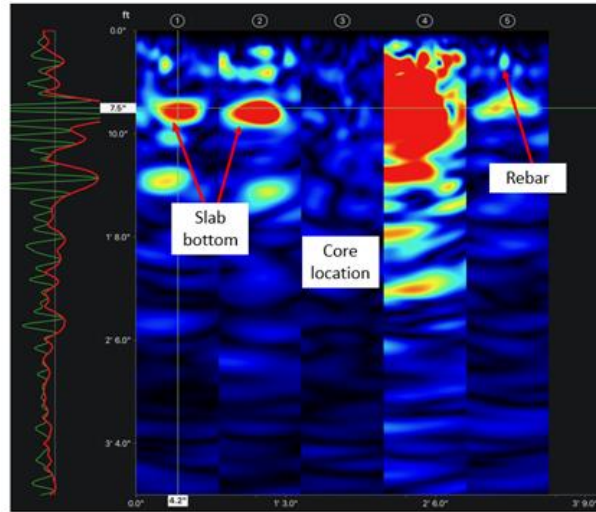


Figure 94. Image. UPE line scan data for core location H8.

Impact Echo

As previously mentioned, the Pundit PI8000 device involves a first calibration of the wave speed in the concrete, which requires the expected thickness of the element that is being tested. Once the velocity is calibrated, tests can be performed. The velocity was calibrated to 3281 ft/s for an expected thickness of 7.75 inches, which was rounded to 7.80 on the instrument. Although there were varying bottom slab depths detected through the other testing methods, this value was set for each location to observe how much this estimation thickness affects the results. In the case that the thickness of an element is unknown, the user might have to use best judgment. If the IE was the first testing method used in this case, the slab thickness would not have been known. However, the 7.8 inches is still close for an estimation of the depth.

The spot test results provide the data in the amplitude versus frequency form, which can be analyzed to estimate thickness and defects. The Fast Fourier transform (FFT) peak gives the measured thickness, where the orange waveform is the most accurate one out of the series of impacts performed. This feature uses auto gain, which automatically detects the thickness. A

lower measured thickness than expected indicates a possible defect or embedded object. When a delamination is detected, there will be a higher frequency. However, the frequency depends on the size of the crack or delamination. The peak data obtained for the bridge deck thickness are shown in table 21 **Error! Reference source not found.** The values range 6.91–8.92, which is a considerable difference.

Table 21. IE data for slab thickness estimation.

Core Location ID	B2	C7	D4-5 & E5-6	H8	I9	A13	F11
Peak detection/slab depth (in.)	6.91	8.41	8.8	8.41	8.92	8.41	8.12

For the analysis of delamination or flaws, the signal responses can be evaluated. Specifically, the core location H8 was analyzed, which was initially suspected to have delamination from GPR data. The results are shown in figure 95. The top image shows the FFT peak, and the bottom image shows the time domain. The three impacts are shown, where the orange highlighted one was found to be the most accurate impact detected by the system. This graph shows the amplitude versus the frequency, and the three separate impacts appear to be similar. Additionally, the amplitude spectrum shows the reflections from the bottom of the deck and top slab surface. The peak or thickness is also higher than expected, so there is no clear delamination or flaws in this spot. In the case that a defect was detected, the amplitude spectrum would display reflections from the top of the slab to the defect, which would be a shorter peak than expected (Carino, 2001)[48].

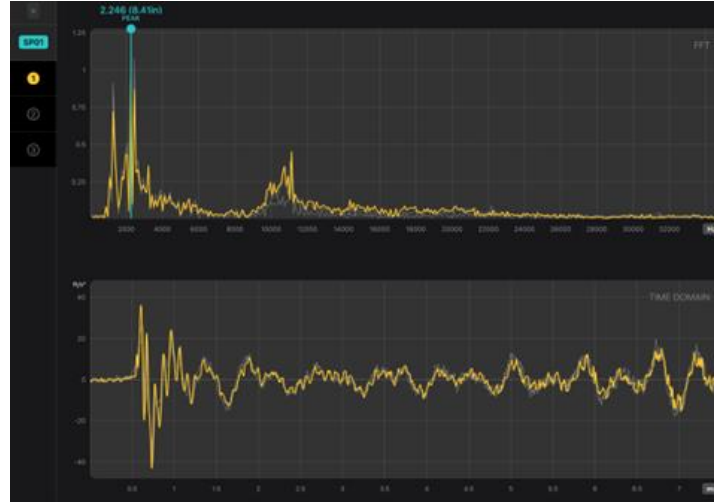


Figure 95. Graphs. IE data response for core H8: FFT (top) and time domain (bottom).

Comparisons with GPR

In this section, a comparison is discussed of the GPR data with the other testing methods. The rebar depth found on the GPR scans was compared to what was manually measured on the actual cores. Core location F11 was not included because it did not have any rebar to evaluate. The mean absolute error (MAE) was calculated to verify the accuracy of the data using equation 30.

Equation 30. MAE.

$$MAE = \frac{\sum_{i=1}^n |y_i - x_i|}{n}$$

where,

y_i = GPR data (predicted values),

x_i = core data (actual values), and

n = total number of data values.

The MAE was calculated to be 0.1 inch, which shows the numbers to be very close in range.

Therefore, this signifies that the GPR was able to closely predict rebar location and depth.

Table 22 shows the individual rebar depths found for each location.

Table 22. Comparison of rebar depth values with GPR and core data.

Core ID	GPR Estimated Rebar Depth (inch)	Actual Rebar Depth Core Data (inch)
B2	2.6	2.75
C7	2.1	2
D4-5	5.3	5.375
E5-6	5	4.75
H8	2.6	2.625
I9	5.6	5.625
A13	1.7	1.625
MAE (inch)	0.1	

For comparison of the cover meter and GPR data, an observation was made that the spacing measurements obtained from the cover meter did not match GPR data. Although the cover meter data from the x -axis direction show the rebar to be closely spaced together, this was not the case for the observed rebar in the GPR scans for the same direction. Refer back to figure 90 to see the GPR B-scan data output for this direction. This specific rebar depth and spacing is seen across all of the scans in this direction, which consists of rebar around the 2.5 inch mark spaced far apart, ranging 13.5–17.0 inches. The bottom layer of rebar around 5 inches is closely spaced together, but from the cover meter data, these points were not picked up. One possible explanation for this occurrence is the cover measurement accuracy can be sensitive to surrounding rebar.

Additionally, the scanning direction of the GPR has an effect on locating cylindrical objects. The antenna system must cross over the rebar to the nearest 90° angle to properly detect the cylinder object. Because the design of the bridge was not accessible, it was not possible to know the

placement of the rebar. However, after data collection and coring, it was revealed that the rebar may have not been exactly perpendicular to scanning. Figure 96 shows all of the core locations on the bridge deck after they were extracted, and they are all oriented in the same direction. These pictures were taken 48 days after the core extraction, so the rust on the rebar is from environmental exposure.



Figure 96. Images. Core locations after extraction.

Because GPR can detect different materials beneath the surface, another applicability with GPR is detecting the slab thickness. This was measured manually in each scan from which cores were extracted. This information was used to compare slab estimation from the UPE and IE methods. The core specimens were also measured in length, but not all of them went through the bridge deck. Table 23 includes the measured slab depth from the GPR, UPE, IE, and core specimens. The slab depth measured from GPR scans ranged 6.8–8 inches. The UPE average measurements ranged 6.46–7.25 inches, whereas the IE measurements ranged 6.91–8.92 inches. The MAE was calculated for the GPR, UPE, and IE data, with the core data being the true value. Three core specimens do not represent the actual bridge deck thickness, so those three were excluded in the

calculations. The MAE for the GPR data was 0.255 and 0.209 inch for the UPE data. The MAE for IE data was higher, with a value of 1.535 inches. This shows there is more range in the data set, and this method is more sensitive to the parameters set before testing, such as estimating the slab thickness. From the surveying and actual data, there is clear evidence that the bridge deck thickness is not even throughout. Both GPR and UPE show to be more dependable methods for estimating the slab depth when the thickness is unknown.

Table 23. Comparison of slab depth data from GPR, UPE, IE, and core specimens.

Core Location ID	GPR Slab Depth (inch)	UPE Slab Depth (inch)	IE Slab Depth (inch)	Core Specimen Length (inch)	Did the core specimen go through the deck?
B2	7.50	7.00	6.91	7.25	No
C7	7.00	7.25	8.41	7.00	Yes
D4-5	7.50	7.11	8.8	7.25	Yes
E5-6	8.00	7.11	8.8	7.25	Yes
H8	7.50	7.17	8.41	7.50	No
I9	6.80	6.46	8.92	6.875	Yes
A13	7.20	7.00	8.41	7.25	No
F11	7.20	7.10	8.12	7	Yes
MAE (inch) (excluding B2, H8, and A13)	0.255	0.209	1.535		

Concrete Compressive Strength

A manual rebound hammer was used on the bridge deck as the NDT method to estimate the in-place compressive strength. This apparatus involves a spring, plunger, and hammer encased in the body of the instrument. The body is pushed toward the testing surface where the hammer is released, and then rebounds. Although using the instrument is simple, it is important that the plunger or head of the hammer is perpendicular to the surface (Jedidi, 2020)[49]. The output value is known as the rebound number, which provides an indication of the concrete strength and

surface hardness. Prior to the application, an area of the deck surface was smoothed out with a rubbing stone. A total of 12 rebounds were recorded, omitting the highest and lowest values, leaving 10 values for the average to be calculated. The average of the recorded numbers was 38.30 MPa or 5555 psi.

For the destructive testing, known as compression testing, three cores were evaluated by the GDOT OMAT. The cores were tested in accordance with AASHTO T24, which is the Standard Test Method of Test for Obtaining and Testing Drilled Cores and Sawed Beams of Concrete. The assessment involves a compression-testing machine to apply a compressive axial load to the specimens until failure, and the compressive strength is measured in psi by dividing the maximum load by the cross-sectional area (ASTM C39/C39M-21, 2021)[50]. The cores were capped with sulfur prior to testing. The data for all three cores are presented in table 24. From the compressive tests, the average compressive strength was 5745 psi. The average results of the rebound hammer and compressive tests show to be close in value, with a difference of 190 psi and a percent accuracy of 96.69 percent.

where the true value was the average strength of the compressive tests, and the observed value was the average compressive strength from the rebound hammer. The compressive strength of concrete is one of the most important properties of the material, and it varies depending on the concrete mixture and curing time of the concrete. Because the concrete mix design is not known for this bridge deck, the tested compressive strength cannot be compared to the designed strength. However, the compressive strength for a deck is typically in the 4000–8000 psi range.

Table 24. Concrete core compressive test data.

Core ID	F1	F2	F3
Core Length (inch)	7.358	7.350	7.323
Diameter (inch)	2.720	2.712	2.730
Max. Load (lb)	30,610	36,860	32,680
Type Fracture	Cone and Shear	Cone and Shear	Cone and Shear
Comp. Strength (psi)	5270	6383	5583
Correction Factor	1.000	1.000	1.000
Adj. Strength (psi)	5270	6383	5583
Average Adj. Strength (psi)	5745		

CHAPTER 6. PRACTICAL IMPLEMENTATION OF GPR

UNDERSTAND AND STUDY THE SCIENCE OF IDENTIFIED GPR TOOL, ITS SENSITIVITY, AND ITS POTENTIAL TECHNICAL LIMITATIONS OR SERVICE-MAINTENANCE REQUIREMENT

GPR technology is based on the principles of EM wave propagation and reflection. It uses radar pulses to non-invasively investigate the subsurface of the Earth, detecting and mapping variations in material properties and features below the ground surface. The fundamental science behind GPR technology includes the following key principles.

Electromagnetic Waves—GPR operates on the principles of EM waves, specifically radio waves in the microwave frequency range. These waves have wavelengths ranging from millimeters to meters. Figure 97 shows a 90 wavelet representing the pulse of EM waves within the GPR signal. Maxwell's equations for the electric field, E , and magnetic field, H , are shown in equation 31 and equation 32.

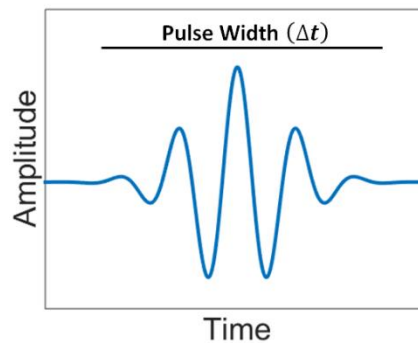


Figure 97. Graph. 90 wavelet representing the pulse of EM waves within the GPR signal.

Equation 31. Maxwell's equation for electric field.

$$\nabla \times E = i\omega\mu H$$

Equation 32. Maxwell's equation for magnetic field.

$$\nabla \times H = -i\omega\epsilon E + \sigma E + J_s$$

Wave Reflection—When EM waves encounter an interface between two materials with different electrical properties (dielectric constants), they experience partial reflection. Some of the energy is transmitted into the new material, and some is reflected back toward the source. The amplitude of the reflected wave proportional to that of the incident wave is defined by the reflection coefficient (R). For EM waves, the reflection coefficient can be expressed as a function of the relative permittivities on each side of the interface. Assuming the EM wave arrives at an angle perpendicular to the interface, the reflection coefficient is given by equation 33.

Equation 33. Reflection coefficient for EM waves.

$$R = \frac{\text{Reflected Amplitude}}{\text{Incident Amplitude}} = \frac{\sqrt{\epsilon_1} - \sqrt{\epsilon_2}}{\sqrt{\epsilon_1} + \sqrt{\epsilon_2}}$$

where ϵ_1 and ϵ_2 are the relative permittivity of the medium carrying the incident and reflected waves, respectively.

Dielectric Constant—The dielectric constant (also known as permittivity) is a fundamental property of materials that describes how they interact with electric fields. It quantifies a material's ability to store electrical energy and determines the speed of EM waves through the material.

Propagation Speed—EM waves travel at different speeds through materials with different dielectric constants. In GPR, the propagation speed of radar waves is typically slower in materials with higher dielectric constants.

Antenna and Transmitter—GPR systems consist of a transmitting antenna that emits EM pulses. These pulses propagate into the subsurface and encounter subsurface features and boundaries.

Receiver Antenna—A receiving antenna is used to capture the radar waves that are reflected back to the surface after encountering subsurface interfaces and objects.

Time Measurement—GPR measures the time it takes for radar pulses to travel from the transmitter, reflect off subsurface features, and return to the receiver. This time measurement is used to determine the depth of subsurface objects or interfaces.

Data Recording—The data collected by GPR are recorded over time, with each recorded pulse representing a specific depth within the subsurface. These data are then processed and visualized to create subsurface images or profiles.

Velocity Analysis—GPR data processing involves analyzing the arrival times of reflected radar pulses to calculate the apparent radar wave velocity in the subsurface. This velocity is used to convert time measurements into depth. The velocity of the EM waves depends on the physical properties of the medium. In general, the velocity of EM waves through a homogeneous material is given by equation 34.

Equation 34. Velocity of EM waves through a homogeneous material.

$$V = \sqrt{\frac{2}{\mu\epsilon}} \left[\left(1 + \left(\frac{\sigma}{\omega\epsilon} \right)^2 \right)^{1/2} + 1 \right]^{-1/2}$$

This equation can be used to show that the EM wave velocity is largest in free space. Therefore, EM waves in matter travel slower than the speed of light.

Reflections and Refractions—GPR waves can produce reflections and refractions at subsurface boundaries. Reflected waves provide information about the location and nature of subsurface features, whereas refracted waves can be used to estimate material properties and depths.

Resolution—The resolution of GPR images depends on the frequency of the radar waves used. Higher-frequency antennas provide finer resolution but shallower penetration, whereas lower-frequency antennas penetrate deeper but with reduced resolution.

Data Interpretation—GPR data interpretation involves identifying and characterizing subsurface features based on the patterns of reflections and other data attributes. Experienced interpreters can differentiate between materials, voids, buried objects, and structural anomalies.

In summary, GPR technology relies on the interaction of EM waves with subsurface materials, particularly variations in dielectric constants, to create images and profiles of the subsurface. By measuring the time it takes for radar waves to travel to the subsurface and back, GPR can provide valuable information about the depth, composition, and location of subsurface objects and features. This technology is widely used in applications such as geophysics, civil engineering, archaeology, and environmental studies.

STUDY THE TECHNICAL CHALLENGES AND OPERATIONAL LIMITATIONS OF GPR

The GSU research team implemented the GPR technique on the bridge deck over the Ogeechee River in May 2023. In addition, GPR technique has been evaluated in GSU’s laboratory for detailed evaluation of its capabilities and challenges for inspection at different conditions. Major observations regarding the technical challenges and operational limitations of GPR that must be considered when used by GDOT are summarized in table 25. Subject matter expert consultation is strongly recommended for practical implementations.

Table 25. GPR major technical challenges.

Technical Challenge	Description
Signal Penetration and Depth Limitations	GPR waves may not penetrate bridge deck materials effectively, especially if the deck contains highly conductive or thick layers. This can limit the depth to which defects or deterioration can be detected.
Material Heterogeneity	Bridge decks often consist of heterogeneous materials with varying properties, such as concrete, asphalt overlays, rebar, and voids. The differing dielectric properties of these materials can complicate GPR signal interpretation.
Reflections and Multiple Interfaces	GPR waves can produce reflections at various material interfaces within a bridge deck, making it challenging to distinguish between actual defects and reflection artifacts. Interpretation errors can occur when multiple reflections overlap.
Rebar Interference	Rebar in bridge decks can cause signal attenuation and scattering, making it difficult to detect defects located below or near reinforcing bars. This can lead to false positives or missed defects.
Signal Attenuation	GPR signals can attenuate as they travel through the bridge deck materials, reducing signal strength with depth. This attenuation can limit the depth at which defects can be reliably detected.
Antenna Frequency Selection	Selecting the appropriate GPR antenna frequency is crucial. Higher frequencies provide better resolution but shallower penetration, whereas lower frequencies penetrate deeper but offer reduced resolution. Choosing the right frequency for a specific bridge deck is a critical decision.
Interference and Noise	GPR data collection can be susceptible to EM interference and environmental noise. Shielding against such interference is essential for accurate results.
Limited Vertical Resolution	GPR systems have limited vertical resolution, meaning they may not be able to distinguish small defects or thin delaminations close to the surface. The ability to detect small defects depends on the frequency of the antenna used.
False Positives and Negatives	GPR assessments can produce false positives (indicating defects that do not exist) and false negatives (missing actual defects). These errors must be considered when interpreting results.
Depth Estimation	GPR assessments provide information about the depth of detected features, but the accuracy of depth estimates can be affected by factors such as signal velocity variations within the materials.
Signal Resolution vs. Depth	GPR systems often have a trade-off between signal resolution and depth penetration. Selecting the appropriate antenna frequency is critical, as higher frequencies provide better resolution but shallower penetration, whereas lower frequencies penetrate deeper but offer reduced resolution.

To overcome these technical challenges, it is crucial to employ well-trained professionals, select appropriate GPR equipment and frequencies, and combine GPR data with other assessment techniques when necessary. Additionally, ongoing research and technological advancements continue to address some of these challenges, improving the effectiveness of GPR in bridge deck assessment.

In addition to technical challenges that must be considered in the practical operation of GPR, there are some operational limitations due to various factors and conditions that can influence the implementation of the GPR. Major operational limitations of GPR in practical projects are summarized in table 26.

Table 26. GPR major operational limitations.

Operational Limitations	Description
Signal Processing and Data Inversion	GPR data collected from bridge decks often require complex signal processing and data inversion techniques to convert raw data into meaningful subsurface images. This process can be computationally intensive and requires expertise.
Bridge Deck Surface Conditions	GPR performance is highly dependent on the surface condition of the bridge deck. Surface conditions of the bridge deck, such as moisture, contaminants, or debris, can affect GPR signal quality. Wet or contaminated surfaces can result in signal attenuation or distortion, reducing its depth penetration and signal quality. To mitigate this limitation, assessments are often conducted during dry conditions, and surface cleaning may be necessary.
Survey Setup and Data Collection Grid	Proper survey setup and data collection grid design are crucial. Uneven spacing or irregular survey patterns can lead to data artifacts and affect the accuracy of the assessment.
Data Interpretation	Interpretation of GPR data from bridge decks requires experienced personnel who can differentiate between various subsurface features and defects. Proper training and expertise are necessary for accurate assessments.
Accessibility and Safety	Accessing all parts of a bridge deck can be challenging, especially in busy or confined areas. Safety considerations and traffic control are paramount when conducting GPR assessments on bridges.
Data Integration	Integrating GPR data with other assessment methods, such as visual inspection, coring, or structural analysis, can be complex but is essential for a comprehensive evaluation of the bridge deck's condition.
Environmental Conditions	Environmental factors, such as temperature, humidity, and electrical interference, can affect GPR performance. Adverse weather conditions or EM interference may impact data quality.
User Expertise	Accurate interpretation of GPR data requires trained and experienced personnel who can differentiate between various subsurface features and defects. Inexperienced users may misinterpret data or miss important details.
Personnel Training	GPR data collection and interpretation require skilled personnel. Inexperienced operators may misinterpret data or miss defects. Proper training and expertise are crucial for accurate assessments.
Cost	GPR assessments can be costly, particularly when extensive surveys are required for large bridge networks. Budget constraints may limit the frequency of GPR inspections.

GPR DATA COLLECTION

Acquisition Parameters

Prior to a GPR survey, care must be taken to select appropriate acquisition parameters to achieve an appropriate balance between cost and data quality. The main acquisition parameters include antenna frequency, number of scans per unit of distance, dielectric constant, range, number of samples per scan, transmit rate, antenna filters, gain, and traverse spacing. Important aspects in planning and preparation, as well as conditions during data collection must be considered.

Antenna Frequency

Investigation of a concrete bridge deck using ground-coupled GPR is frequently performed with the use of one or more high-frequency antennas (>900 MHz) to provide an optimum balance between depth and resolution of imaging [41]. In this project, Proceq GPR Model GP8000 with SFCW radar technology has been used. Modulated frequency range of SFCW for Model GP8000 is 200–4000 MHz, which provides the capability to penetrate into concrete up to 85 cm (33.5 inch). Figure 98 shows the change in penetration depth in concrete as a function of frequency. The SFCW radar has some advantages over the other types of GPRs: wider dynamic range, higher mean power, lower noise figure, and, probably the most important one, the possibility of shaping the power spectral density. The last feature allows changing the level of the side lobes just by changing the “windowing” function. Of course, there is a price to be paid, and this regards the range resolution. Also, SFCW radar opens a lot of opportunities regarding single- and multi-frequencies processing, time-frequency analysis, polarimetric processing; in other words, the SFCW can be seen as a step further toward a software GPR [42].

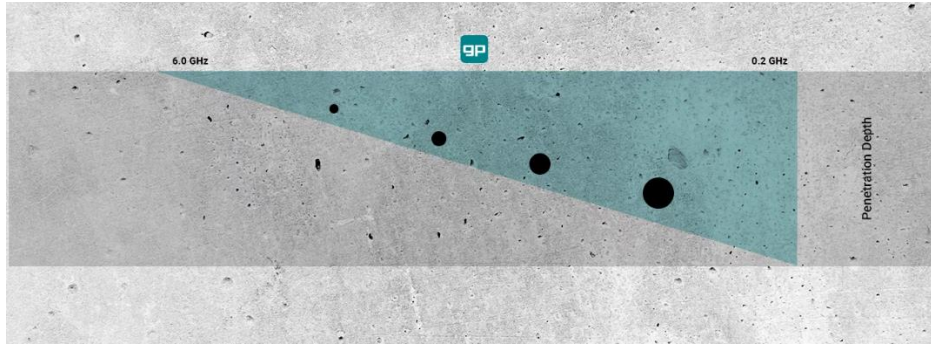


Figure 98. Diagram. Change in penetration depth in concrete as a function of frequency [43].

Number of Scans per Unit of Distance

The number of scans per unit of distance is a function of EM pulse repetition and acquisition speed. This parameter affects both lateral resolution and acquisition speed. To optimize this parameter for the equipment utilized in the field investigations, a survey can be carried out to determine the time required to acquire ground-coupled GPR data that allow clear imaging of individual pieces of rebar for a different number of scans per unit distance. A study by Varnavina et al. concluded that the parameter of 12 scans/ft allows for collecting data more rapidly [44]. However, using such coarse scan spacing may limit data visibility in the field and cause inaccurate manual adjustments of peaks when processing. Conversely, 24 scans/ft is found to be sufficient to image a single piece of rebar for detailed amplitude analysis and can be used to significantly increase data acquisition speed and obtain good quality data for further amplitude analysis. However, it should be kept in mind that if other field estimates are required (e.g., selecting a site for coring, locating an individual steel bar, or imaging of the lower layer of transverse steel), a denser scan spacing is recommended to improve visibility of GPR scans as they are being collected. Clearly, if identifying anomalies in the field is necessary, more care must be taken to investigate those areas.

Dielectric Constant

GPR response is a function of the EM properties: dielectric permittivity (ϵ), magnetic permeability (μ), and electrical conductivity (σ). Dielectric permittivity is a complex function having real and imaginary components. The real portion of dielectric permittivity is usually expressed as the dielectric constant (ϵ_r), which is the ratio of the electric-field storage capacity of a material to that of free space. The imaginary portion of dielectric permittivity is usually expressed as dielectric loss, which represents attenuation and dispersion. Dielectric permittivity, magnetic permeability, and electric conductivity are frequency dependent and behave differently over various frequency ranges [45]. Dielectric constant generally decreases with increasing frequency, whereas conductivity and dielectric loss increase with increasing frequency. However, their behavior is relatively consistent over the typical GPR antenna frequency range of 25–1500 MHz.

The dielectric constant is a critical GPR parameter because it controls the propagation velocity of EM waves through a material and the reflection coefficients at interfaces, as well as affecting the vertical and horizontal imaging resolution. Therefore, knowing the dielectric constant values of materials helps in planning GPR surveys and in better understanding and interpreting GPR images.

The dielectric constant plays a crucial role in GPR surveys, influencing the propagation velocity of EM waves, reflection coefficients at material interfaces, and the resolution of both vertical and horizontal imaging. The dielectric constant is primarily determined by factors such as mineralogy, porosity, pore fluids, frequency, geometries, and electrochemical interactions among a material's components. Reported dielectric constant values for traditional pavement and construction materials provide general ranges of expected values, but these values may not

adequately represent the values in specific field conditions. This can cause errors and deviations in the results. Dielectric constant modeling techniques can help with acquiring more accurate values and decrease the errors in GPR measurements. The results of dielectric constant modeling can be used in planning GPR data acquisition and in interpreting GPR data. For data acquisition, modeling results can be used to determine whether a feature or interface will result in measurable reflections [46].

Weather Conditions

Weather conditions should also be taken into consideration and documented. Changing weather conditions can cause variations in moisture content in the bridge deck, and consequently alter the dielectric constant of the medium investigated. Small cracks and fractures in concrete tend to hold water, increasing both the dielectric constant and conductivity of the material [47].

However, the conductivity of concrete may not be uniform throughout the entire deck due to varying moisture and chloride content. Moisture and chloride content decrease the propagation velocity and reflection amplitude. Fundamentally, propagation velocity, v , is a function of the dielectric constant, ϵ ($v = c/\sqrt{\epsilon}$, where c is the speed of the light), and EM velocity decreases with increasing dielectric constant. Similarly, signal attenuation might affect reflection amplitude as the signal penetrates through conductive concrete, weakens, and strikes reinforcing steel with less energy [48].

Equation 35. EM wave's propagation velocity.

$$v = c/\sqrt{\epsilon}$$

Figure 99 by Varnavina et al. shows the reflection amplitude results from four different scans corresponding to the following: (1) December 5, 2012, 0.98 inch of rain reported within 35 h prior to the investigation, temperature range of 33°–57°F; (2) February 19, 2013, no precipitation

within 24 h prior to the investigation, temperature range of 24°–35°F; (3) May 19, 2013, no precipitation within 24 h prior to the investigation, temperature range of 68°–87 °F; and (4) May 20, 2013, 0.60 inch of rain reported within 10 h prior to the investigation, temperature range of 60°–75°F. Results from scans 3 and 4, which were acquired within 24 h of each other, clearly illustrate a difference in reflection amplitudes at each location along the traverse. Because it is reasonable to assume that the bridge deck did not deteriorate significantly within a single day, the differences in results from scans 3 and 4 can be attributed to differences in weather. Comparing the reflection amplitudes from scans 1–4, it can be observed that the values from scan 4 are larger (less negative) than those of scans 2 and 3. Under the same conditions, these results would suggest that the bridge deck actually improved with time. However, this cannot be the case because no intervention was carried out on the bridge deck within this time period. Therefore, the weather conditions to which the bridge deck was exposed can be assumed to have influenced the results.

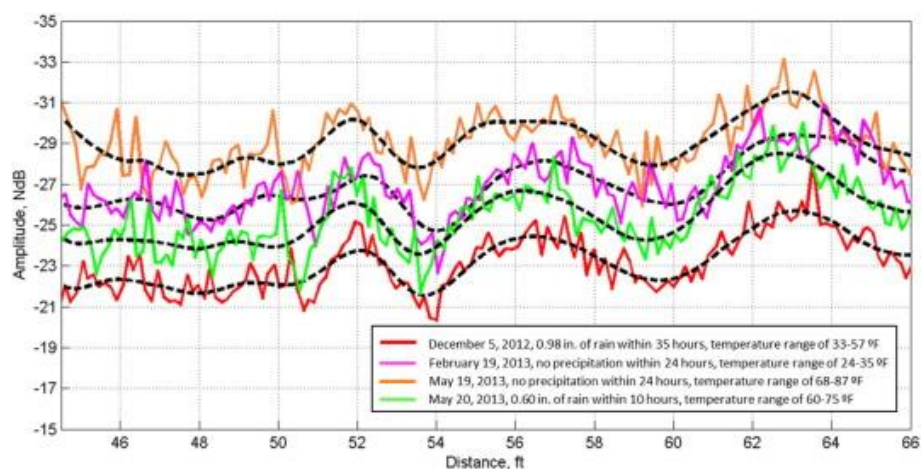


Figure 99. Graph. Reflection amplitude mapped along the same distance in different weather conditions. Dashed line shows smoothed amplitude data. [44].

Range

The range corresponds to the TWTT window in nanoseconds. Setting a longer time range allows energy to penetrate deeper. To set the range appropriately, the target depth, GPR antenna frequency, and the number of samples per scans should be taken into consideration. The user also needs to ensure that the reflected wavelet is sampled with sufficient density to ensure that the maximum reflection amplitude is digitally recorded. In general, a time range of 9–12 ns is needed for shallow concrete evaluations, such as those of a concrete bridge deck. A lower range (9 ns) is to be used for decks in good condition, and a higher time range (12 ns) is required for decks in poor condition after a sufficient amount of precipitation.

As an example, table 27 shows the difference in apparent depth estimated using different values of dielectric permittivity and range associated with good and poor conditions. Note that the range is set a little higher than necessary to pass energy deeper down and allow reflections from deeper layers to be recorded. It is also necessary as concrete is not homogenous, which could cause unforeseen velocity changes. Additionally, a greater range may be necessary if data are to be migrated. It is recommended to acquire test data to ensure that the upper layer of rebar is imaged.

Table 27. Apparent depth estimates calculated for given values of dielectric permittivity and range (ns).

Range (ns)	Dielectric Permittivity	Apparent Depth (inch)
9	6	21.68
12	6	28.90
9	8	18.77
12	8	25.03

Number of Samples per Scan

The vertical resolution and acquisition speed can be influenced by the quantity of samples per scan. Furthermore, an increased number of samples per scan necessitates more computer memory and leads to a decrease in data acquisition speeds. When choosing the number of samples per scan, it is crucial to consider the time window (range). Specifically, if the range is excessively large and the sample count is too low, there is a risk of aliasing. Even in the absence of aliasing, it is essential for the user to confirm that the reflected wavelet is adequately sampled to digitally capture the maximum reflection amplitude. Figure 100 shows the effect of number of samples per scan for the scans collected with the range of 15 ns over a bridge deck.

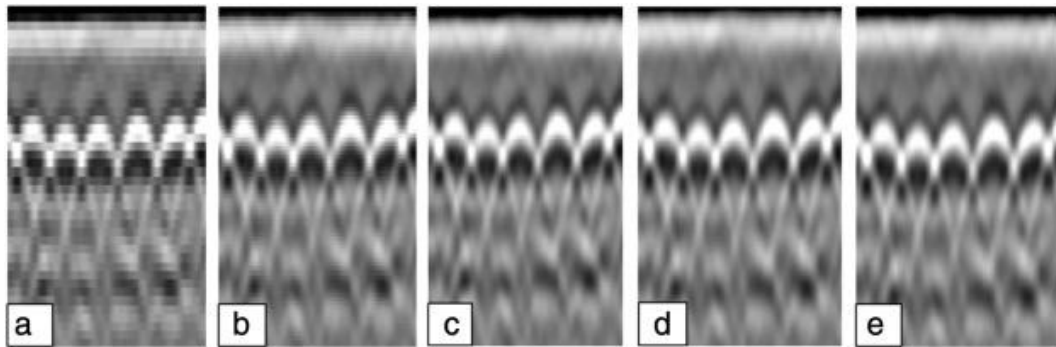


Figure 100. Images. GPR scans collected over a bridge deck using the range of 15 ns and the following number of samples per scan: (a) 128, (b) 256, (c) 512, (d) 1024, and (e) 2048 [44]

Transmit Rate

The transmit rate is indicative of the speed of data acquisition. Elevated transmit rates correlate with a swifter ability to collect data. Select a suitable transmit rate in alignment with the GPR model's manufacturer recommendations.

Gain

It is of utmost importance to fine-tune the gain settings. Ensuring that the gain is appropriately adjusted is essential to prevent any signal clipping or over-gaining. Certain GPR systems are designed to autonomously establish gain settings within acceptable parameters during the initialization period. Typically, one-point gain is employed when acquiring bridge deck data.

GPR DATA INTERPRETATION

Simplifying the automation of GPR data interpretation can be achieved by breaking down the data analysis system into smaller, interconnected subsystems with distinct inputs and outputs. This setup enables the evaluation of each subsystem's performance as an independent module and permits the assessment of various combinations of consecutive subsystems. Additionally, this configuration offers the advantage of distributing data processing across multiple processors, enhancing the speed of analysis. GPR data interpretation can include these major steps: preprocessing, layer interface detection, dielectric properties estimation, and layer/distress separation.

Preprocessing

In its raw form, GPR data often contain noise and clutter. Noise is primarily a result of interference from other radio-wave-emitting devices (e.g., citizens band or CB radios, cell phones, etc.) in the proximity during data collection. Clutter, conversely, encompasses undesired reflections in the GPR signal, complicating data interpretation. In the context of pavement systems, GPR clutter can be categorized into two types: clutter inherent to the GPR system and clutter arising from the surveyed pavement structure. It is important to highlight that the reflection mentioned is consistently present in GPR data. GPR clutter arising from the surveyed pavement structure involves multiple reflections in the GPR signal, typically caused by EM

energy trapped between two highly reflective layer interfaces. In such instances, the EM energy oscillates between the two reflectors, generating an undesired echo on the GPR trace. The impact of this clutter, contingent on the surveyed structure, can be mitigated by appropriately adjusting the length of the GPR scan [49].

Due to the ultra-wide bandwidth of impulse GPR receivers, GPR signals are prone to noise interference. In GPR surveys along highways, prevalent sources of noise affecting reflected signals include cell phone towers, cell phones, CB radios, and other EM devices emitting within the GPR bandwidth. It is important to note that, despite GPR antennas being primarily oriented toward the ground, they can still be susceptible to interference from nearby EM devices. In terms of GPR data analysis, the primary impact of noise is that a significant increase in its level within the reflected signal (resulting in a decreased SNR) reduces the likelihood of detecting reflected pulses.

Detection of Interface Reflections

Previous findings indicate that relying solely on the straightforward detection of reflected pulses within the GPR signal may not always be successful. This is due to the infrequent verification of the condition that the minimum time-delay separation between any two consecutive reflected pulses must exceed the incident pulse width in field GPR data. The imposition of this constraint stems from the transformation of the detection problem into a search for local peaks. It is important to note that any detection technique other than the matched filter (MF) would be similarly bound by this constraint.

To enhance the time-delay resolution of detected pulses in the GPR reflected signal, approaching layer interface detection as an estimation problem, rather than a conventional detection problem, proves beneficial. In this estimation approach, a specific number of pulses are assumed to exist

within the GPR reflected signal, and an optimal estimator is employed to estimate their respective time delays. Notably, in estimation theory, one of the most optimal (unbiased with minimum variance) and feasible estimators is the maximum likelihood estimator (MLE). The MLE is defined as the estimator that maximizes the likelihood ratio, representing the ratio of the probability of the presence of the processed signal to the probability of its absence (i.e., the probability of noise only). With no restrictions on the estimated time delays, except that they should fall within the duration of the reflected GPR signal, this estimation approach ensures high time-delay resolution and accuracy.

Dielectric Properties Estimation

The dielectric properties of pavement layers can be estimated through either destructive means, involving direct measurements on pavement cores, or non-destructively, relying on the analysis of reflected GPR signals. However, due to the potential inaccuracies and perturbations introduced to the pavement structure by the destructive technique, it is not advisable.

Various techniques for estimating dielectric properties of pavement materials from GPR reflected signals were discussed. Analysis of field data revealed that the dielectric properties of HMA materials exhibit negligible variations within the GPR bandwidth. Consequently, the use of an invariant complex dielectric constant in such cases would not compromise the accuracy of GPR results.

Similar findings were reported in another study focused on Portland cement concrete slabs. In both cases, the dielectric constant of pavement materials can be estimated from GPR response, utilizing either the reflection amplitudes measured by an air-coupled GPR system or the reflection time delays measured simultaneously by an air-coupled system and a ground-coupled system.

Layer/distress Separation

The objective of this processing stage is to categorize the detected reflected pulses into two groups: reflections from layer interfaces and reflections from subsurface distresses. This enables the assessment of the degree of deterioration in the surveyed pavement. The separation process relies on the distinctive properties of the two pavement features: layer interfaces typically extend longitudinally along the surveyed pavement, whereas subsurface distresses, such as air voids or accumulated moisture, are generally localized within small areas of the road.

Theoretically, the layer interfaces possess the same length as the surveyed pavement, with some exceptions in cases where the layers are confined to a specific section of the pavement. This scenario arises during full-depth repairs on segments of the surveyed pavement. In such cases, the layer interfaces of the repaired section may not necessarily align with the layer interfaces of the remaining pavement.

However, the layer interfaces of the repaired sections typically exhibit greater length than the localized distresses. The reflections corresponding to localized distresses can also be attributed to false alarms originating from the interface detection stage. However, these reflections are typically scattered and are not consistently present in more than a maximum of three or four consecutive GPR scans. Therefore, distinguishing false alarms from localized distresses is feasible, and the former can be effectively filtered out by eliminating detected pulses that are not consistently present over several consecutive scans.

OPTIMIZING THE INFORMATION YIELD FROM GPR

Obtaining GPR data is not always straightforward, and various factors may constrain the acquisition process. These constraints can include equipment availability, weather conditions,

legal or logistical restrictions, as well as safety or access considerations. In such scenarios, there might be only a single opportunity to gather data. Therefore, it is essential to acquire, process, and model the data with the goal of maximizing the information gained while considering the invested time, cost, and potential hazards. The process commences with appropriately configuring the survey and anticipating site conditions, yet remaining flexible and open to unexpected discoveries. In addition to collecting radar data, various parameters such as calibration, orientation, location, and other essential equipment and survey details are meticulously recorded. These parameters play a crucial role in processing and modeling the data. Consequently, the final outcomes encompass more than just a radar image resembling a pseudo-cross-section. They include a corrected geometric cross-section, interpreted electrical and magnetic properties of the ground, details about the location, orientation, size, and shape of subsurface objects, as well as information about the composition of the ground and objects. This information encompasses inferred density, porosity, fluid saturation, and other pertinent material properties. An example of buried pipe investigation, presented by Olhoeft, is used in this discussion to show the related factors and considerations [50][60].

Locating the Target

Figure 101 illustrates a portion of a radar pseudo-section acquired with a GSSI SIR-10A+ radar system using a 900 MHz in air center frequency bistatic bowtie antenna over a 90 cm diameter steel pipe buried 37 cm deep (surface to top of pipe) [51].

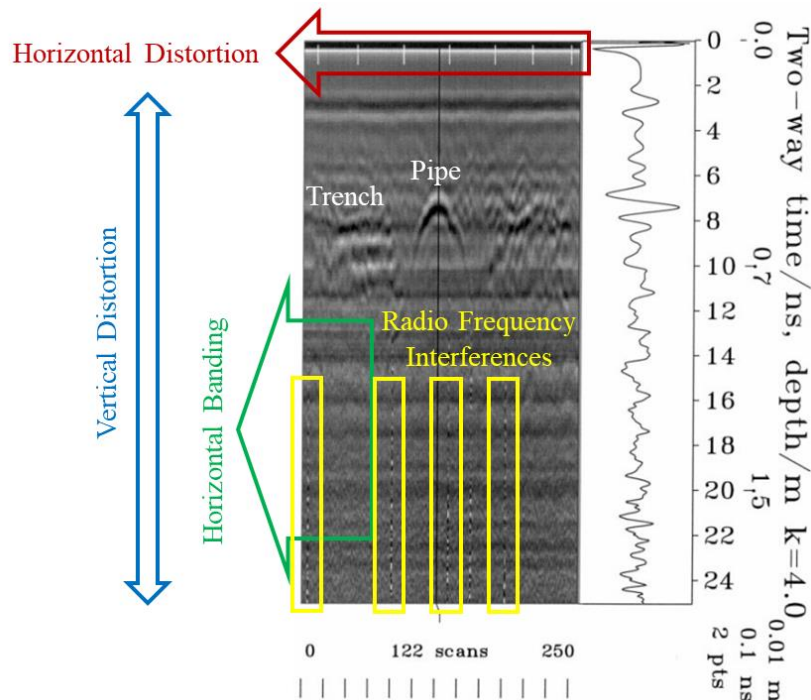


Figure 101. Image. Raw radar data acquired with a GSSI SIR-10A+ using a bistatic 900 MHz in air center frequency antenna towed across a 90 cm diameter pipe buried 37 cm deep.

The radar image data display several issues. Horizontally, the image is distorted due to irregular towing speed and uneven spacing of the marks across the top. Vertically, there is distortion from an unknown velocity of wave propagation. Additionally, horizontal banding is present across the image, caused by suboptimal coupling of the antenna to the ground and unwanted oscillatory ringing of the antenna. There are five vertical lines coming up from the bottom of the image that are caused by RF interference from nearby portable radios or cell phones.

Depth and Size Estimation

If additional information is needed, the initial processing step involves removing any artifacts present in the data. Figure 102 shows the steps in data and image post-processing to enhance the results.

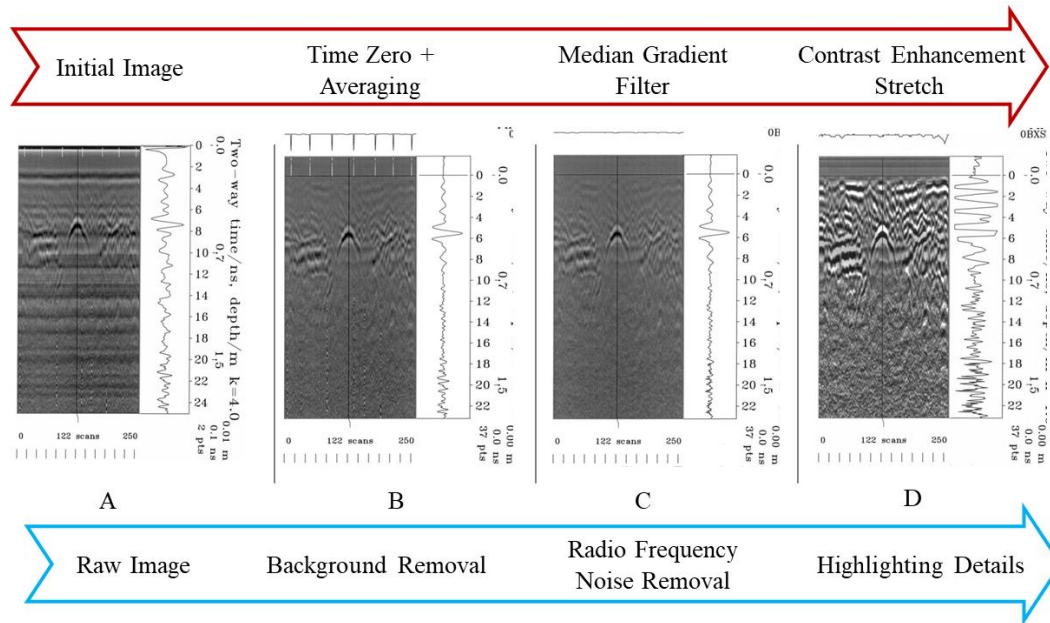


Figure 102. Images. Steps in data and image post-processing to enhance imaging results.

In figure 102B, the time zero has been set at the first energy of arrival. Time zero is a function of the system timing, cable lengths, and antenna positioning. The average of all the scans has been accumulated and removed. Background removal is applied to eliminate the antenna ringing and horizontal banding across the image. The background removal also removes other horizontal features such as flat-lying geology and the surface of the Earth, so time zero had to be located first. In figure 102C, a median gradient filter has been applied to remove the RF interference from nearby wireless phone and portable radio transmissions. In figure 102D, an image processing contrast enhancement stretch has been applied to bring out details in the image. This last step loses all the absolute amplitude information that will be recovered later and enhances not only geological details (note the appearance of several small hyperbolas caused by rocks) but also the noise of the RF interference. These steps are done to improve the ability to clearly see the tails of the pipe hyperbola, to be used in determining the location (based on velocity) and size of the pipe. Following the image improvement steps described above, the quantitative results

must be improved as well. The procedure of improving quantitative results is shown in figure 103.

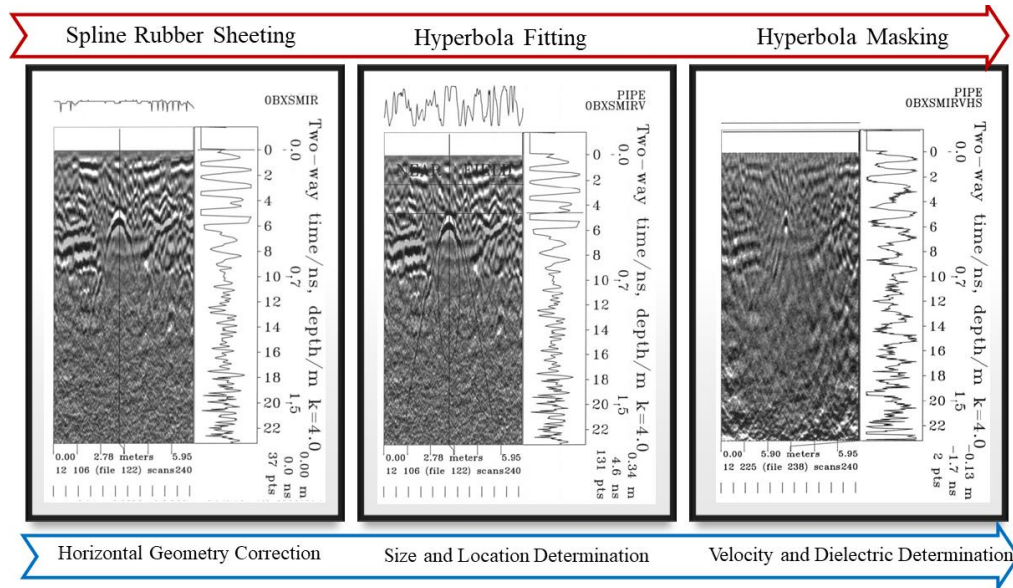


Figure 103. Images. Steps in data and image post-processing to enhance quantitative results.

In the left part of figure 103, the image has changed size and shape slightly as a spline rubber sheeting process is used with the locations of the marks to correct the horizontal geometry of the image. In the middle part of figure 103, a mathematical function has been fitted to the hyperbola shape in the data. The function is a slice from a conic section that is often called “hyperbola.” The radius of curvature at the peak of the hyperbola and the lengths of the asymptotes (by taking into account the antenna pattern) give the size of the object causing it. In the right part of figure 103, an image processing hyperbola mask has been applied to the data to collapse or focus the hyperbola. The image now shows only the scattering cross-section of the visible radius of curvature of the pipe.

GPR IN COASTAL ENVIRONMENTS

As known from many studies and previous reports and discussions, environmental factors such as humidity, as well as ground properties like permeability, can affect the GPR signals and inspection results. Coastal regions, such as Georgia, would face such influences during the GPR survey. A main aspect of efficient GPR surveying in coastal environments is the choice of antenna frequency.

Field Work, Survey Design, and Topographic Correction

To optimize survey efficiency, it is imperative to have a thorough understanding of the orientation of geomorphological features and potential sedimentary structures such as dip and strike. This knowledge can be acquired through various means, including the analysis of aerial photographs, interpretation of topographic maps, and geological mapping. By accurately predicting or determining these geological attributes, survey planners can strategically plan survey routes and data collection points, ensuring comprehensive coverage of the target area and maximizing the effectiveness of subsequent analysis and interpretation efforts. Additionally, this proactive approach enhances the overall reliability and validity of survey results, facilitating informed decision-making in geoscience and environmental studies [52].

Conducting multiple test measurements and transects over a relatively short distance (typically spanning 30–100 m) in various directions is instrumental in obtaining an initial overview of the subsurface characteristics within the study area. These test measurements and transects serve as essential reconnaissance tools, providing valuable insights into the spatial variability of subsurface features such as soil composition, groundwater levels, and potential geological structures. By systematically exploring the subsurface from multiple vantage points and orientations, researchers can gain a comprehensive understanding of the geological heterogeneity

and variability present within the study site. This holistic approach enhances the effectiveness of subsequent data collection and analysis efforts, enabling researchers to make more informed interpretations and decisions regarding subsurface conditions and geologic processes. Moreover, the utilization of multiple test measurements and transects helps to mitigate the inherent uncertainties associated with subsurface characterization, thus improving the overall reliability and accuracy of the study findings [52].

In coastal environments, a 3D GPR survey stands out as an exceptional tool for visualizing and analyzing subsurface sedimentary structures. By capturing data in three dimensions, these surveys offer unparalleled insights into the complex geological features beneath the surface. The ability to visualize the subsurface in three dimensions allows researchers to better understand the spatial distribution and arrangement of sedimentary layers, fault lines, and other geological formations, facilitating more accurate interpretations of past depositional environments and geological processes.

However, it is essential to acknowledge that 3D GPR surveys come with certain drawbacks. One significant limitation is the considerable time and resources required for both data collection and processing. The comprehensive nature of 3D surveys necessitates the acquisition of numerous data points from various angles and depths, leading to extended fieldwork durations and complex data processing procedures. Consequently, 3D surveys may not always be the most practical or efficient option, especially when conducting surveys over large geographic areas or under time constraints.

Despite these challenges, the rich and detailed information provided by 3D GPR surveys often outweighs the associated costs and time commitments, particularly in coastal environments where subsurface structures are intricate and dynamic. By carefully considering the specific

objectives of the study and balancing the advantages and limitations of 3D surveys, researchers can effectively leverage this powerful tool to enhance their understanding of coastal geology and geomorphology.

In coastal environments, acquiring accurate topographic data is crucial for the success of GPR surveys. These data serve as a foundational element in the interpretation of reflexional geometries within the subsurface. To ensure precise interpretations, a topographic correction is necessary to account for variations in terrain elevation. Several methods are available for conducting topographic surveys in the field, each with its own advantages and limitations. One widely utilized approach is the application of a differential GPS (dGPS). dGPS technology offers exceptional accuracy in determining precise positions relative to a reference station, making it well suited for capturing detailed topographic data in coastal environments. By leveraging dGPS equipment, survey teams can efficiently collect elevation data across the survey area, providing valuable insights into the topographic features that may influence GPR data interpretation. In addition to dGPS, alternative methods such as total stations or Light Detection and Ranging (lidar) technology may also be employed depending on the specific requirements of the survey and the characteristics of the study area. Regardless of the chosen method, the careful acquisition of accurate topographic data is essential for achieving reliable GPR survey results in coastal environments. By integrating high-quality topographic data with GPR data, researchers can enhance their understanding of subsurface structures and geological processes, contributing to advancements in coastal geoscience and environmental research.

Choice of Antenna Frequency for Effective GPR Surveys

To ensure the success of GPR surveys, it is imperative to have a clear understanding of the specific data requirements aligned with the scientific objectives of the study. Therefore, prior to

commencing fieldwork, it is essential to define both the depth of investigation and the desired resolution. These parameters serve as critical considerations in determining the appropriate surveying approach and equipment setup. One key aspect to consider when planning a GPR survey is the selection of antenna frequency. This decision involves striking a balance between achieving adequate penetration depth into the subsurface and attaining sufficient resolution to resolve target features. Typically, higher frequencies offer improved resolution but limited penetration depth, whereas lower frequencies provide greater penetration depth at the expense of resolution. In geological materials, the relationship between antenna frequency and penetration depth follows a general trend: lower frequencies tend to result in greater penetration depth. This phenomenon is particularly relevant when surveying subsurface structures in coastal environments, where geological materials may vary in composition and density. By carefully evaluating the scientific objectives of the study and considering factors such as target depth, desired resolution, and subsurface characteristics, researchers can make informed decisions regarding antenna frequency selection. This strategic approach ensures that GPR surveys are tailored to effectively address research goals, ultimately enhancing the reliability and interpretability of survey results in coastal environments [53]. There again, the resolution of GPR data decreases by decreasing antenna frequency [53], [54]. To reveal fine-scaled sedimentary structures, it is necessary to use a higher frequency antenna, which provides higher resolution. To optimize GPR equipment selection and determine the most suitable antenna for the specific investigation target and subsurface conditions of the study area, conducting preliminary testing is highly advisable prior to commencing the survey. This testing phase allows researchers to evaluate the performance of different antennas in terms of their ability to penetrate the subsurface and resolve target features effectively.

GPR serves as a highly effective tool for investigating the shallow subsurface across various coastal environments. Unlike traditional coring methods, which provide discrete samples at specific locations, GPR offers the advantage of generating continuous 2D or 3D profiles with exceptional geometrical and architectural detail. This comprehensive data output enables researchers to visualize and analyze subsurface structures and features with unprecedented clarity and resolution, enhancing the understanding of geological processes and environmental dynamics in coastal regions. By leveraging the capabilities of GPR technology and conducting thorough pre-survey testing, researchers can optimize equipment selection and ensure that the chosen antennas are well suited to the unique characteristics of the study area. This proactive approach maximizes the effectiveness and reliability of GPR surveys in coastal environments, ultimately facilitating more robust and insightful scientific investigations. Coastal dunes present ideal targets for GPR surveys due to their unique geological characteristics and accessibility. GPR technology enables the detection and imaging of the internal aeolian structure of dunes, allowing researchers to visualize the intricate layering and bounding surfaces within cross-bedded aeolian dune strata. By analyzing GPR data collected from coastal dune ridges, researchers can gain valuable insights into the sedimentary architecture and depositional history of these dynamic landforms.

In addition to elucidating internal structures, GPR data from coastal foredune ridges can provide valuable information for establishing a relative chronology of dune deposits. By analyzing variations in radar signatures and stratigraphic patterns, researchers can infer the sequence and timing of sedimentary deposition events, shedding light on the evolution of coastal dune systems over time. Furthermore, GPR surveys offer the advantage of non-invasive data collection, minimizing disturbance to fragile dune ecosystems while providing high-resolution subsurface

imaging. This non-destructive approach allows for repeated surveys over time, facilitating long-term monitoring of dune dynamics and environmental changes. Overall, the application of GPR technology in coastal dune environments holds significant promise for advancing our understanding of aeolian processes, sedimentary dynamics, and coastal geomorphology. By leveraging the capabilities of GPR surveys, researchers can uncover valuable insights into the formation, evolution, and resilience of coastal dunes, ultimately informing conservation efforts and management strategies for these ecologically important landforms. In radargrams depicting till or moraine core deposits, diffraction hyperbolas emerge as prominent and visually striking features, often serving as key indicators of underlying geological structures. These hyperbolas primarily result from the presence of large clasts such as boulders and pebbles embedded within the moraine, which act as scattering objects and generate distinctive radar signatures. Moreover, horizontal layers observed within moraine cores are commonly interpreted as signs of lamination and bedding structures, particularly prevalent in sandy moraine deposits. These layers are often attributed to fluvio-glacial processes, reflecting the dynamic interplay between glacial ice and meltwater streams during deposition.

GPR measurements have proven particularly successful in characterizing sandy moraine deposits, enabling deep penetration into the subsurface to unveil hidden geological features. However, the extent of ground penetration may be constrained by the presence of high clay content within certain moraine cores, which can attenuate radar signals and limit the depth of penetration. Overall, the analysis of GPR data from till and moraine core deposits offers valuable insights into the sedimentary architecture, depositional processes, and geological history of glaciated landscapes. By deciphering the complex radar signatures and interpreting subsurface structures, researchers can enhance their understanding of glacial dynamics and environmental

change, contributing to broader scientific investigations into past glaciations and landscape evolution.

Practical Implementation (GPR Test Procedure)

The following procedure is suggested as a practical implementation of this project and a guide for the technicians and practitioners for using GPR for bridge deck inspection:

Scope

Use this test method to evaluate the condition of a concrete deck bridge by detecting anomalies such as delaminations, voids, rebar condition, and areas with reduced structural integrity.

NOTE: This method will not work for concrete containing lightweight or highly porous aggregates.

This method includes instructions for ground coupled ground penetrating radar (GPR).

Apparatus

1. Ground coupled ground penetrating radar (GPR)

The apparatus consists of the following:

- a. Transmitter Antenna
- b. Receiver Antenna
- c. Processor
- d. Output (Software)

Figure 57, shows the equipment schematics used in bridge deck evaluation. Some of the steps below make reference to the numbers shown on the figure.

NOTE: Check apparatus calibration with the vendor.

2. Apparatus Calibration

- a. Dielectric Calibration: Set the dielectric constant of the GPR system to match the expected material properties of the bridge deck (e.g., concrete permittivity of approximately 7 for accurate depth measurement)
- b. Hyperbola Fitting: Perform hyperbola calibration using a test object to validate antenna settings and ensure accurate rebar depth estimation
- c. Depth and Time Window Settings: Adjust the depth range and time window based on the expected thickness of the bridge deck to optimize data collection without oversampling

3. System Maintenance

- a. Battery Checks: Use flight-safe, rechargeable batteries with a charge sufficient for continuous operation (e.g., 3–4 hours autonomy). Keep spares or a power bank available
- b. Sensor Cleaning: Regularly clean the antenna surface to prevent signal interference caused by dust, debris, or moisture

Survey Region Size and Preparation

1. Preliminary Investigation

- a. Define the total area of the bridge deck to be scanned.
- b. Clear the surface of debris, standing water, and loose materials to ensure consistent GPR signal quality.

- c. Establish a grid or reference system on the deck using markers or GPS to align the GPR scan paths accurately.
- 2. Analyze Site and Material Characteristics
 - a. Assess the deck material and subsurface conditions. Determine the dielectric properties and possible signal attenuation due to moisture or embedded materials.

Procedures

- 1. Planning and Preparation
 - a. Site Assessment.
 - 1) Conduct a preliminary site visit to assess the condition of the bridge and determine the areas to be surveyed.
 - 2) Identify safety hazards and establish access routes.
 - 3) Mark and document any “Region of Interests (ROI)” or concern locations.
 - b. Select GPR Equipment
 - 1) Use a GPR system equipped with antennas suitable for concrete inspection (e.g., Stepped-frequency continuous-wave (SFCW) with modulated frequency range of 200 – 4000 MHz for penetration depth of 80 cm / 31.5 in).
 - 2) Ensure the system has data logging, signal processing, and display capabilities.
 - c. Calibration

- 1) Calibrate the GPR system based on the anticipated dielectric properties of the concrete and the depth of investigation.
 - 2) Perform a test scan on a representative area or a known condition slab to confirm calibration settings.
- d. Survey Plan
 - 1) Define the grid pattern for GPR data collection. A typical spacing is 0.5 m to 1.0 m between scan lines.
 - 2) Mark reference points on the deck surface for orientation during data collection.
2. Data Collection
 - a. Positioning
 - 1) Position the GPR equipment at the starting point of the grid.
 - 2) Align the antenna parallel to the direction of scanning.
 - b. Scanning
 - 1) Move the antenna at a consistent speed (e.g., 0.5 to 1.0 m/s) along the grid lines. Use a mechanical cart if available for better precision.
 - 2) Record data at regular intervals (e.g., every slab's length or width depending on direction of scanning).
 - c. Environmental Conditions
 - d. Avoid scanning in extreme weather conditions (e.g., after heavy rain or flooding).

e. Note any environmental factors (e.g., moisture or surface roughness) that might affect the data.

f. Multiple Passes

1) Perform multiple passes at varying orientations (e.g., perpendicular or parallel according to the planned grid) to ensure comprehensive coverage.

3. Data Processing and Analysis

a. Pre-Processing

1) Apply signal processing features in the equipment software to remove noise and enhance the clarity of reflections. Techniques include background removal and time-zero correction.

2) Make sure to use gray scale for the image processing.

b. Analysis

1) Identify anomalies in the radargram (e.g., hyperbolic reflections indicate objects like rebar; weak signals may suggest voids or delaminations).

2) Estimate the depth and size of detected features using the signal travel time and the calibrated dielectric constant.

c. Mapping

1) Create a condition map of the deck showing the location and extent of anomalies.

2) Categorize defects based on severity (e.g., minor, moderate, severe).

4. Validation

a. Ground-Truthing

1) Verify the GPR findings through coring, visual inspection, or other complementary NDT methods (e.g., ultrasonic testing).

b. Documentation

1) Document the findings in a detailed report, including radargrams, condition maps, and recommendations for repair.

5. Post-Survey Actions

a. Recommendations

1) Suggest maintenance or repair actions based on the severity and extent of detected defects.

2) Provide a timeline for the necessary interventions.

b. Archiving

1) Store the GPR data and analysis results for future reference and monitoring.

Calculations

No calculations are required for this survey procedure.

Report

Report the following information and parameters:

1. General Information

a. Project Details

- 1) Bridge name and location
- 2) Purpose of the inspection (e.g., routine maintenance, damage assessment, load evaluation).

b. Survey Area

- 1) Total area inspected
- 2) Specific regions of interest

c. Environmental Conditions

- 1) Temperature, humidity, and surface moisture levels.
- 2) Time and date of inspection.

2. Data Collection

a. Depth and Signal Quality

- 1) Depth of penetration achieved.
- 2) Signal clarity or attenuation issues encountered.

b. Observed Features

- 1) Hyperbolic reflections indicating rebar or other objects.
- 2) Anomalies like weak signals or noise suggesting voids or delamination.

c. Coverage and Completeness

- 1) Percentage of the bridge deck area scanned.
- 2) Gaps or limitations in data collection.

CHAPTER 7. CONCLUSIONS AND RECOMMENDATIONS

This study illustrates the practical implementation, benefits, and challenges of using Ground Penetrating Radar (GPR) technology for subsurface inspections, with a focus on applications in infrastructure and environmental settings. GPR technology leverages electromagnetic wave propagation to detect and analyze subsurface materials, offering non-destructive insights into material properties, depth estimations, and potential structural anomalies. However, the effectiveness of GPR is influenced by several factors, including material heterogeneity, signal attenuation, environmental conditions, and operational challenges such as surface conditions and interference. To optimize the use of GPR, it is crucial to understand its technical limitations, select appropriate parameters (e.g., antenna frequency, dielectric constant), and ensure proper data processing.

For practical application, particularly in complex environments such as bridge decks, it is recommended to use GPR alongside other non-destructive testing (NDT) methods for a comprehensive assessment. Combining GPR with techniques such as impact echo (IE) or ultrasonic pulse echo (UPE) can improve defect detection accuracy, depth estimation, and data interpretation reliability. Furthermore, conducting pre-survey tests, refining data interpretation algorithms, and providing specialized training for operators can significantly enhance data quality and usability. Future research should focus on advancing GPR data interpretation methods through machine learning algorithms, exploring integration with complementary NDT methods, and developing protocols that address environmental influences on GPR signals.

In conclusion, GPR offers a promising, non-invasive solution for infrastructure and environmental monitoring. With continuous technological advancements and strategic

implementation approaches, GPR can play an essential role in maintaining and assessing critical infrastructure effectively and sustainably.

ACKNOWLEDGEMENTS

The LANDTIE research laboratory at Georgia Southern University would like to acknowledge the financial support for this work provided by the Georgia Department of Transportation. The authors would like to thank the many GDOT personnel who assisted with this study. A special thanks to Mr. Peter Wu, Ph.D., P.E.; Mr. Christopher Collins; Mr. Jacob Walker, P.E.; and Mr. Jason Waters for their research support and valuable input. Special thanks also to the project management team, Ms. Supriya Kamatkar, Mr. Brennan Roney, Mr. Sunil Thapa, Mr. William (Bradley) Bilsback, Ms. Sephara Raymond, and Mr. MD Sabbir Ahmed, who advised the research team in successfully performing the study and assisted with the coordination of the field site visits and testing.

REFERENCES

- [1] National Academies of Sciences, Engineering, and Medicine. (2012). *Nondestructive Testing to Identify Concrete Bridge Deck Deterioration*. The National Academies Press, Washington, DC. Available online: <https://doi.org/10.17226/22771>.
- [2] Oikonomopoulou, E.C., Palieraki, V.A., Sfikas, I.P., and Trezos, C.G. (2022). “Reliability and Limitations of GPR for Identifying Objects Embedded in Concrete—Experience from the Lab.” *Case Studies in Construction Materials*, 16, p. e00898, 2022. Available online: <https://doi.org/10.1016/j.cscm.2022.e00898>.
- [3] Abdel-Qader, I., Abu-Amara, F., and Abudayyeh, O. (2011). “Fractals and Independent Component Analysis for Defect Detection in Bridge Decks.” *Advances in Civil Engineering*, 2011(1), p. 506464. Available online: <https://doi.org/10.1155/2011/506464>.
- [4] Li, B., Zhao, Y., Shen, R., Bi, W., Hu, S., and Huang, H. (2021). “Application of GPR in Rebar Detection of Building Structures.” *IOP Conference Series: Earth and Environmental Science*, 660(1), p. 012022. Available online: <http://dx.doi.org/10.1088/1755-1315/660/1/012022>.
- [5] Prego, F.J., Solla, M., Puente, I., and Arias, P. (2017). “Efficient GPR Data Acquisition to Detect Underground Pipes.” *NDT & E International*, 91, pp. 22–31. Available online: <https://doi.org/10.1016/j.ndteint.2017.06.002>.
- [6] Ristic, A.V., Petrovacki, D., and Govedarica, M. (2009). “A New Method to Simultaneously Estimate the Radius of a Cylindrical Object and the Wave Propagation Velocity from GPR Data.” *Computational Geosciences*, 35(8), pp. 1620–1630. Available online:

<https://doi.org/10.1016/j.cageo.2009.01.003>.

- [7] Hasan, M.I. and Yazdani, N. (2016). “An Experimental and Numerical Study on Embedded Rebar Diameter in Concrete Using Ground Penetrating Radar.” *Chinese Journal of Engineering*, 2016(1), p. 9714381. Available online: <http://dx.doi.org/10.1155/2016/9714381>.
- [8] Tešić, K., Baričević, A., and Serdar, M. (2021). “Non-Destructive Corrosion Inspection of Reinforced Concrete Using Ground-Penetrating Radar: A Review.” *Materials*, 14(4), p. 975. Available online: <http://dx.doi.org/10.3390/ma14040975>.
- [9] Sossa, V., Pérez-Gracia, V., González-Drigo, R., and Rasol, M.A. (2019). Available online: <https://doi.org/10.3390/rs11232814>.
- [10] Wong, T.W.P., Poon, C.S., and Lai, W.L.W. (2018). “Laboratory Validation of Corrosion-Induced Delamination in Concrete by Ground Penetrating Radar.” In 2018 17th International Conference on Ground Penetrating Radar (GPR), IEEE, pp. 1–6. Available online: <https://doi.org/10.1109/ICGPR.2018.8441597>.
- [11] Eisenmann, D., Margetan, F.J., and Ellis, S. (2018). “On the Use of Ground Penetrating Radar to Detect Rebar Corrosion in Concrete Structures.” *AIP Conference Proceedings*, 1949(1), 030009. Available online: <http://dx.doi.org/10.1063/1.5031532>.
- [12] Dinh, K., Gucunski, N., Kim, J., and Duong, T.H. (2017). “Method for Attenuation Assessment of GPR Data from Concrete Bridge Decks.” *NDT & E International*, 92(Dec), pp. 50–58. Available online: <https://doi.org/10.1016/j.ndteint.2017.07.016>.
- [13] Abouhamad, M., Dawood, T., Jabri, A., Alsharqawi, M., and Zayed, T. (2017). “Corrosiveness Mapping of Bridge Decks Using Image-based Analysis of GPR Data,”

Automation in Construction, 80(Aug), pp. 104–117. Available online:

<https://doi.org/10.1016/j.autcon.2017.03.004>.

[14] Alani, A.M., Aboutalebi, M., and Kilic, G. (2013). “Applications of Ground Penetrating Radar (GPR) in Bridge Deck Monitoring and Assessment.” *Journal of Applied Geophysics*, 97(Oct), pp. 45–54. Available online: <https://doi.org/10.1016/j.jappgeo.2013.04.009>.

[15] Im, S.B. and Hurlebaus, S. (2012). “Non-Destructive Testing Methods to Identify Voids in External Post-tensioned Tendons.” *KSCE Journal of Civil Engineering*, 16, pp. 388–397.

[16] Lai, W.W.L., Chang, R.K.W., and Sham, J.F.C. (2017). “Detection and Imaging of City’s Underground Void by GPR.” 2017 9th International Workshop on Advanced Ground Penetrating Radar (IWAGPR), IEEE, pp. 1–6. Available online:

<https://ira.lib.polyu.edu.hk/handle/10397/100760>.

[17] Thitimakorn, T., Kampananon, N., Jongjaiwanichkit, N., and Kupongsak, S. (2016). “Subsurface Void Detection Under the Road Surface Using Ground Penetrating Radar (GPR), a Case Study in the Bangkok Metropolitan Area, Thailand.” *International Journal of Geo-Engineering*, 7(1), pp. 1–9. Available online: <http://dx.doi.org/10.1186/s40703-016-0017-8>.

[18] Xie, X. Qin, H., Yu, C., and Liu, L. (2013). “An Automatic Recognition Algorithm for GPR Images of RC Structure Voids.” *Journal of Applied Geophysics*, 99(Dec), pp. 125–134. Available online: <https://doi.org/10.1016/j.jappgeo.2013.02.016>.

[19] Cassidy, N.J., Eddies, R., and Dods, S. (2011). “Void Detection Beneath Reinforced Concrete Sections: The Practical Application of Ground-Penetrating Radar and Ultrasonic Techniques.” *Journal of Applied Geophysics*, 74(4), pp. 263–276. Available online:

<http://dx.doi.org/10.1016/j.jappgeo.2011.06.003>.

- [20] ASTM International. (2022). “ASTM D6087: Standard Test Method for Evaluating Asphalt-Covered Concrete Bridge Decks Using Ground Penetrating Radar.” ASTM, Available online: doi: 10.1520/D6087-08R15E01.
- [21] Pajewski, L., Derobert, X., Lambot, S., Vrtunski, M., Bugarinović, Ž., Ristić, A., Govedarica, M., Van Geem, C., van der Wielen, A., Grégoire, C., Borecky, V., Artagan, S.S., Fontul, S., and Marecos, V. (2017). “GPR System Performance Compliance.” The Final Conference of COST TU1208, Warsaw, Poland. Available online: https://www.gpradar.eu/onewebmedia/COST_TU1208_SystemPerformanceCompliance.pdf.
- [22] Benedetto, F. and Tosti, F. (2017). “A Signal Processing Methodology for Assessing the Performance of ASTM Standard Test methods for GPR Systems.” *Signal Processing*, 132(Mar), pp. 327–337. Available online: <https://doi.org/10.1016/j.sigpro.2016.06.030>.
- [23] Trung, D.H., Van Giang, N., and Van Nguyen, T. (2018). “The Application of Depth Migration for Processing GPR Data,” *E3S Web of Conferences*, 35. Available online: <https://dx.doi.org/10.1051/e3sconf/20183503004>.
- [24] Dinh, K., Gucunski, N., Kim, J., and Duong, T.H. (2016). “Understanding Depth-Amplitude Effects in Assessment of GPR Data from Concrete Bridge Decks.” *NDT & E International*, 83, pp. 48–58. Available online: <https://doi.org/10.1016/J.NDTEINT.2016.06.004>.
- [25] Dinh, K., Gucunski, N., Kim, J., Duong, T., and La, H. (2015). “Attenuation-based Methodology for Condition Assessment of Concrete Bridge Decks using GPR.” 32st International Symposium on Automation and Robotics in Construction and Mining (ISARC), Oulu, Finland. Available online: <http://dx.doi.org/10.13140/RG.2.1.4714.8003>.
- [26] Diamanti, N. and Annan, A.P. (2017). “Air-launched and Ground-coupled GPR Data.”

11th European Conference on Antennas and Propagation (EUCAP), pp. 1694–1698. Available online: <http://dx.doi.org/10.23919/EuCAP.2017.7928409>.

[27] Liu, H., Yang, Z., Yue, Y., Meng, X., Liu, C., and Cui, J. (2023). “Asphalt Pavement Characterization by GPR Using an Air-coupled Antenna Array.” *NDT & E International*, 133, 102726. Available online: <https://doi.org/10.1016/j.ndteint.2022.102726>.

[28] Bianchini Ciampoli, L., Tosti, F., Economou, N., and Benedetto, F. (2019). “Signal Processing of GPR Data for Road Surveys.” *Geosciences*, 9(96), pp. 1–2. Available online: <http://dx.doi.org/10.3390/geosciences9020096>.

[29] Langman, A. and Inggs, M.R. (2001). “Pulse Versus Stepped Frequency Continuous Wave Modulation for Ground Penetrating Radar.” IGARSS 2001. Scanning the Present and Resolving the Future. *Proceedings. IEEE 2001 International Geoscience and Remote Sensing Symposium (Cat. No.01CH37217)*, 3, pp. 1533–1535. Available online: <https://doi.org/10.1109/IGARSS.2001.976902>.

[30] P. Ulriksen, “Assessment of infrastructure and environmental conditions using GPR,” 1994.

[31] Imse, J.P. and Levine, E.N. (1985). “Conventional and State-of-the-art Geophysical Techniques for Fracture Detection.” Second Annual Eastern Regional Ground Water Conference, Portland, ME, pp. 261–276.

[32] Saarenketo, T. and Scullion, T. (2000). “Road Evaluation with Ground Penetrating Radar.” *Journal of Applied Geophysics*, 43(2–4), pp. 119–138. Available online: [https://doi.org/10.1016/S0926-9851\(99\)00052-X](https://doi.org/10.1016/S0926-9851(99)00052-X).

- [33] Zhao, S. and Al-Qadi, I.L. (2017). “Development of Regularization Methods on Simulated Ground-penetrating Radar Signals to Predict Thin Asphalt Overlay Thickness.” *Signal Processing*, 132, pp. 261–271. Available online: <https://doi.org/10.1016/j.sigpro.2016.06.015>.
- [34] Olhoeft, G.R. (1984). “Applications and Limitations of Ground Penetrating Radar.” *SEG Technical Program Expanded Abstracts*, Society of Exploration Geophysicists, pp. 147–148. Available online: <https://doi.org/10.1190/1.1894192>.
- [35] Morey, R.M. (1974). “Continuous Subsurface Profiling by Impulse Radar.” *Proceedings Engineering Foundation Conference on Subsurface Exploration for Underground Excavation and Heavy Construction*, Henniker, NH, pp. 213–232.
- [36] Doolittle, J.A. (1987). “Using Ground-penetrating Radar to Increase the Quality and Efficiency of Soil Surveys.” *Soil Survey Techniques*, 20, pp. 11–32. Available online: <https://doi.org/10.2136/sssaspecpub20.c2>.
- [37] Rhee, J.-Y., Choi, J.-J., and Kee, S.-H. (2019). “Evaluation of the Depth of Deteriorations in Concrete Bridge Decks with Asphalt Overlays Using Air-coupled GPR: A Case Study from a Pilot Bridge on Korean Expressway.” *International Journal of Concrete Structures and Materials*, 13(1), pp. 1–17. Available online: <https://doi.org/10.1186/s40069-018-0327-7>.
- [38] Sebesta, S., Scullion, T., and Saarenketo, T. (2012). “Using Infrared and High-Speed Ground-Penetrating Radar for Uniformity Measurements on New HMA Layers.” Available online: <https://doi.org/10.17226/22769>.
- [39] Prowell, B., Cervarich, M., Morian, N. and Morian, D. (2021). *Dielectric Profiling System. Implementation Plan (Roadmap)*, Final report, Quality Engineering Solutions, Inc. Available online:

http://advancedmaterialsservices.com/uploads/1/0/7/7/107776005/final_dielectric_profiling_system_roadmap.pdf.

[40] Hoegh, K., Maupin, M., and Dai, S. (2021). “MnDOT DPS Efforts Towards Advancement & Acceptance. Presentation at Dielectric Profiling System (DPS).”

[41] Gehrig, M.D., Morris, D.V., and Bryant, J.T. (2004). “Ground Penetrating Radar for Concrete Evaluation Studies.” Technical Presentation Paper, Performance Foundation Association, pp. 197–200. Available online:

https://www.researchgate.net/publication/252266154_Ground_Penetrating_Radar_for_Concrete_Evaluation_Studies.

[42] Nicolaescu, I., van Genderen, P., van Dongen, K.W.A., van Heijenoort, J., and Hakkaart, P. (2003). “Stepped Frequency Continuous Wave Radar-data Preprocessing.” *Proceedings of the 2nd International Workshop on Advanced Ground Penetrating Radar*, pp. 177–182. Available online: <http://dx.doi.org/10.1109/AGPR.2003.1207315>.

[43] Proceq. “GPR Penetration Depth.” Accessed: Mar. 11, 2023. [Online]. <https://www.screeningeagle.com/en/products/category/concrete/ground-penetrating-radars-gpr>.

[44] Varnavina, A.V., Khamzin, A.K., Torgashov, E.V., Sneed, L.H., Goodwin, B.T., and Anderson, N.L. (2015). “Data Acquisition and Processing Parameters for Concrete Bridge Deck Condition Assessment Using Ground-coupled Ground Penetrating Radar: Some Considerations.” *Journal of Applied Geophysics*, 114, pp. 123–133. Available online: <https://doi.org/10.1016/j.jappgeo.2015.01.011>.

[45] Powers, M.H. (1997). “Modeling Frequency-dependent GPR.” *The Leading Edge*, 16(11), pp. 1657–1662. Available online: <https://doi.org/10.1190/1.1437549>.

- [46] Martinez, A. and Byrnes, A.P. (2001). “Modeling Dielectric-constant Values of Geologic Materials: An Aid to Ground-penetrating Radar Data Collection and Interpretation.” *Current Research in Earth Sciences*, Bulletin 247(1), pp. 1–16. Available online: <https://www.kgs.ku.edu/Current/2001/martinez/martinez.pdf>.
- [47] Tarussov, A., Vandry, M., and De La Haza, A. (2013). “Condition Assessment of Concrete Structures Using a New Analysis Method: Ground-penetrating Radar Computer-assisted Visual Interpretation.” *Construction and Building Materials*, 38, pp. 1246–1254. Available online: <https://doi.org/10.1016/j.conbuildmat.2012.05.026>.
- [48] Barnes, C.L., Trottier, J.-F., and Forgeron, D. (2008). “Improved Concrete Bridge Deck Evaluation Using GPR by Accounting for Signal Depth–amplitude Effects.” *NDT & E International*, 41(6), pp. 427–433. Available online: <https://doi.org/10.1016/j.ndteint.2008.03.005>.
- [49] Lahouar, S. (2003). *Development of Data Analysis Algorithms for Interpretation of Ground -penetrating Radar Data*. PhD dissertation, Virginia Polytechnic Institute & State University, Blackburg, VA.
- [50] Olhoeft, G.R. (2000). “Maximizing the Information Return from Ground Penetrating Radar.” *Journal of Applied Geophysics*, 43(2–4), pp. 175–187. Available online: [https://doi.org/10.1016/S0926-9851\(99\)00057-9](https://doi.org/10.1016/S0926-9851(99)00057-9).
- [51] Olhoeft, G.R. (1994). “Geophysical Observations of Geological, Hydrological and Geochemical Heterogeneity.” 7th EEGS Symposium on the Application of Geophysics to Engineering and Environmental Problems, European Association of Geoscientists & Engineers, p. cp-208. Available online: <https://doi.org/10.4133/1.2922059>.

[52] Tillmann, T. (2012). “Ground-penetrating Radar in Coastal Environments: Examples from the Islands Sylt and Amrum.” *Bremer Beiträge zur Geographie u. Raumplanung*, 44, pp. 60–77.

[53] Bristow, C.S. (2009). “Ground Penetrating Radar in Aeolian Dune Sands.” *Ground Penetrating Radar Theory and Applications*, pp. 273–297. Available online: <https://doi.org/10.1016/B978-0-444-53348-7.00009-0>.

[54] Jol, H.M., Lawton, D.C., and Smith, D.G. (2003). “Ground Penetrating Radar: 2-D and 3-D Subsurface Imaging of a Coastal Barrier Spit.” *Geomorphology*, 53(1–2), pp. 165–181. Available online: [https://doi.org/10.1016/S0169-555X\(02\)00352-5](https://doi.org/10.1016/S0169-555X(02)00352-5).